# Design, Modelling, Fabrication & Testing of a Miniature Piezoelectric-based EMF Energy Harvester

by

Tim E. Pollock

A thesis
presented to the University of Waterloo
in fulfillment of the
thesis requirement for the degree of
Master of Applied Science
in
Mechanical Engineering

Waterloo, Ontario, Canada, 2014

I hereby declare that I am the sole author of this thesis. This is a true copy of the thesis, including any required final revisions, as accepted by my examiners.

I understand that my thesis may be made electronically available to the public.

**Abstract**

Wireless sensing applications have extended into power transmission line monitoring applications. Minimal power consumption of sensor electronics have enabled kinetic energy harvesting systems to provides a means of self sustainability in the form of parasitic energy harvesting from power transmission lines. With this goal in mind, a miniature piezoelectric bimorph cantilever harvester has been developed using a magnetic tip mass which interacts with the oscillating magnetic flux surrounding power transmission wires. The focus of this thesis is develop an analytical model which can be used to optimize the amount of piezoelectric material to support sensory electronics. Special emphasis has also been placed on magnet orientation and geometry to ensure optimal magnetic flux interaction between input and output mechanisms. A single prototype harvester is designed with an arbitrary piezoelectric material length and experimentally validated at different conductor wire currents. The analytical model shows excellent agreement in frequency prediction for the prototype tested. Two damping techniques are used to experimentally extract modal damping ratios to predict peak mechanical and electrical responses at resonance frequencies. The miniature prototype design is less than 30 mm in length with only 10 mm piezoelectric material to produce a total volume of $154 \times 10^{-12} cm^3$. The power output is measured at 174.1 $\mu$W of power when positioned over top a 10 AWG copper conductor a distance of 6 mm with approximately 16 Amps of current passing though the conductor.

**Acknowledgements**

First and foremost I would like to thank my supervisor Dr. Armaghan Salehian for the opportunity to come to the University of Waterloo and pursue graduate studies. During my time at Waterloo she has made it possible for me to become involved in multiple academic and industry research challenges. These experiences have exposed me to a multitude of engineering tools which allowed me to hone my analytical skills in a variety of ways and ultimately broaden my engineering prowess.

Second, I would like to thank my lab mates Blake Martin, Steven Lao, and Mohammed Ibrahim. Your personal support and knowledge in areas I was not as well-versed in has truly played an integral role in my success. I would also like to thank Adam Craig and Shamsheer Chauhan for their dedication and helpfulness towards the completion of this work. The technical staff at Waterloo has also been phenomenal with their helpfulness and facilitation of experimental work and I would like to thank Andy Barber, Chris McClellan and Richard Parker.

Last but certainly not least, I would like to thank my family and friends for their unconditional and ongoing support of my goals. It means a great deal to have the support from the people closest to you.

## Dedication

I would like to dedicate this work to my parents, Brian Pollock and Vallerie Hamel. Words can not express the amount of gratitude I have for the two of you. Your continued support has allowed me to accomplish so many things and made me the person I am today.

# Table of Contents

# List of Tables

# List of Figures

# Chapter 1

# Introduction

## 1.1 Motivation

In todays world, developing greener technologies has become a priority that extends across every major industry. The reason for this is primarily due to societal recognition in the importance of environmental responsibility. Growing concern for decreasing fossil fuels and increasing environmental decay have of course accelerated this trend in the last few decades. Furthermore, governmental incentives and inherent cost savings associated with green technologies have also been strong motivation for these technological shifts. Subsequently academic and industrial investment in green energy alternatives have grown. One technological area which has gained interest and has benefited from greener energy solutions is electronics. Given the ubiquitous nature of electronics and more specifically wireless electronics around the globe today, the need for sustainable power solutions is at an all time high. This technological trend has consequently placed a large demand on stored energy in the form of battery cells to supply electronic energy needs. Although this is a viable solution for the short term, the problem with battery dependence is that the entire system is dependent on the lifespan of the battery that supplies it. This can be costly and problematic in many applications where reliable electronic operation is crucial(health, industrial, communications, etc.). In some cases when the battery is depleted, it can be recharged but often is simply discarded. Both of these options can be quite costly when considering the cost of replacement/recharging does not stop at the cost of the battery itself but also the associated labor and maintenance cost. Furthermore, there is the environmental cost associated with battery waste disposal since batteries also contain hazardous chemicals. These inherent shortcomings do not provide a cost effective sustainable

solution for small wireless electronics that are currently dependent on battery power.

The presence of electronics extends even further in some industrial sectors where wireless electronics have begun to form "'intelligent"' environments which are made up of large quantities of wireless sensor nodes. Wireless sensor nodes can adopt many different forms however a simplistic representation of what a sensor node may be comprised of is depicted in Figure 1.1. The main goal of most wireless sensors is to collect and transmit data for monitoring, control and analysis. Groups of sensors make up what is often called a WSN(wireless sensor network) which are used for countless applications across many industries for data acquisition [1–4]. As the need for electronics and WSN's increases, the environmental impact and additional costs associated with battery replacement increases substantially. Even though technological advancements in battery density have been made, batteries continue to lag behind many other electronic technology to date [5, 6]. Wireless sensors are designed to consume as little power as possible to extend their life. Often the design of the sensor node and the life of the sensor is often limited to the capacity and life of the battery which powers it [7, 8]. These technological, societal and environmental trends give rise to the need to investigate self powering solutions in the form of environmental energy harvesting in order to mitigate these issues.

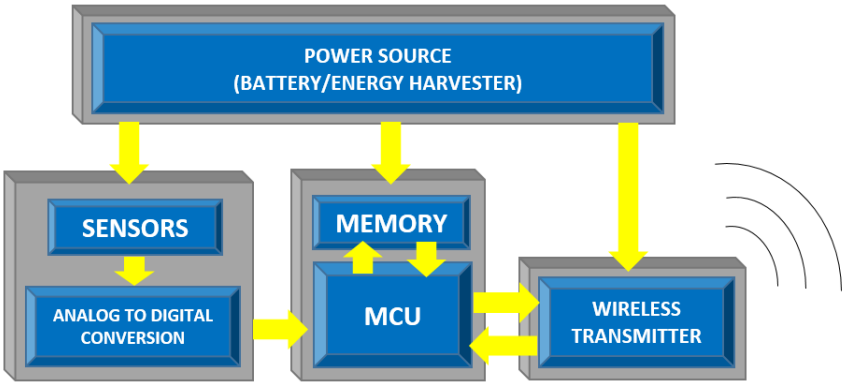


Figure 1.1: Typical Wireless Sensor Node

Wireless sensors in general over the past decade have been decreasing in both size and energy dependence allowing for alternative power solutions such as energy harvesting technology to become a viable and sustainable powering solution. Energy harvesting in general is not a new concept with known environmental effects such as solar, wind, hydro and geothermal energy all being harvested for many years. However these sources of energy are typically too large and constitute hardwired connections to the grid since storing harvested energy in large battery cells would be too cumbersome and impractical. Wireless

sensor nodes require minimal power and often only operate on a very low duty cycle which places them in a very low power consumption 'sleep mode' for the majority of their existence. Furthermore, wireless electronics and sensor nodes often find themselves in remote locations where large energy sources may not exist and therefore a more versatile energy solution is required. To that affect, alternative energy sources in the form of mechanical energy such as vibration, changing magnetic fields, and radio waves is often available in most environments. These smaller energy sources can be converted to useful power and stored in super capacitors to sustain continuous or intermittent wireless sensor node functionality. With that in mind, the sensor environment often dictates which mechanical energy is most practical to support an energy harvesting system capable of meeting the power requirements of the wireless sensor node.

The North American power grid is one of the greatest engineering achievements of the past century. Depicted in Figure 1.2 is a basic diagram which shows a general description of how power is delivered through transmission lines from power plants to customers. Power lines extend more than 320,000 km across the continent servicing approximately 283 million people [9]. Our society as a whole has come to depend on this power system for virtually all aspects of life in the twenty-first century. We expect this system to work when we need it to and take for granted the amount of control that is needed to sustain such a vast system. With control comes extensive system monitoring to provide feedback for adjustment during peak consumption hours, and to resolve outages due to storms and natural disasters. Grid monitoring requires a vast sensor network to collect and transmit data to maintain and ensure reliable power delivery across North America. Recently, hydro companies have expressed interest in the development of an energy harvesting unit that could be mounted on power transmission lines to provide a non-invasive, cost effective and maintenance free means of powering grid monitoring sensors found in WSN's across North America. With that interest, the scope of this research was formed.

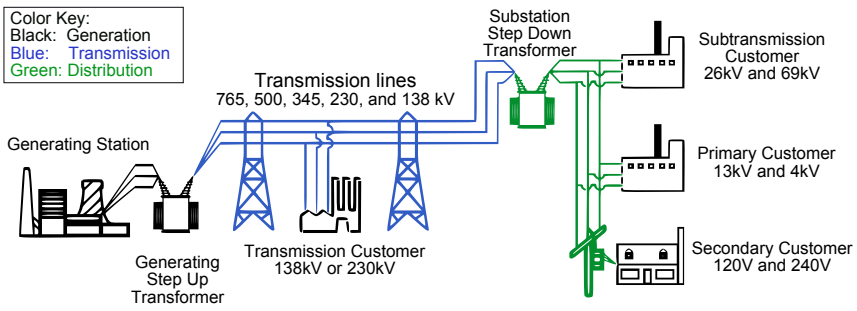


Figure 1.2: North American Power Grid [9]

## 1.2 Scope of Research

The purpose of the present thesis research is to design an energy harvesting unit that is to be mounted atop power transmission lines and harvest power from the most reliable source of energy. Although solar energy is quite abundant, complications quickly arise when considering evening hours, light density due to obstruction(buildings, trees, cloud cover etc.), latitudinal position and weather complications(ice and snow) [10]. Since power transmission lines emit an abundance of alternating EMF(electromagnetic force) energy, this was selected as the most reliable energy source the harvester could scavenge from. The harvester shall be designed to be mounted on single conductor transmission lines that operate at a 60Hz primary frequency with current amplitudes ranging from 10A-1000A. However for proof of concept prototype testing, a current amplitude up to 15 amps is acceptable.

With the energy source defined, the harvester is to be designed and optimized to operate at a 60Hz frequency. An energy transduction method is to be chosen by evaluating common techniques found in literature. The harvester is to be cost effective, practical and miniature in size. An analytical model is to be developed to predict the mechanical and electrical behaviour of the harvester and be validated experimentally through prototype fabrication. The voltage regulation and conditioning will not be considered in this thesis and are outside the scope of this work. The determination of this work will be the model validity based on laboratory experimental results.

## 1.3 Contribution

This thesis provides an accurate analytical approach using a distributed parameter model which can be used to model and design miniature piezoelectric bimorph energy harvesters to be used for power transmission line harvesting applications. Optimization efforts are made between input (conducting wire) and output (piezoelectric material) mechanisms to maximize power output for a designed frequency of 60 Hz within the volume and size constraints set forth. Electromagnetic flux optimization efforts are made to select proper single magnet tip mass orientation through analytical modelling and simulation. The results maximize the force between magnet and conducting wire to generate increased amounts of strain in the piezoelectric material mounted on the beam. A discontinuous modelling technique is used to provide a generalized design tool for determining power output per unit length of piezoelectric material to optimize piezoelectric material costs for varying electronic sensor applications.

## 1.4 Thesis Outline

This thesis will be structured in the following manner.

**Chapter 2** will be structured into two portions. First, to begin with an overview of common transduction methods with a focus on general kinetic energy harvesting methods that relate closely to the proposed design. This will provide a foundation for understanding current harvesting advances and key concepts discussed in the second part of the literature review. Second, the literature review will cover techniques and strategies found in open literature that may lend themselves to the proposed EMF energy harvesting design including any research directly related to AC power line harvesting technology.

**Chapter 3** will begin with defining the proposed design based on information gathered from the literature review and scope sections. Fundamentals of operation will be described followed by some design optimization. To follow a complete analytical derivation of magnetic/EMF interaction and the dynamic models used to experimentally validate the harvesting unit will be outlined.

**Chapter 4** will begin with experimental methodology, followed by a complete model validations of the proposed design and discussion of the results.

**Chapter 5** will conclude the results obtained in Chapter 4 and make suggestions for possible future work in this subject area.

# Chapter 2

# Literature and Background

## 2.1 Energy Harvesting

Energy harvesting, or energy scavenging, has taken on variable definitions over the past few decades, however in the most broad terms it could be defined as the conversion of any ambient energy into stored energy for future use. Modern day applications tend to support a more specific definition as the conversion of ambient energy into electrical energy since energy storage is typically in the form of electrical energy [11]. Ambient energy is considered the wasted energy or byproduct energy found in the harvesting environment. Given that the focus of this work is to develop an energy harvester to be used to power electronics in the form of wireless sensor nodes, adoption of the more specific definition tends to make sense. With energy harvesting properly defined, understanding the point of energy harvesting and of assessing the scale of the harvesting application is also important. The main goal of energy harvesting technology is typically cost driven although environmental advantages are also present. Harvesting technologies large and small mitigate power supply issues and offset costs in different ways. Large scale harvesting, or 'Green energy' technology, typically connects harvester mechanisms to the power grid which help offset local energy costs and places conventional fuel sources in less demand thus reducing carbon emissions. Small scale harvesting called 'energy harvesting' or 'energy scavenging', reduces costs differently by eliminating the need to run expensive cabling to remote locations and removing costs and complications related to battery replacement and maintenance. In addition to these items, both large and small scale harvesting technologies enjoy environmental advantages in the form of reduced waste and sustainability. For the subject of the present thesis, the case of energy harvesting is of small scale as described in section 1.2.

Table 2.1: Common Energy Harvesting Sources and Transduction Methods

| **Ambient Energy Source** | **Common Transduction Methods** |
|---|---|
| Vibration | Electrostatics<br>Electromagnetics<br>Piezoeletrics |
| Magnetic (magnetization, currents) | Electromagnetics |
| Thermal gradients | Thermoelectrics |

Small scale ambient energy applicable to wireless electronics can be found in a number of forms, some are more obvious than others, however the most common energy sources that are used practically to power small electronic devices are described in Table 2.1. Each of these energy sources can be converted to electrical energy using various transduction methods.

When considering the location of the proposed harvester, thermal gradients are a valid source of ambient energy, however the primary source of energy found surrounding a power transmission line is alternating electromagnetic fields. Moreover, although vibration energy is not a primary source of energy found amongst power transmission lines, given that the oscillatory in nature of the magnetic fields suggests the notion that vibration transduction methods may be of relevant interest. Lastly, magnetic energy is of course relevant however the primary method of transduction conveniently lends itself to both vibration and magnetic energy. For these reasons, research efforts have been aimed towards, kinematic energy harvesting methods which include piezoelectric, electromagnetic and electrostatic harvesting methods.

## 2.2 Literature Review

### 2.2.1 General Energy Harvesting Work

The field of energy harvesting is well documented with multiple review papers already published in recent years [7, 12–14]. However, exploring the general concepts pertaining to kinematic energy harvesting principals and novel optimization techniques is appreciable. The following transduction method are based on an inertial generator concept proposed by [15] which consists of a seismic mass, $m$, spring, $k$, and dashpot $c$ as shown in Figure 2.1.

As the generator is vibrated at the base, the mass moves relative to the outer housing which creates a net difference between the housing and the mass. The transducer can actually be modelled as the dashpot because the conversion of mechanical energy to electrical energy realistically dampens the mass motion. Obviously in real life additional system damping is present, however for the sake of understanding the following transduction methods this is a reasonable representation of piezoelectric, electromagnetic and electrostatic generator configurations. A more detailed overview for modeling the proposed work will be provided in Chapter 3.

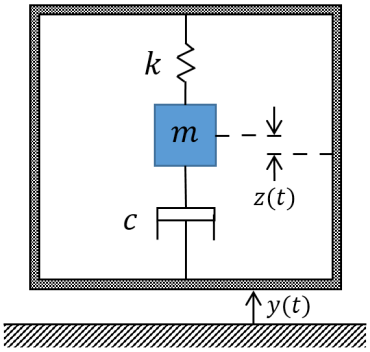


Figure 2.1: Inertial Generator Schematic

### Piezoelectric

Piezoelectric material is a special type of material that exhibits an electromechanical coupling. In general, when stress is applied, the material induces a strain and an electric displacement. Conversely when an electric field is applied an electric displacement and a mechanical strain is induced. These unique material characteristics allow piezoelectric material to be exploited for sensing, actuation and energy harvesting purposes. With that in mind, the amount of electromechanical coupling and the electrical output performance is dictated by material properties. Furthermore, piezoelectric material tends to be quite brittle and since electrical output is related to strain, mechanical properties also limit performance. With that in mind, piezoelectric material should be selected while considering these crucial aspects. Mechanical vibration energy can be easily converted to electrical energy using this transduction method under many different configurations. One of the most studied configuration of energy conversion is using a cantilever beam under transverse vibrations. For example, using piezoelectric material to harvest energy from human motion has been the focus of many researchers [16–18]. Preliminary designs using a cantilever

configuration were demonstrated by [16] to harvest human walking motion. In that work, a piezoelectric bimorph (active material on top and bottom) cantilever with tip mass was integrated into the heal of a shoe which is excited by human walking motion as shown in Figure 2.2. The various preliminary designs produced output power from $293 - 378\mu$W of power however characterizing the excitation of the walking motion has been challenging and makes optimization of such designs difficult.

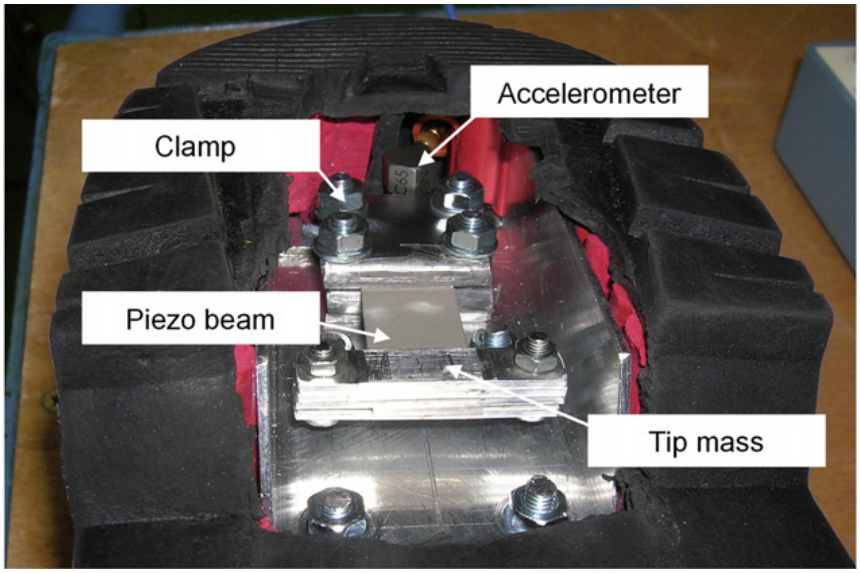


Figure 2.2: Piezoelectric Energy Harvester inside heel of shoe [16]

### Electromagnetic

Electromagnetic energy harvesting uses Faraday's law of induction as the principle method of energy transduction. In general terms, an electromotive force is induced in an inductor (coil of wire) while in the presence of changing magnetic flux. Relative motion between an inductor coil and a permanent magnet induces a voltage and current in the coil which can be harvested. Configurations that utilize this principle offer comparatively high output current levels with low voltages for low frequency applications [12]. Low voltage levels in harvesting applications tend to require additional power conditioning circuitry to step up voltage levels for rectification. A classic configuration was used by [19] to design the harvester shown in Figure 2.3. In this concept, a cantilever beam with permanent magnet tip mass surrounded a stationary coil. When the harvester was excited from mechanical

vibrations the cantilever would deflect and induce a voltage in the coil. The harvester resonated at 50Hz which produced approximately $3mW$ of AC power when excited by a $0.5m/s^2$ harmonic base input. Many researchers have used this transduction principal in various configurations for energy harvesting from ambient mechanical vibrations [20–23] as well as human motion [24].

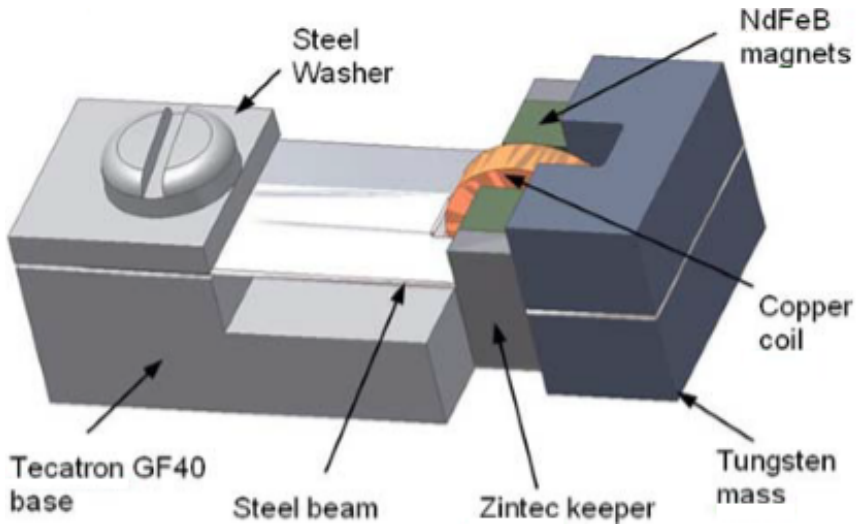


Figure 2.3: Eletromagnetic Energy Harvester [19]

**Electrostatic**

Another area of interest that has gain substantial attention is using electrostatic principals for energy harvesting. Due to their ease of integration there has been considerable attention from the MEMS (micro electro-mechanical systems) research community into electrostatic energy harvesting systems. The principal of electrostatic energy harvesting is through the use of variable capacitance. As two oppositely charged plates (separated by air, vacuum or insulator) are forced by mechanical vibrations against one another, a charge or voltage is produced which can be harvested. Three fundamental design concepts for MEMS fabrication were suggested and analyzed by [25]. Although electrostatic generators are popular in the MEMS community, they have a fundamental drawback in that energy density is low and a pre-charge voltage is required for operation [26]. An interesting example of electrostatic harvesting work was developed by [27]. A micro power generator for low frequency vibration harvesting applications was developed using electrostatic design concepts as shown in Figure 2.4. This generator allows for a 15mm travel range in the

direction of vibration while controlling the gap between electrode plates with micro-ball bearings (320$\mu$m). The resulting output power is 40$\mu$W with a 0.4G input at an extremely low frequency of 2Hz.

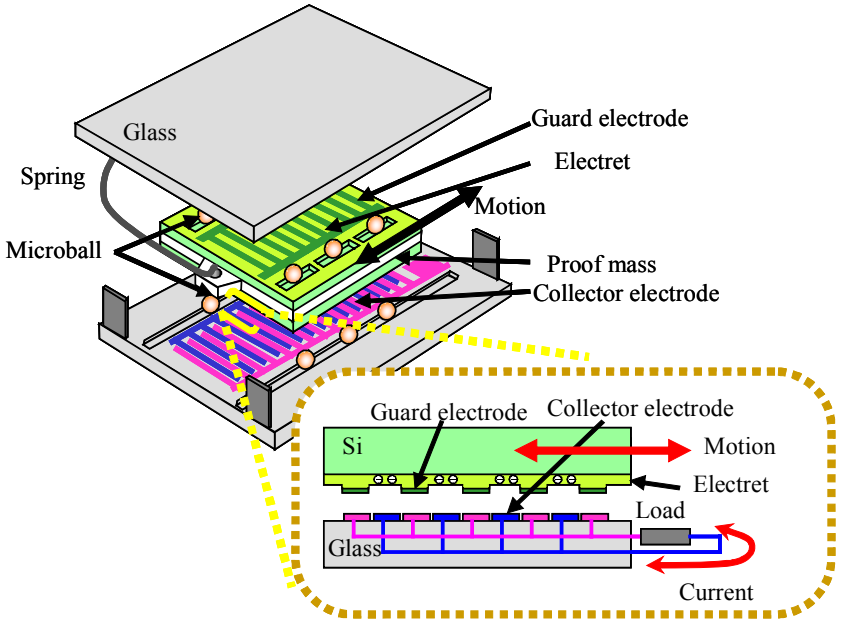


Figure 2.4: Eletrostatic Energy Harvester [27]

### Hybrid Devices

Searching for ways to increase power output and reduce size, some researchers have studied hybrid approaches towards kinematic energy harvesting. A hybrid approach uses a combination of one or more mechanical to electrical transduction methods to harvest energy. Combining piezoelectric with electromagnetic is one of the most studied hybrid harvesting methods [28–31]. Multiple voltage output signals however typically call for additional power conditioning which must be considered when estimating overall power. A hybrid configuration shown in Figure 2.5 combines piezoelectric and electromagnetic transduction mechanisms. Multiple piezoelectric layers (30$\mu$m) make up a cantilever with miniature dimensions of 22mm, 9.6mm and 0.65mm for length, width and thickness respectively. At the tip of the beam a permanent magnet is fixed to make up the electromagnetic tip mass.

During base excitation the cantilever deflects which creates strain in the piezoelectric material as well as a relative motion between the tip mass and the stationary coil. The axial strain in the cantilever may be harvested with piezoelectric material while the relative motion between the magnetic tip mass and coil induces current in the coil which may also be harvested. Power density was calculated for separate piezoelectric and electromagnetic circuits to be $790\mu\text{W}/cm^3$ and $0.85\mu\text{W}/cm^3$ respectively.

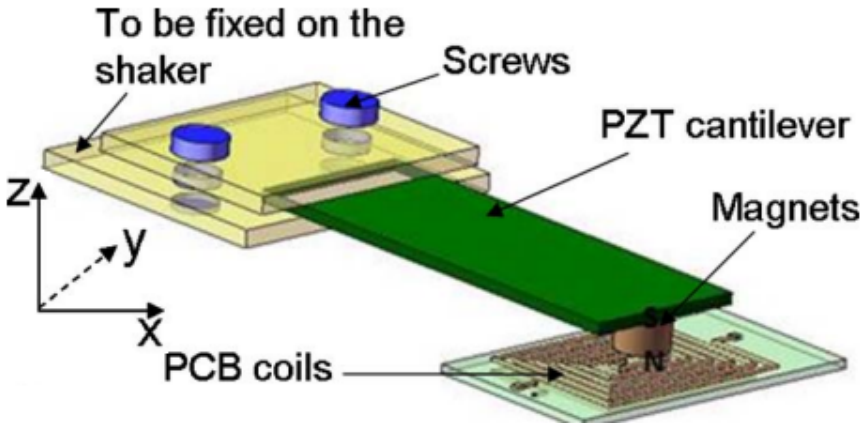


Figure 2.5: Hybrid Piezoelectric/Electromagnetic Energy Harvester [30]

**Wide-band Harvesting**

Another common approach to increasing overall power output from a harvester that has received substantial attention is wide-band harvesting. Typically harvesting systems are only able to harvest appreciable energy at the systems resonant frequency. Deviation from this frequency results in a substantial drop in power output from the harvester. This becomes a problem for systems that have drifting input frequencies which is the case for most ambient vibrations. Multiple methods have been found in literature to to account for these power drops including frequency tuning (active and passive), multimodal harvesting, frequency up-conversion and non-linear techniques (bistable and monostable). Frequency tuning approaches typically alter stiffness or mass of the system to shift the resonant frequency of the harvester. Active or semi-active tuning systems require additional energy or alternative voltage inputs from a tuning control systems which often reduce the overall energy harvested by the system [32, 33]. Conversely, passive adjustment tuning mechanisms do not draw additional system energy but do require human intervention to alter the optimal resonance frequency [34–36]. Passive systems may not be considered

wide-band systems however since the system does not actively harvest energy over a range of frequencies. Multimodal harvesting systems harvest energy in two different ways, the first is from multiple modes under hybrid scenarios where power is extracted at multiple frequencies from different transduction methods [37]. The second and most simplistic approach is to create an array of harvesters that all have adjacent resonance frequencies [38]. Frequency up conversion methods are used when the input frequency is drastically different than the harvesting frequency. In these cases, mechanical stoppers are often used to couple a low frequency output with a high frequency output to create a wide-band response [39]. Lastly non-linear techniques are used typically by involving non-linear stiffness mechanisms such as magnets to create bistable and monostable harvesting states which effectively widen harvesting ranges [40]. A simplistic representation of a multimodal harvester is depicted in Figure 2.6 studied by [38] where power is generated using electromagnetic induction principals. A central magnet is surrounded by four banks of cantilevers with coils embedded in them which are designed to resonate at adjacent frequencies to produce a broadband power output. This MEMS configuration was able to generate $0.4\mu$W of continuous power over a range of 800Hz at $10mV$ when excited at 4.2-5kHz frequency.

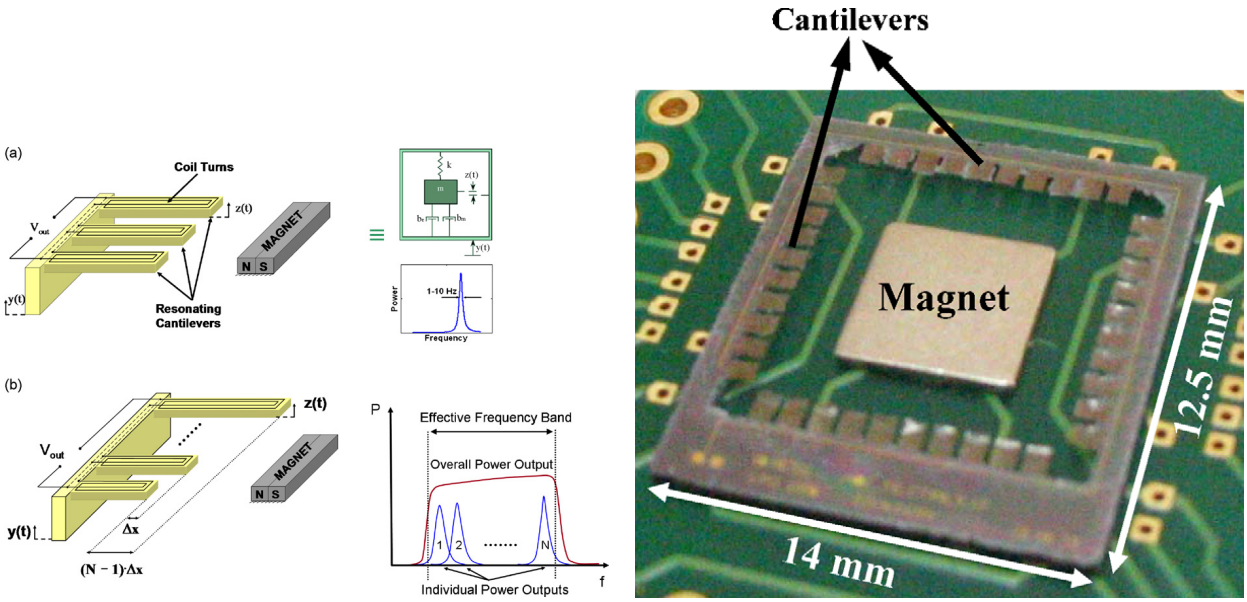


(a) Wide-band Cantilever Array Concept.

(b) Actual Wide-band Cantilever Device.

Figure 2.6: Wide-band Cantilever Array Concept and Device [38]

#### Summary

Based on the above overview of typical energy harvesting techniques, each transduction method has its own advantages and disadvantages, some of which have been highlighted in the foregoing overview. Further metrics and additional harvesting examples have also been highlighted in review papers [12,26]. A comprehensive overview has been provided in Table 2.2 based on general consensus found during literary review. Comparing harvesting methods can be an ambiguous task and so authors have done their best to compare harvesters and harvesting techniques in a manner that is conducive to all methods. However this can get rather difficult and confusing still when considering hybrid and wide-band harvesting. One of the primary metrics found readily in literature to compare harvesting configurations is 'energy density' or 'power density'. An energy density metric was derived and suggested by [41] with extensive further justification found in [42] to compare piezoelectric, electrostatic and electromagnetic methods. Using this method of comparison we can see in Table 2.3 that piezoelectric material maintains the highest effective energy density based on the assumptions made by [42]. In the table, $\sigma_y$ is the yield stress, $k$ is the coupling coefficient, $c$ is the elastic constant, $B$ is the magnetic field, $\mu_0$ is the permeability of free space, $\varepsilon_0$ is the permittivity of free space and E is the electric field.

### 2.2.2 Relevant Work

With a general foundation for kinematic energy harvesting described and the scope of this current work considered, it is believed by this author that exploring research through literature review can be narrowed to two primary sub-sections. First a review of relevant kinematic energy harvesting techniques that utilize piezoelectric principals. Thus to provide insight into novel configurations and modeling approaches found in open literature that may lend themselves to the proposed harvester design. And second, a review of recent work pertaining to AC transmission line monitoring/harvesting technology to get an idea of what has been successful. A review and discussion pertaining to these two areas will provide the needed insight into advantages/disadvantages of various configurations as well as suggest design opportunities that may be used for the proposed harvester.

#### Piezoelectric

Piezoelectric transduction has gained considerable attention from researchers in the field of energy harvesting in the past few decades. This is primarily due to the natural electromechanical coupling properties, high energy density, useful voltage output levels, and

Table 2.2: Inertial Generator Advantages & Disadvantages

| **Harvester Type** | **Advantages** | **Disadvantages** |
|---|---|---|
| Electrostatic | Expensive smart materials NA<br>Compatible with MEMS<br>Output voltages approx. 2-10V<br>High output at designed frequency | External charge (voltage) required<br>Capacitive<br>low energy density<br>Narrow bandwidth |
| Electromagnetic | Expensive smart materials NA<br>No external voltage source needed<br>High current output<br>High output at designed frequency | Bulky configuration (magnets & coil)<br>Low voltage output<br>difficult to integrate into MEMS<br>Narrow bandwidth |
| Piezoelectric | Highest energy Density<br>No external voltage source needed<br>Output voltages approx. 2-10V<br>High output at designed frequency | Brittleness with most materials<br>High output impedance<br>Depolarization<br>Narrow bandwidth |
| Hybrid | Multiple energy sources<br>increased voltage output levels | Increased fabrication complexity<br>Less mature |
| Wide-band | Wide-band power output<br>multiple techniques available | NA for specific driving frequency |

ease of fabrication as outlined in Table 2.2. One of the most widely researched configurations in the field of piezoelectric energy harvesting is a cantilever beam under base excitation. Many variations of this model have been developed including single-degree-of-freedom (SDOF) models, distributed parameter models and eventually closed form analytical models [15, 41, 43–45]. These various models provide insight into potential modeling approaches for the proposed work.

A bimorph cantilever beam with tip mass design under base excitation was suggested and modelled by [41] as depicted in Figure 2.7. A cantilever configuration was selected for its low resonance frequency and high average strain for a given force input when compared to other boundary conditions (fixed-fixed, pinned-pinned, etc.). In this analytical model, the mass was assumed to be a concentrated tip mass, rotational moment of inertia effects due to tip mass were ignored and the distributed mass of the beam was neglected. These seem to be fair assumptions when considering the $1cm^3$ volume of the harvester. In this configuration, the input force is applied to the base of the structure via external harmonic vibrations (60-200Hz) to produce strain along the length of the beam. Due to the electromechanical coupling properties of the piezoelectric material used to fabricate the beam, an electric displacement is also produced which can then be harvested. In the experimentally tested design as seen in figure, a power output of $375\mu$W was generated from a $2.5m/s^2$, 120Hz vibration source which seemed to be in good agreement with the analytical model.

Later on, further work was done to improve piezoelectric cantilever beam modeling in [44] which presented a closed-form analytical solution for a unimorph beam with no tip mass based on Euler-Bernoulli assumptions. The model also considered damping mechanisms (strain-rate and viscous air) which were modelled and experimentally validated in this work. Thereafter, the work was then embellished by the author in [45] for a bimorph beam with tip mass. Analytical solutions were derived and validated for both series and parallel piezoelectric configurations and both single-mode and multi-mode closed form expressions were demonstrated. Although power output under optimal load conditions for both series

Table 2.3: Inertial Generator Maximum Energy Densities [42]

| **Type** | **Energy Density** $mJ/cm^3$ | **Equation** | **Assumptions** |
|---|---|---|---|
| Piezoelectric | 35.4 | $(1/2)\sigma_y^2 k^2/2c$ | PZT 5H |
| Electromagnetic | 24.8 | $(1/2)B^2/\mu_0$ | 0.25T |
| Electrostatic | 4 | $(1/2)\varepsilon_0 E^2$ | $3 \times 10^7 V/m$ |

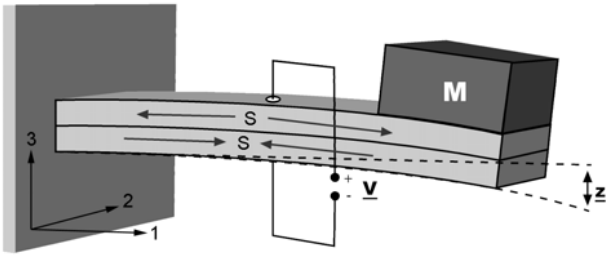


(a) Piezoelectric Cantilever Concept.

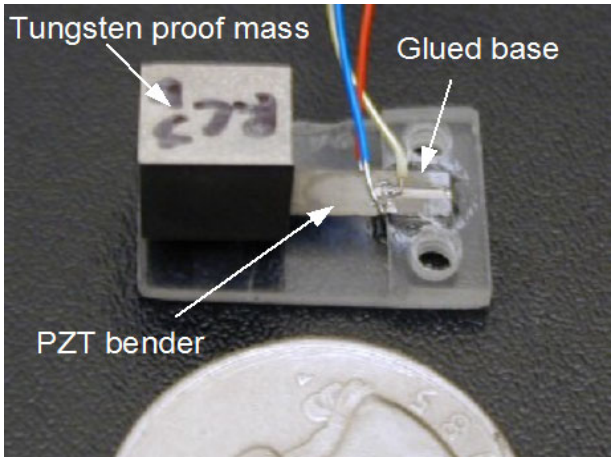


(b) Piezoelectric Cantilever Device.

Figure 2.7: Experimental Piezoelectric Cantilever with Tip Mass [41]

and parallel conditions were equal, series connection configuration provided higher voltage output levels. This becomes of interest when considering power rectification circuits that will be needed for DC power storage and use in future works.

In the aforementioned work, piezoelectric cantilever beam models were either of unimorph or bimorph configuration with piezoelectric material extending continuously from the fixed end to the tip of the beam. A similar Euler-Bernoulli modeling approach is taken for a cantilever beam with multiple step discontinuities in [46]. The framework for continuity conditions at partitioned points, proper mode shape derivation and orthogonality criterion is presented and then numerically validated. The model shows that the additional added mass and stiffness caused by the discontinuity in the beam are significant enough to justify the suggested exact method. Although a cantilever configuration in general provides high average strain as previously mentioned, the majority of the the induced strain is closest to the fixed end of the beam. This suggests that if a more cost effective harvester solution is required, it may be desirable to limit the amount of piezoelectric material to the fixed end of the beam rather then extend material to the tip where less appreciable strain exists. Furthermore, for low frequency harmonics where cantilever length is larger, a discontinuous cantilever beam which reduces overall stiffness may be necessary to meet size constraints for a given harvester design.

### AC Power Line Sensing/Harvesting

AC power transmission line energy harvesting has begun to draw significant attention from researchers. A non-invasive energy solution is an attractive method for providing a means of sustainability to wireless sensors found on power transmission lines. Since the most reliable source of energy found in the vicinity of power transmission lines is the alternating EMF (electromagnetic field) radiating from the lines, transduction methods that favor oscillatory motion and changing magnetic fields are the best options. However some electrostatic methods have also been realized [47, 48]. The transduction methods chosen by most engineers and researchers has been either electromagnetic induction for obvious reasons or piezoelectric configurations which utilize magnetic coupling though magnetic tip masses to induce strain on the piezoelectric material. These two transduction methods seem to be more practical solutions given their higher energy densities. A review of known literature will be done to further reveal potential design cues that may be of interest in the forthcoming design section.

Electromagnetic harvesting efforts utilize the changing electromagnetic field that is present along current carrying conductors to induce a current in a coil placed in close proximity to the wire. Traditionally what is know as a 'Power donut' has been employed to provide power to sensory devices located on power transmission lines [49]. However this system is quite large at 320 mm by 140 mm and weighs 9.2 kg which can cause transmission lines to sag substantially. Power donuts also require a difficult installation and routine maintenance after 5 years of operation. Alternative approaches have been made by [50–52] to address these issues however these designs still require additional circuitry to boost voltage levels. Ease of installation and size was addressed by [51] using an 'energy coupler' configuration. The 'energy coupler' consists of a multi-turn induction coil that is wound around a magnetic core made of highly permeable mu-metal. The design includes a small gap to allow the harvester to be easily wrapped around the transmission line rather than line disconnection or any pre-manufacturing processes. The magnetic core gap however reduces overall magnetic flux linkage and subsequently the harvester performance. Furthermore, the harvester voltage output highly dependent on the number of coil turns, diameter of the coil, number of core layers and the overall line coverage (width) of the harvester. These parameters all increase the size of the harvester. The harvester prototype shown in Figure 2.8 was made up of a 280 turn coil around 8 layers of mu-metal with a width, length and core thickness of 50mm, 45mm and 4mm respectively. This harvester proclaims 10mW of conditioned dc power to a 50 ohm load with 13.5A current passing through the wire at 60hz.

A similar technique used by [50] was studied to address flux leakage concerns that were

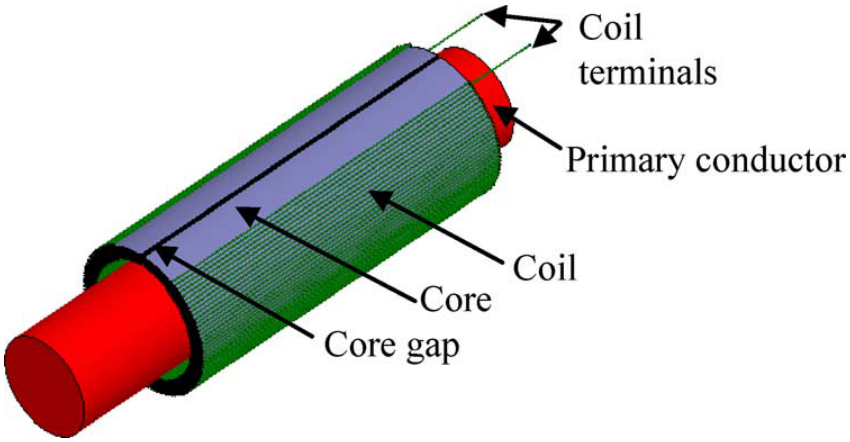


Figure 2.8: Electromagnetic Induction 'Coupler' Harvester - Power Lines [51]

also apparent in [51] design. A major shortfall of [51] design was the presence of the air gap used for ease of installation. The electromagnetic induction design shown in Figure 2.9 used a two magnetic C-cores that linked together via interlocking teeth. In this work, flux leakage was dramatically reduced by the eliminating the gap and increasing the number of interlocking teeth used to connect the C-cores. With this design, the installation can still be made without disrupting power to the line and flux losses are reduced by eliminating the gap. However core saturation is an issue with transformer type harvesters and these designs are more susceptible to line surges which could potentially damage follow on electronics connected tot he harvester.

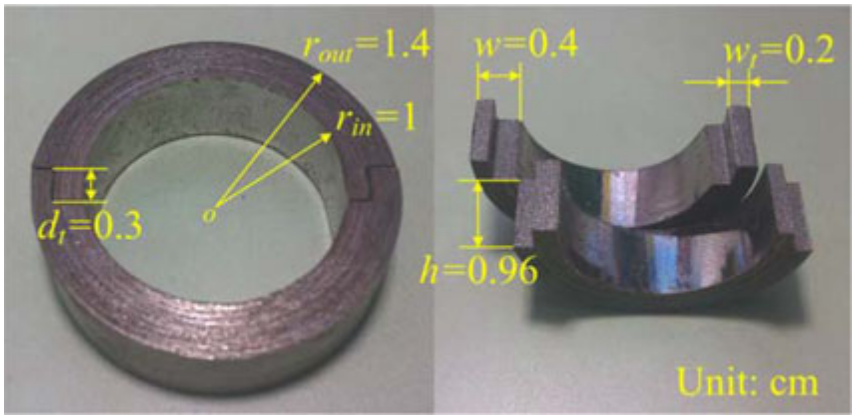


Figure 2.9: Electromagnetic Induction Optimization - Power Lines [50]

On another front, piezoelectric designs are gaining popularity. Piezoelectric transduction methods gained more popularity after many piezoelectric transmission line current sensor designs were studied [53–55]. Sensor design typically use cantilever configurations with magnetic tip masses which couple to the AC found in the power line. The flux radiating from the wire causes the cantilever to deflect producing a voltage from the piezoelectric layers proportional to the current in the wire. Another approach has been to use magnetostrictive material as the cantilever substrate to provide the sensory interaction to produce highly sensitive sensor outputs [56]. Piezoelectric cantilever harvesting designs seem to be a natural extension from similar sensor designs and benefit over electromagnetic designs given that they do not need to encompass the wire making for easy retrofitting.

For harvesting applications, the design of the cantilever is done to maximize output power by designing the harvester to resonant at the same frequency of the input which is 60Hz (50Hz in Europe). In [57] a cantilever harvester was designed using two axially poled disc magnets for tip mass. The cantilever beam tip was positioned over a two conductor appliance cord and the magnets on either side of the beam were adjusted until the beam resonated at the input frequency. Considering an appliance cord has two conductors separated by a small distance with AC currents operating theoretically 180 degrees of phase with one another, the resulting magnetic fields would be equal and opposite in sign. Based on this configuration, the magnetic fields partially cancel each other out. Analytical expressions for the resulting magnetic field are derived for two possible positions in which to place the cantilever tip while ignoring nonlinear magnetic field effects. The tested harvester had a length, width and thickness of 31.8mm, 3.2mm and 0.38mm with NdFeB disc magnets measuring 9.5mm in diameter and 1.6mm thick sandwiching the bimorph tip. The piezoelectric material extended continuously from the fixed end to the free end of the beam and no substrate was used. In this configuration, shown in Figure 2.10, a 13A current in the wire generated 345$\mu$W of power at an optimal load resistance of 491kohms. This work was later extended into a MEMS design which incorporated the above mesoscale harvester, a newly developed MEMS AC harvester and a current sensor [58]. And then once again [59] investigated fatigue stresses for a similar larger design in which the importance of maximizing the magnetic field potential in the direction of bending for the cantilever was underlined.

More intricate magnetic circuits were studied by [60, 61] in an attempt maximize the magnetic field acting perpendicular to the cantilever beams bending axis. In work done by [60], the piezoelectric bimorph cantilever energy harvester is designed to concentrate magnetic flux density on the power line thus to maximize reaction bending movement of the beam. Analytical expressions are developed for the force and voltage response of the harvester and experimentally validated. Based on 6A current and a resonant frequency

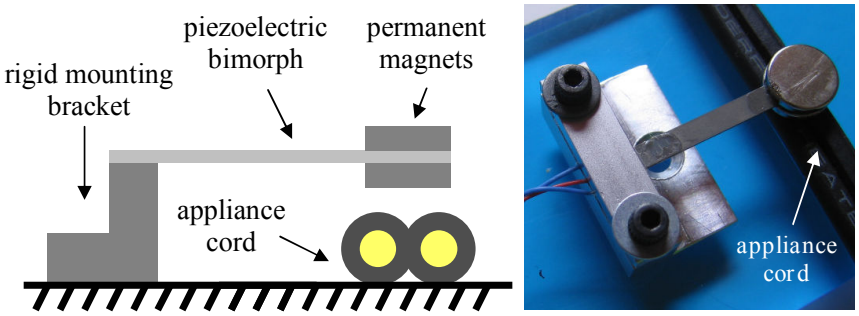


Figure 2.10: Piezoelectric Cantilever - Power Lines [57]

of 50Hz, the harvester generates 1.58mW of power with an optimal load resistance of 216kohms. This idea was later expanded by the same author in [61] to use what is know as 'Hallbach Array' magnet configuration which augments the magnetic field to one side of the magnetic tip mass. By doing so, the majority of the field energy is focused on the wire side of cantilever which creates greater force interaction resulting in increased power output densities by over 3 times. A schematic of the continuous unimorph cantilever harvester with Hallbach array is shown in Figure 2.11. Both single and double wire analytical models are derived and experimentally tested. For the case of the single conducting wire, a power of 566$\mu$W was generated across an optimal load of 196kohms when placed 4mm from a conducting wire with 10A current.

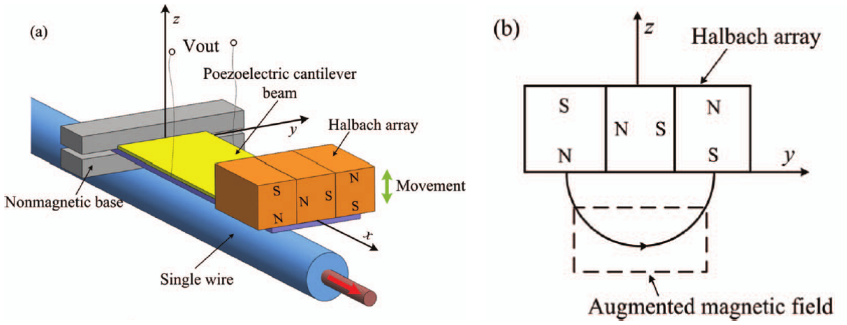


Figure 2.11: Piezoelectric Cantilever with Hallbach Magnet Array - Power Lines [61]

Finally, in current work by [62] a bimorph piezoelectric sensor design was developed for AC power transmission wire monitoring applications which utilized an amalgamation of two models by [46] and [44]. This work also considered magnetic orientation optimization for a single neodymium magnet to optimize the sensor to have a highly linear response. The sensor was modelled as a discontinuous beam with two uniform sections which was

then incorporated into a similar analytical modelling approach taken by [44] to produce a closed form analytical solution for the sensors electromechanical behavior at resonance. The sensors sensitivity was also tested over a range of temperatures to determine if the materials selected would demonstrate reduced sensitivity under extreme weather conditions. A diagram and picture of the senor design are shown in Figure 2.12. A natural extension of this work is an accompanying energy harvester to provide power to the sensor and wireless transmission hardware contained in the wireless sensor node. The modelling approach used in this thesis was subsequently used to model to the sensor design by [62] which is quite similar in construction.

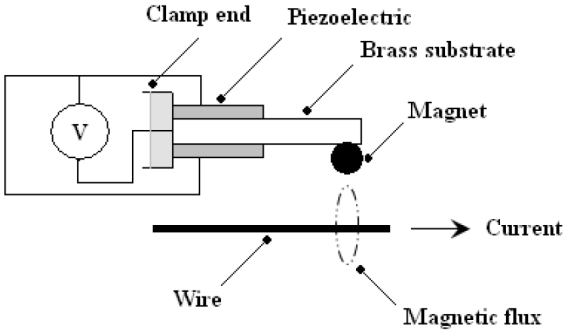


(a) Piezoelectric Cantilever Sensor Diagram.

Figures/Lao2.png

(b) Piezoelectric Cantilever Sensor.

Figure 2.12: Piezoelectric Cantilever Current Sensor [62]

### Summary

With respect to AC energy harvesting techniques the above work suggest that piezoelectric harvesting is a less invasive and more versatile harvesting technology. Electromagnetic coil based harvesters do not seem to have as strong of electromechanical coupling and require additional circuity to boost voltage levels to rectification levels. Piezoelectric transduction

produces voltages levels that can be fed into rectifying circuits directly with out the need for voltage multipliers. Furthermore, the need for encompassing the wire that is found with coil based harvester designs could be considered a nuisance. Piezoelectric based harvesters are also less susceptible to line surges and can be protected more easily with mechanical stops suggesting the risk of damaging follow on electronics is higher with coil based harvesters. The above literature has suggested some important things to consider when designing a piezoelectric energy harvester for AC line harvesting.

- Maximizing output per unit length can be done by selecting a bimorph over a unimorph cantilever beam configuration.
- Series electrical configuration should be chosen to boost direct voltage output levels to avoid additional circuitry.
- Piezoelectric material with a high coupling coefficient that is not too brittle to undergo the subjected strain induced from by line currents should be selected to increase voltage output.
- Magnet tip mass properties should have the highest remnant flux density to maximize magnetic charge density between magnet and and conducting line.
- In any design, orientation and placement of cantilever tip magnets should be done with care to ensure maximum magnetic field interaction.
- Air gap between wire and magnet should be reduced to a minimum to further increase magnetic flux density.
- Since resonance is a key factor for maximizing output from the harvester, accurate modeling of design parameters is important for obtaining a harvester that resonates at the designed frequency.
- Volume and cost of the harvester may be reduced by implementing a discontinuous section of piezoelectric material rather then extending material to the tip of the beam.

# Chapter 3

# Design and Modelling

In this chapter the harvester design concept will be outlined and explained. As mentioned in Chapter 2, the harvester design chosen to be studied in this thesis is an extension of the current sensor design done by [62]. The design concept and principle of operation will described followed design considerations to better understand the design requirements. Mathematical modelling necessary to describe the electromagnetic force interaction between current carrying conductor and a magnet will then be demonstrated and simulated for optimization. Based on the the force modelling results, a more detailed harvester design is described followed by material selection. Finally, the coupled mechanical equation of motion and electrical circuit equations are developed to produce the necessary frequency response functions of interest for this thesis.

## 3.1 General Design Concepts

### 3.1.1 Fundamental Principle of Operation

Based on the information gathered in the literature review portion of this thesis, a piezoelectric cantilever beam configuration was selected as the ideal harvesting method. The fundamental principle of operation is such that the harvester generates an alternating voltage output when mounted near an AC carrying conductor. The magnetic field which radiates from an AC carrying wire, interacts with the harvester's permanent magnet tip mass causing the beam to deflect. The deflection causes a strain in the piezoelectric material attached to the cantilever beam substrate. Due to the natural electromechanical coupling

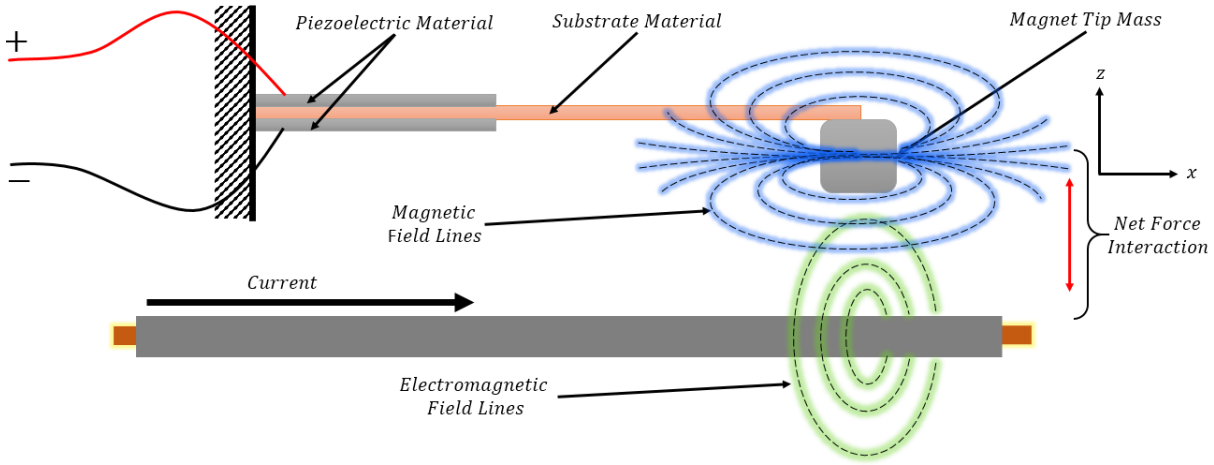


Figure 3.1: Fundamental design concept

properties found in piezoelectric material, an electric displacement is produced which is proportional to the strain along that section of the beam. A simplified representation of the design and concept is depicted in Figure 3.1.

### 3.1.2 Design Considerations

#### Permanent Magnet

Maximizing the force on the magnet will allow the harvester to be as efficient as possible. This can first be done (as suggested by the literature review) by maximizing the remanence (residual magnetic flux density) of the magnet. Additionally, the orientation of the magnet should be considered to ensure that magnetic flux density is maximized for the harvester design. This can be achieved through careful modelling and numerical simulation of different orientations to determine which is most optimal to maximize force on the magnet.

Another consideration is the overall size restrictions as outlined in the scope of this thesis. This places some constraints on the the size of the tip mass in terms of overall volume. Although maximum flux density is the primary concern, the density of the magnetic material must be considered as well. In order to achieve a low frequency of 60Hz and stay within the length constraint of 3cm, the density of the magnetic tip mass should also be maximized. This concern can also be mitigated by allowing the magnet to extend outward in the width direction beyond the width of the beam to increase mass while keeping the

mass location at the tip. However, if the magnet's width becomes too exaggerated then torsional vibrations due to asymmetric mounting may also become an issue for concern.

Attachment of the magnet to the beam will be done using an epoxy. The magnet must be aligned properly at the tip of the beam and remain attached during operation. A flat surface is desirable to ensure proper bonding as well as repeatable fabrication with minimal holding fixtures. Commercially available magnets provide the most accessible choice and are typically available in multiple geometries including, bar, cube, disc, cylinders, rings and spheres [63]. Of these geometries, bar and cube magnets are the only magnets without radial geometry to consider during harvester fabrication.

### Cantilever Beam

The first major design consideration when designing the harvesting beam is the harvesting material. Selecting a piezoelectric material that is both available and exhibits high electromechanical coupling is key. Effective energy harvesting requires careful material selection for the desired application. The substrate material should also be selected carefully to ensure minimal additional stiffness is added to the beam to ensure a low harvesting frequency of 60 Hz can be achieved. The substrate material must also be conductive and be resilient to repetitive applications of stress without plastic deformation.

To ensure the designed frequency is met during harvester fabrication a method of tuning is also required. Although the goal of this thesis is to analytically model the response of the system to a high degree of accuracy, sources of error are always present during fabrication which will have an effect on the harvesters fundamental frequency. For this reason a simple but effective means of making minor adjustments to the harvester during the experimental validation process is necessary. When considering the parameters that affect the frequency of a cantilever beam and the steps required to fabricate a harvester, adjusting length of the beam offers the most simplistic and least sensitive approach to tuning the harvester post fabrication. Adjusting thickness, epoxied tip mass or material parameters all seem to be impractical for a prototype design. Both modelling and design approaches should consider the effective length of the harvester as the variable parameter.

As mentioned in the scope of this work, cost effective harvesting is a priority considering the substantial number of harvesters needed to deploy large WSN's. For that reason, a model and design that maximizes electrical output per unit length and incorporates the opportunity to limit the amount of costly piezoelectric material on a given harvester is of interest. This can be done first and foremost by using a bimorph configuration as opposed to a unimorph configuration. In doing so, compressive and tensile strain on

both the top and bottom of the cantilever beam will be converted to useful electrical output thus maximizing the harvesting output per unit length of the beam. Secondly, in a cantilever design under transverse vibration, it is known from introductory mechanics that the strain profile decreases from the fixed end to the tip of the beam. This suggest that the effectiveness of the piezoelectric material towards the tip of the beam will be reduced as the strain at the tip of the beam goes to zero. A design such that piezoelectric material extends only partially down the length of the beam is of interest (discontinuous piezoelectric material). This type of design and model would allow for optimal piezoelectric material incorporation for a given application.

A final key design consideration that has been made is to build the harvester with a very small gap of just substrate exposed at the fixed end of the beam. The reason for this is actually three-fold. First, given the brittle nature of piezoelectric material, clamping down on the material in practice can easily cause cracking which could alter the boundary condition, distort the experimental results, and diminish the accuracy of the model. Secondly, given that cost has been highlighted as a key design parameter, if piezoelectric material were clamped at the fixed end, the piezoelectric material would need to extend into the clamping domain between the clamping pieces to provide a consistent and flat surface for clamping. This excess piezoelectric material between the clamps would not yield any additional power output and therefore is considered a waste of costly material. Lastly, the small gap at the fixed end provides a tuning region for minor frequency adjustment if required. For example, if the manufactured harvester happens to resonate at 59 or 61 Hz, small adjustments could then be made at the fixed and of the beam to achieve the designed frequency of 60 Hz which is crucial for maximum power output. This design consideration requires that a discontinuous beam modelling approach be adopted to include the varying stiffness and mass at each section of the beam given that the this type of configuration will have a large effect on the design frequency and overall length of the beam.

### Practical Boundary Conditions

The last thing to consider is designing practical boundary conditions. Since the validation of this is two fold as described in Section 3.4.1, the harvester will need to be mounted in two experimental positions. The harvester will first be mounted on an electrodynamic shaker for base excitation model validation. Followed by mounting on top of a separate experimental setup which will involve a current carrying wire. To effectively be mounted in both experimental set-ups, the boundary conditions must not change when switching from one test to the next. A clamping mechanism should be designed to allow for interchangeability between the two experimental set-ups to reduce sources of error and eliminate the

need to re-tune the harvester to 60 Hz during transition.

## 3.2 Electromagnetic Modelling

### 3.2.1 Electromagnetic Force Modelling

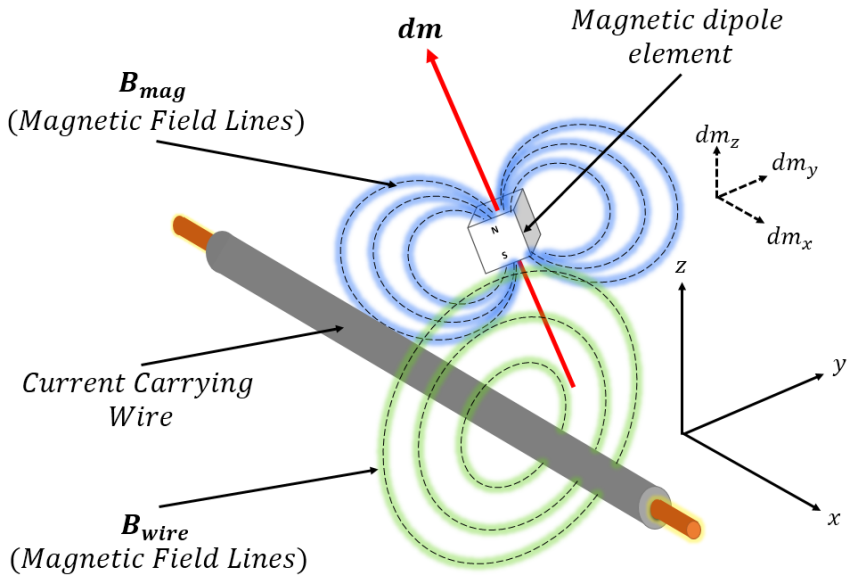


Figure 3.2: Magnetic dipole element near magnetic field of a current carrying wire

To model the force interaction between a permanent magnet and a current carrying conductor in the form of a power transmission line we must first consider the interaction between the magnetic fields produced by each as depicted in Figure 3.2. The magnetic force on a current carrying wire segment in the presence of an external magnetic field can be expressed as [64].

$$\mathbf{d}\boldsymbol{F} = I_0(\mathbf{d}\boldsymbol{l} \times \boldsymbol{B_{mag}}) \tag{3.1}$$

where $\mathbf{d}\boldsymbol{F}$ is the differential force on the current carrying element for a fixed current, $I_0$ is the magnitude of the current passing through the wire, $\mathbf{d}\boldsymbol{l}$ is the differential wire element vector(along the direction of current flow), and $\boldsymbol{B_{mag}}$ is the magnetic flux density of the magnetic field produced by the magnet. Bolded quantities here represent vectors in Cartesian coordinates. Conversely, the expression for the force on a magnetic dipole

element when placed in an external magnetic field is [64].

$$\mathbf{d}\boldsymbol{F} = \nabla(\boldsymbol{dm} \times \boldsymbol{B_{wire}}) \tag{3.2}$$

where $\boldsymbol{B_{wire}}$ is the time varying magnetic flux density from the magnetic field generated by the current carrying wire and $\boldsymbol{dm}$ is the magnetic moment of the magnetic dipole element which can be described as

$$\boldsymbol{dm} = dm_x\hat{\imath} + dm_y\hat{\jmath} + dm_z\hat{k} \tag{3.3}$$

where $dm_x$, $dm_y$ and $dm_z$ are the respective $x$, $y$ and $z$ components for any arbitrary dipole orientation. The magnitude of the dipole moment is

$$dm = \frac{B_r \mathrm{d}V}{\mu} \tag{3.4}$$

where $B_r$ is the remanence (residual magnetic flux density) of the magnetic material, $\mathrm{d}V$ is the differential volume of an element, and $\mu$ is the permeability constant of air. It can be seen from Eq. (3.4) that the remanence determines the overall strength for a given volume of magnetically poled material. Eq. (3.1) shows that for a fixed current the force on a current

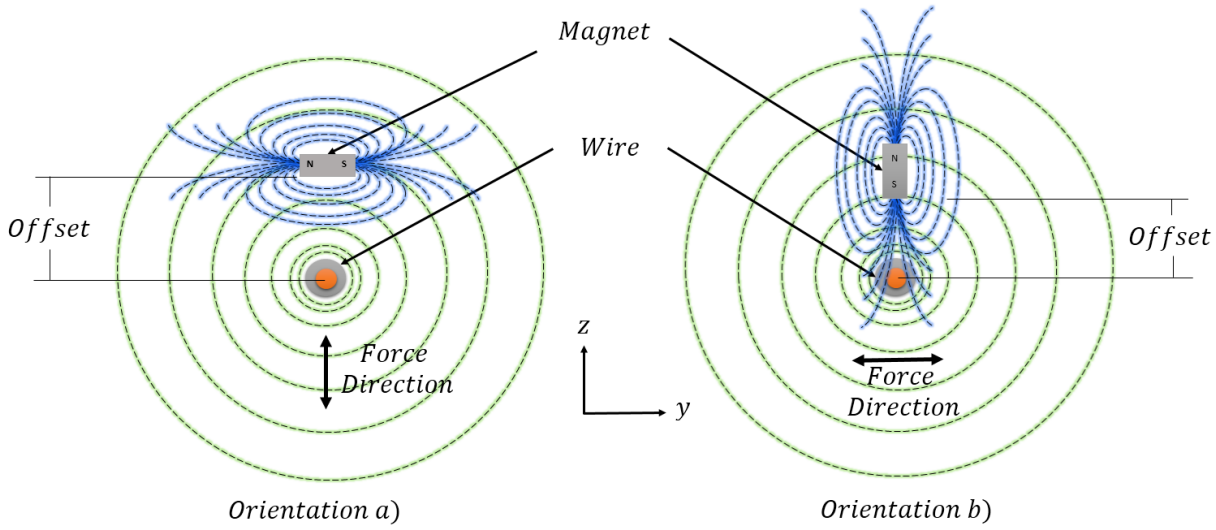


Figure 3.3: Magnetic field lines for magnet orientations a) and b)

carrying element can be maximized when the cross product of the external magnetic flux density and the current unit vector are at a maximum. If you consider a volume with an

uneven cross-sectional dimension, this can be successfully achieved by either of the two separate magnet orientations shown in Figure 3.3. The green and blue lines represent the magnetic field lines produced by the current carrying conductor and the permanent magnet respectively. Each orientation demonstrates the two extreme possibilities for the flux lines to be aligned. The flux lines of the magnet may either be tangential or perpendicular to flux lines of the current carrying wire as shown in orientations $a$) and $b$) respectively [62]. Any orientations in between these two options would only result in reduced overall magnetic flux density and asymmetric forces, which would be undesirable for a cantilever harvester design. Using the right hand rule and Eq. (3.1) the force directions for orientations $a$) and $b$) which is equal and opposite for magnet and wire have also been identified in Figure 3.3.

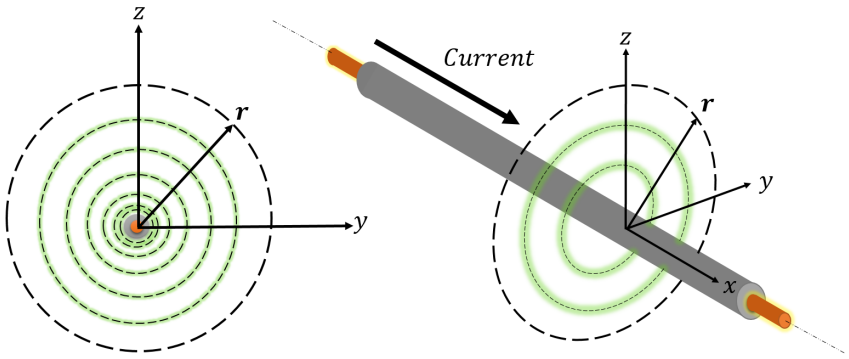


Figure 3.4: Normal and isometric views of the chosen coordinate system

Since the force of the magnet is equal and opposite to the force on the wire, Eq. (3.1) and (3.2) are both viable choices for obtaining an expression for the total force on the magnet. However for simplicity sake, Eq. (3.2) has been chosen to further develop the force expression. The following were developed based of the coordinate system shown in Figure 3.4 where $\boldsymbol{r}$ is the position vector or any point around the wire defined as $\boldsymbol{r} = y\hat{j}+z\hat{k}$. Considering that the wire is located along the $z$-axis with harmonic current amplitude, the current can be described

$$\boldsymbol{I} = I\hat{\imath} = I_0 \sin(\omega t + \theta)\hat{\imath} \tag{3.5}$$

where $I_0$ is the magnitude of the current flowing in the wire, $\omega$ is the frequency, $t$ is time and $\theta$ is the phase angle. Using Ampère's law,

$$\oint \boldsymbol{B} \cdot \mathrm{d}\boldsymbol{l} = \mu \iint \boldsymbol{J} \cdot \mathrm{d}\boldsymbol{S} = \mu I_{enclosed} \tag{3.6}$$

the magnetic field $\boldsymbol{B}$ around an infinitely long current carrying conductor can be expressed as

$$\boldsymbol{B_{wire}} = \frac{\mu}{2\pi r^2}(\boldsymbol{I} \times \boldsymbol{R}). \tag{3.7}$$

Considering the coordinate system chosen in Figure 3.4, Eq. (3.6) can be simplified to

$$\boldsymbol{B_{wire}} = \frac{\mu I}{2\pi}\frac{(-z\hat{\jmath} + y\hat{k})}{y^2 + z^2}. \tag{3.8}$$

The force differential volume of the magnetic element can be found using Eq. (3.2), Eq. (3.3), and Eq. (3.8)

$$\mathrm{d}\boldsymbol{F} = \frac{\mu I}{2\pi}\left[\frac{\partial}{\partial y}\left(\frac{-\mathrm{d}_y z + \mathrm{d}_z y}{y^2 + z^2}\right)\hat{\jmath} + \frac{\partial}{\partial z}\left(\frac{-\mathrm{d}_y z + \mathrm{d}_z y}{y^2 + z^2}\right)\hat{k}\right], \tag{3.9}$$

which further expands to

$$\boldsymbol{dF} = \frac{\mu I}{2\pi}\left[\left(\frac{\mathrm{d}_y(2yz)}{(y^2+z^2)^2} + \frac{\mathrm{d}_z(z^2-y^2)}{(y^2+z^2)^2}\right)\hat{\jmath} + \left(\frac{\mathrm{d}_z(-2yz)}{(y^2+z^2)^2} + \frac{\mathrm{d}_y(z^2-y^2)}{(y^2+z^2)^2}\right)\hat{k}\right]. \tag{3.10}$$

Based on the coordinate system chosen in Figure 3.4 and due to symmetry, the y-components of the force will cancel out for the magnet in orientation a) as shown in Figure 3.3. Furthermore, since the magnetic dipole moment in the $x$ and $z$-directions are zero, the force expression in Eq. (3.10) can be reduced using Eq. (3.4) to obtain the force on a differential volume element as

$$\mathrm{d}\boldsymbol{F} = \frac{IB_r \mathrm{d}V}{2\pi}\frac{(z^2-y^2)}{(y^2+z^2)^2}\hat{k}. \tag{3.11}$$

Similarly, using the same reasoning for orientation b) in Figure 3.3, Eq. (3.10) can be reduced to

$$\mathrm{d}\boldsymbol{F} = \frac{IB_r \mathrm{d}V}{2\pi}\frac{(z^2-y^2)}{(y^2+z^2)^2}\hat{\jmath}. \tag{3.12}$$

The force on the entire magnet can then be described from volume integrals using Eqs. (3.11) and (3.12) as

$$\boldsymbol{F_a} = \frac{IB_r}{2\pi}\iiint \frac{(z^2-y^2)}{(y^2+z^2)^2}\mathrm{d}V\hat{k} \tag{3.13}$$

$$\boldsymbol{F_b} = \frac{IB_r}{2\pi}\iiint \frac{(z^2-y^2)}{(y^2+z^2)^2}\mathrm{d}V\hat{\jmath} \tag{3.14}$$

where Eqs. (3.13) and (3.14) correspond to the force on the magnet for orientations a)

and b) respectively as denoted with subscripts [62]. These equations can then be used to identify which orientation produces largest total force on the magnet by evaluating the integrals numerically.

### 3.2.2 Magnet Material Selection

As described in the literature review section, and can be seen directly in Eqs. (3.13) and (3.14), an important design parameter is the remanence (residual magnetic flux density) or $B_r$ material constant for magnetic materials. Selecting a magnetic material with the highest remanence is crucial for maximizing the force on the magnet as it is directly proportional to the force on the magnet. However also considered here is the mass density of the magnetic material as suggested by the design considerations section as a secondary criteria for reducing overall length of the harvester. These two material parameters have been outlined in Table 3.1 for some of the most commonly used high strength magnets. The table identifies that Neodymium magnets offer the highest remanence constant while still maintaining the second highest mass density. Neodymium magnets from K&J Magnetics Inc [65] are the selected magnets for fabrication.

Table 3.1: Magnetic Material Properties

| **Material Type** | $\boldsymbol{B_r}$ **(kGs)** | **Density (g/cc)** | **Source** |
|---|---|---|---|
| Ferrite | 2.2 - 4.2 | 4.9 - 5 | Magnet Sales and Manufacturing Company [66] |
| Alnico | 7 - 13.5 | 6.8 - 7.3 | Magnet Sales and Manufacturing Company [67] |
| Neodymium | ***11 - 14.5*** | 7.4 - 7.5 | K&J Magnetics Inc [65] |
| Samarium Cobalt | 8 - 11.6 | ***8.2 - 8.4*** | Magnet Sales and Manufacturing Company [63] |

### 3.2.3 Magnet Orientation Selection

Based on some of the design considerations mentioned in Section 3.1.2 it is important to consider magnet orientation as a key design parameter to maximize the magnetic flux density and overall force acting on the magnet. This can be done by assigning geometric

and material parameters to the volume integrals in Eqs. (3.13) and (3.14) and simulating a normalized force with respect to current and magnet remanence. Based on the magnetic material and magnet manufacturer selected, a number of magnet geometries were selected for numerical simulation. With manufacturing simplicity considered, bar and cube magnets were chosen to be analyzed while maintaining a constant magnet cross-section and varying the width. Keeping with the same coordinate system as described in Figure 3.3 where the y-axis will be considered the width of the magnet, the results in Figure 3.5 display numerically integrated Eqs. (3.13) and (3.14) for three different sizes of commercially available magnets. All magnets maintained square edge cross-sectional dimensions of 3.175 mm while the widths were varied at 1.5875 mm, 3.175 mm, 6.35 mm, and 12.7 mm over a range of radial offset heights. The results demonstrate that the optimum orientation for the magnet depends on the dimensions of the magnet unless the magnet has a cube geometry and the width to square edge ratio is one. If the width dimension is increased larger than the square edge dimension then orientation a) has a distinct advantage. However if the width dimension is smaller than the square edge dimension orientation b) is advantageous. Overall it can be seen that magnets with a width to square edge ratio greater than one will generate higher force output values and that the radial offset distance should be minimized as much as possible.

Based on these numerical results, orientation a) will be selected for three reasons. In practice, orientation a) allows for mounting the cantilever directly above the transmission line for a more simple design. If orientation b) were mounted in this way, a second magnet would be required to make the magnetic forces symmetric to reduce torsional vibrations. Secondly, orientation a) demonstrates the higher force values when the width to square edge ratio is greater than one. Lastly, keeping in mind design considerations outlined in section 3.1.2, it is ideal to increase volume and mass in the width direction on the beam to locate the tip mass as close to the tip as possible.

## 3.3 Harvester Design & Beam Material Definition

### 3.3.1 Harvester Design

Using the design criteria gathered in foregoing sections, a schematic drawing of the proposed energy harvester is shown in Figure 3.6. As depicted, the harvester is a cantilever piezoelectric bimorph with a magnetic tip mass positioned in the optimal configuration (orientation a). The magnet geometry utilizes a width to square edge ratio to allow for increased tip mass to reduce overall size of the harvester as well as increase force output. The

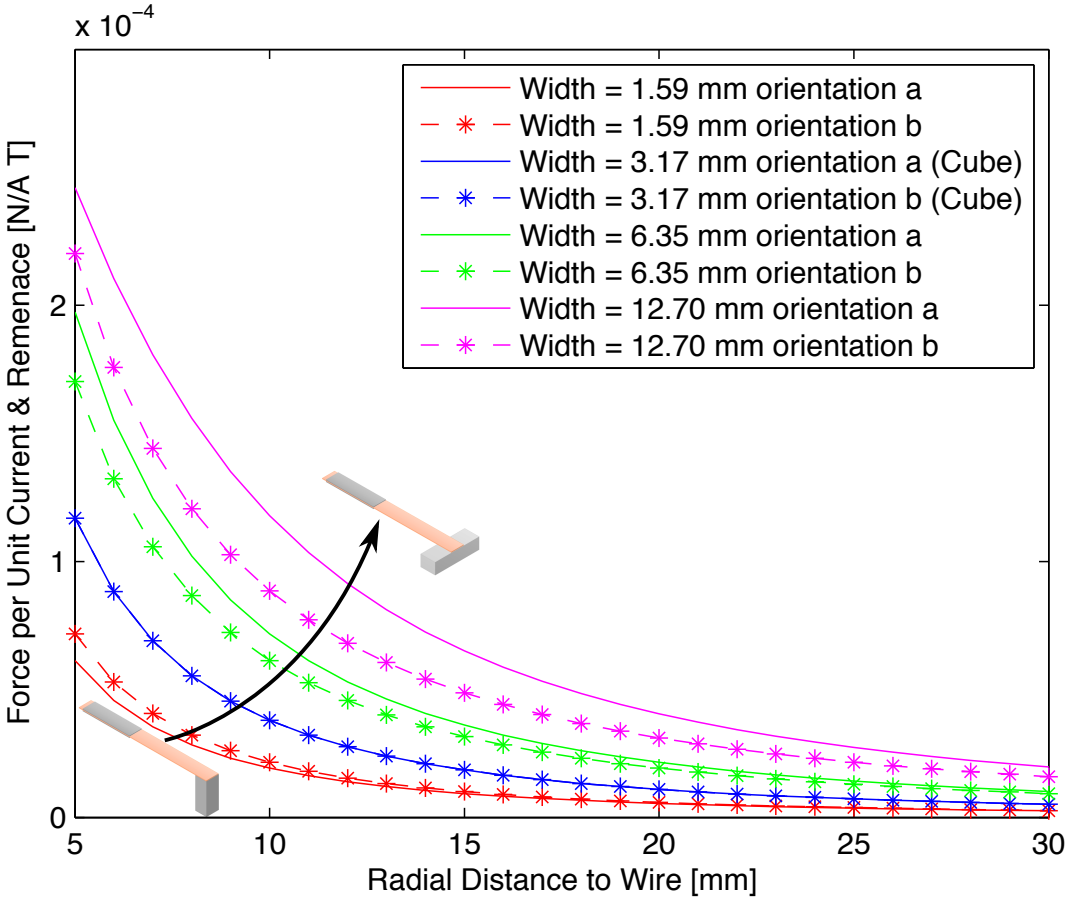


Figure 3.5: Theoretical Force - Normalized with current and residual flux density.

bimorph design includes a section of piezoelectric material near the fixed end (non-uniform beam) to reduce harvester frequency and allow for optimization in the form of reducing the harvesting material to only the amount needed to support follow on electronics. A small gap at the fixed end of the harvester has been added to provide a means of tuning, reducing wasted harvesting material, and eliminate damage to prototypes during clamping at the fixed end. The schematic also identifies a series electrical connection to obtain the highest voltage output to avoid additional electronics needed to bring voltage outputs to appreciable levels for power conditioning.

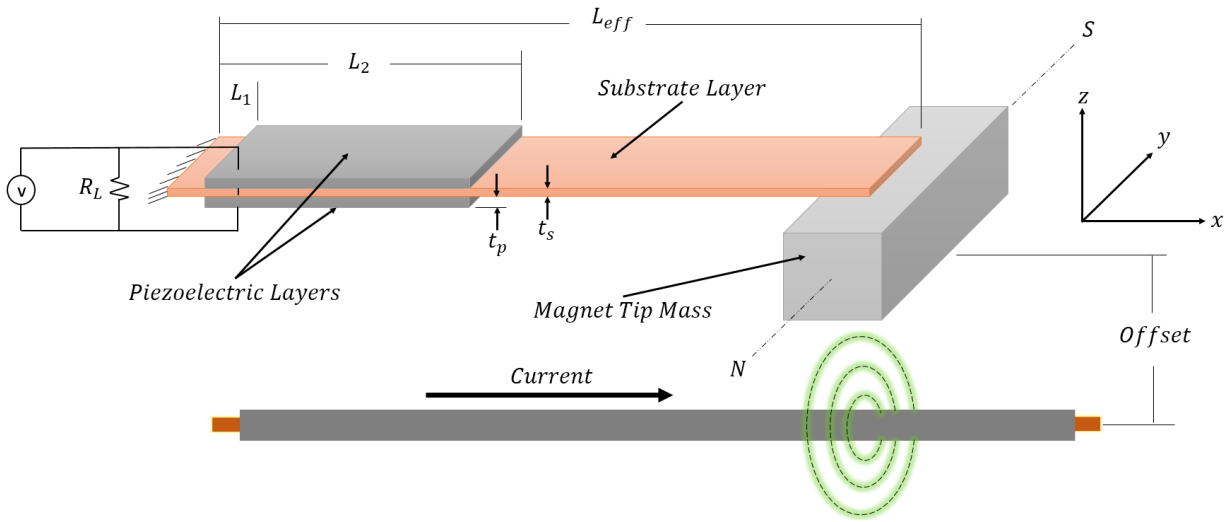


Figure 3.6: Schematic Diagram of the cantilever beam energy harvester

### 3.3.2 Beam Material Modelling and Selection

#### Piezoelectric Modelling and Material Selection

In general terms and under mild assumptions, piezoelectric material can be described as a linear elastic and linear dielectric material that exhibits electromechanical coupling. Hooke's Law describes linear elastic behavior as $\boldsymbol{T} = \boldsymbol{cS}$ where $\boldsymbol{S}$ is a dimensionless strain tensor, $\boldsymbol{T}$ is a stress tensor in units $N/m^2$, and $\boldsymbol{c}$ is elastic modulus matrix with units $N/m^2$. Furthermore, basic electronics theory describes linear dielectric behavior as $\boldsymbol{D} = \boldsymbol{\varepsilon E}$ as the relationship between $\boldsymbol{D}$, an electric displacement vector in units $C/m^2$ and $\boldsymbol{E}$, an electric field vector with units $V/m$ through $\boldsymbol{\varepsilon}$ a matrix of dielectric permittivity material constant in units of $F/m$. Combining these two relationships into matrix form and coupling them through $\boldsymbol{e}$, a matrix of piezoelectric coupling coefficients and its transpose $\boldsymbol{e'}$, which has units $C/m^2$ describes the linear constitutive relationship for piezoelectric material. This becomes evident when examining the relationship for piezoelectric material in matrix form.

$$\begin{Bmatrix} \boldsymbol{T} \\ \boldsymbol{D} \end{Bmatrix} = \begin{bmatrix} \boldsymbol{c}^E & \boldsymbol{e} \\ \boldsymbol{e'} & \boldsymbol{\varepsilon}^S \end{bmatrix} \begin{Bmatrix} \boldsymbol{S} \\ \boldsymbol{E} \end{Bmatrix} \tag{3.15}$$

Observations can be easily made when examining the constitutive relationship in this form. The total electric displacement is a summation of the electric field and mechanical stress applied (piezoelectric effect). Likewise, the total strain induced is a summation of

both the mechanical stress as well as electric field applied (inverse piezoelectric effect). This electromechanical coupling is due to the off-diagonal $\boldsymbol{e}$ terms, which if increased produce greater coupling and when decreased to zero produces no coupling at all. This demonstrates that the piezoelectric coefficient is an important material parameter when comparing different types of piezoelectric material and their relative coupling strengths. The superscripts $E$ and $S$ represent material constants measured under constant electric field $\boldsymbol{E}$ and constant strain $\boldsymbol{S}$. The nomenclature here has been adopted from [68] as commonly done to avoid confusion between mechanical and electrical domain variables. The reader is referred to [11] and [69] for detailed derivation of piezoelectric material.

For a thin cantilever beam configuration subjected to transverse vibrations with the coordinate system suggested in Figure 3.6, Eq. (3.15) can be reduced to the following equation where $1, 2$, and $3$ correspond to $x, y$, and $z$ axis as defined in Figure 3.6.

$$\begin{Bmatrix} T_1 \\ D_3 \end{Bmatrix} = \begin{bmatrix} c_{11}^E & e_{31} \\ e_{13} & \varepsilon_{33}^S \end{bmatrix} \begin{Bmatrix} S_1 \\ E_3 \end{Bmatrix} \tag{3.16}$$

Under transverse vibrations, the specific material constants of interest for energy harvesting become more visible and we can see that $c_{11}^E$, $e_{31}$, and $\varepsilon_{33}^S$ are important material parameters to consider when selecting piezoelectric harvesting material. Generally speaking, the primary goal is to harvest the most amount of electrical energy per given mechanical input which is an indication that the piezoelectric coupling coefficient $e_{31}$ is the most important variable. The piezoelectric $e_{31}$ coefficient is related to the more widely used $d_{31}$ piezoelectric strain coefficient as $e_{31} = d_{31}/s_{11}^E$. Where $s_{11}^E = 1/c_{11}^E$ which is simply the inverse of Young's modulus. Also $\varepsilon_{33}^S$ can be related to $\varepsilon_{33}^T$ as $\varepsilon_{33}^S = \varepsilon_{33}^T - d_{31}^2/s_{11}^E$. Although many piezoelectric materials have been studied, the most widely used piezoelectric material for energy harvesting applications is Lead Zinconate Titanate commonly referred two as PZT [11]. Of this type of piezoelectric material, two different grades, PZT-5A and PZT-5H are the most effective and readily available for academic energy harvesting research. Although material parameters tend to vary between manufacturers, various relevant material parameters found in [11] and compared in Table 3.2. Based on the data presented, from simple comparison, the piezoelectric coefficients $d_{31}$ and $e_{31}$ for PZT-5H are greater than PZT-5A. However this does not necessarily imply greater power generation because the stiffness of the material also affects the amount of electromechanical coupling [70]. Based on a comparative study done by [70] which compared PZT-5H and PZT-5A bimorph uniform cantilevers, theoretical results suggest dynamic flexibility (from elastic compliance values) plays a strong role in the amount of power output a harvester can produce. Dynamic flexibility however is also affected by the load resistance in the harvesting circuit. If damping ratio and elastic compliance are held constant for both bimorphs of the same size, the

Table 3.2: Piezoelectric material properties

| Material Parameter Name | Representation | Units | PZT-5A | PZT-5H |
|---|---|---|---|---|
| Relative Dielectric Constant | $\varepsilon_{33}^{S}$ | $nF/m$ | *13.3* | *25.55* |
| | $\varepsilon_{33}^{T}$ | $\varepsilon^{T}/\varepsilon_{0}$ | *1730* | *3400* |
| Piezoelectric coefficients | $d_{31}$ | $pm/V$ | *-191* | *-300* |
| | $e_{31}$ | $C/m^2$ | *-5.5* | *-12.0* |
| Elastic Modulus | $c_{11}^{E}$ | $N/m^2$ | *61* | *60.6* |
| Elastic Compliance | $s_{11}^{E}$ | $m^2/N$ | *16.4* | *16.5* |
| Density | $\rho$ | $Kg/m^3$ | *7800* | *7800* |

fundamental frequency will match and produce similar power outputs. However the load resistance will differ between the two beams which ultimately affects output power. Based on the experimental study done by [70], for base excited cantilevers of the same width and natural frequency (short-circuit), the PZT-5A cantilever produced larger output power for a wide range of load resistance values. The damping ratio of the PZT-5A cantilever however was slightly lower than the PZT-5H cantilever (0.91% and 1.41% respectively) under short-circuit conditions. Furthermore, The PZT-5A cantilever in this study also demonstrated a 45% larger maximum power density than the PZT-5H cantilever despite having 42% larger $d_{31}$ piezoelectric coefficient than the PZT-5A material used in this study. Given these results, PZT-5A has been selected as the chosen material to use for modeling and experimental prototype testing.

### Substrate Modelling and Material Selection

When considering the design parameters of this work, the most important factor is to obtain a harvester within the size constraints that has a natural frequency of 60 Hz. Since the addition of a harvesting material which has the highest coupling is unavoidable, the intrinsic stiffness of material is also unavoidable. In order to minimize any additional stiffness from the substrate material, we must consider a material that is most suitable for achieving low natural frequencies. Consider the simple case of a uniform cantilever beam with a rectangular cross-section, the natural frequency is given by [71] is

$$\omega_r = \frac{1.875^2}{L}\sqrt{\frac{Yt^2}{12\rho}} \tag{3.17}$$

where $L$ is the length of the beam, $Y$ is Young's modulus, $t$ is the thickness and $\rho$ is the density. Eq. (3.17) demonstrates that for a constant length, the natural frequency is proportional to $\sqrt{\frac{Yt^2}{\rho}}$. The maximum tip deflection of a uniform cantilever beam is defined as

$$w_{tip} = \frac{FL^3}{3YI} \tag{3.18}$$

where $F$ is the tip force and $I$ is the area moment of inertia. Increased tip deflection ultimately results in reduced natural frequency and the stiffness of the beam $YI$ is inversely proportional to the maximum tip deflection. The moment of inertia for a rectangular cross-section is

$$I = \frac{wt^3}{12} \tag{3.19}$$

where $w$ and $t$ are the width and thickness of the beam respectively. If we rearrange Eq. (3.19) and consider a constant width, the required thickness of the beam to achieve stiffness $S = YI$ is

$$t = \left(\frac{12S}{wY}\right)^{1/3}. \tag{3.20}$$

Combining the proportional relationship $\sqrt{\frac{Yt^2}{\rho}}$ and (3.20) we can produce an expression for a fixed length, width and stiffness. The natural frequency a uniform cantilever beam with these constants is proportional to $\sqrt{Y^{1/3}/\rho}$. This identifies two important material parameters that can be used to determine a substrate material that will result in a low natural frequency.

The materials compared must also be conductive and non magnetic to ensure good electrical conductivity for the harvesting circuit to be effective and not interfere with the tip force. Three materials have been considered in Table 3.3 where the last column identifies that 510 Alloy Bronze is the most ideal material given this criterion. Furthermore, this type of bronze also happens to be ideal for applications that are subjected to repeated stresses with out plastic deformation which is also advantageous for the harvester design. Based on these results, 510 Alloy Bronze was selected at the substrate material to be used for the harvester design.

Table 3.3: Substrate material properties

| **Material** | **Young's Modulus,** Y (Pa) | **Density,** $\rho(g/m^3)$ | $\sqrt{\frac{Y^{1/3}}{\rho}}$ | **Source** |
|---|---|---|---|---|
| 6061 Aluminum | 68.9 x $10^9$ | 2.7 x $10^3$ | 1.23 | [72] |
| 260 Brass | 110 x $10^9$ | 8.5 x $10^3$ | 0.75 | [73] |
| 510 Bronze | 110 x $10^9$ | 8.8 x $10^3$ | ***0.74*** | [73] |

## 3.4 Coupled Mechanical Equation of Motion

### 3.4.1 Harvester Modelling Approach

To ensure accuracy and reduce error, a very systematic approach to modelling and experimental validation was taken. First the harvester will be excited via base excitation to more easily characterize the dynamics of the system. To follow the harvester will be mounted on a conducting wire and excited at the tip via EMF radiating from the wire. Practically speaking, laboratory base excitation from an electrodynamic shaker is the most ideal method to validate the resonant frequency of the protoype harvester. Advanced laboratory equipment allows for very controlled experimentation procedures. Furthermore, measuring voltage output from the harvester can be done quite easily and thus makes for an excellent way to experimentally determine the maximum power output resistance which will be described in the foregoing sections in better detail. Lastly, minor tuning of the harvester to the designed frequency is also more convenient given that the clamping mechanisms that attach to the shaker are more easily manipulated. For these reasons, a base excitation model and a tip electromagnetic force excitation model are developed. Both models however are the same but with alternate forcing function parameters which will be subsequently validated in the experimental section of this thesis.

### 3.4.2 Partial Differential Equation

In this thesis, the beam is non-uniform and thus non-constant coefficients are considered in the PDE to allow for the piezoelectric material to only be present at the designed location. Following the same analytical approach developed by [11] and building off work done in [62], the following model describes a discontinuous composite cantilever beam. The model uses Euler-Bernoulli beam theory assumptions which is reasonable given that the harvester will be fabricated to be a fairly thin beam compared to the overall length. Furthermore, beam deformations are assumed to be small which will exhibit linear material behavior. For this

model the internal and external damping mechanisms are considered in the form strain-rate and external air damping considered with separate damping coefficients. Consider the transverse displacement of a non-uniform cantilever beam bimorph with tip mass under base excitation [11].

$$-\frac{\partial^2 M(x,t)}{\partial x^2} + (c_s I)(x)\frac{\partial^5 w_{tot}(x,t)}{\partial x^4 \partial t} + c_a(x)\frac{\partial w_{tot}(x,t)}{\partial t} + m(x)\frac{\partial^2 w_{tot}(x,t)}{\partial t^2} = F_{ext}. \quad (3.21)$$

The total transverse displacement of the system at position $x$ and time $t$ is $w_{tot}(t)$. The coefficients $(c_s I)(x)$ and $c_a(x)$ are strain-rate and viscous air damping coefficients respectively. $L_{eff}$ is the effective length of the beam, $m(x)$ is the mass per unit length, and $M_t$ is the total tip mass which includes the magnet and substrate overlap. $F_{ext}$ is the external force applied to the system. Since piezoelectric material is only present in the second section of the beam the internal bending moment is broken up into piecewise functions as

$$M(x,t) = \begin{cases} w \int\limits_{-t_{\tilde{s}/2}}^{t_{\tilde{s}/2}} T_1^{\tilde{s}} z \mathrm{d}z & \text{if } 0 \le x \le L_1 \\ w \left( \int\limits_{-t_{\tilde{p}}-t_{\tilde{s}/2}}^{-t_{\tilde{s}/2}} T_1^{\tilde{p}} z \mathrm{d}z + \int\limits_{-t_{\tilde{s}/2}}^{t_{\tilde{s}/2}} T_1^{\tilde{s}} z \mathrm{d}z + \int\limits_{t_{\tilde{s}/2}}^{t_{\tilde{p}}+t_{\tilde{s}/2}} T_1^{\tilde{p}} z \mathrm{d}z \right) & \text{if } L_1 \le x \le L_2 \\ w \int\limits_{-t_{\tilde{s}/2}}^{t_{\tilde{s}/2}} T_1^{\tilde{s}} z \mathrm{d}z & \text{if } L_2 \le x \le L_{eff} \end{cases} \quad (3.22)$$

where $w$ is the width of the beam, $t_{\tilde{s}}$ and $t_{\tilde{p}}$ are the thicknesses of the substrate and piezoelectric material layers, respectively. Stress components along the $x$-direction are $T_1^{\tilde{s}}$ for the substrate material and $T_1^{\tilde{p}}$ for the piezoelectric material defined as

$$T_1^{\tilde{s}} = Y_{\tilde{s}} S_1^{\tilde{s}} \quad (3.23)$$

$$T_1^{\tilde{p}} = c_{11}^E S_1^{\tilde{p}} - e_{31} E_3 \quad (3.24)$$

where $Y_{\tilde{s}}$ is Young's modulus of the substrate material and $S_1^{\tilde{s}}$ is the axial strain component of the substrate. A superscript $\tilde{p}$ is used to denote elements related to the piezoelectric material while a superscript $\tilde{s}$ denotes the substrate. Assuming small deflections, the axial strain due to pure bending at a certain level $(z)$ from the neutral axis in a composite beam is also proportional to the curvature of the beam such that

$$S_1(x,z,t) = -z\frac{\partial^2 w_{tot}(x,t)}{\partial x^2}. \quad (3.25)$$

Given that a series connection has been chosen, the electric field component $E_3$ is derived from analyzing the circuit shown in Figure 3.6. Since the two piezoelectric layers are assumed to be identical in size, the voltage across them would be $v(t)/2$. Furthermore, given the series connection, the poling is such that the piezoelectric coupling coefficient $e_{31}$ has opposite signs for top and bottom layers which produce an additive voltage effect where

$$E_3 = -v(t)/2t_{\tilde{p}}. \tag{3.26}$$

Lastly, the piezoelectric coupling term in (3.24) is only a function of time such that the electrical term be multiplied by $[H(x-L_1)-H(x-L_2)]$ to survive the spatial differentiation where $H(x)$ is a Heaviside function [11]. With these considerations and substitution of Eq. (3.23),(3.24) and (3.25) into Eq. (3.22) the internal bending moment is also expressed in cases as

$$M(x,t) = \begin{cases} -YI(x)\frac{\partial^2 w_{tot}(x,t)}{\partial x^2} & \text{if } 0 \le x \le L_1 \\ -YI(x)\frac{\partial^2 w_{tot}(x,t)}{\partial x^2} + \vartheta v(t)[H(x-L_1) - H(x-L_2)] & \text{if } L_1 \le x \le L_2 \\ -YI(x)\frac{\partial^2 w_{tot}(x,t)}{\partial x^2} & \text{if } L_2 \le x \le L_{eff} \end{cases} \tag{3.27}$$

where

$$\vartheta = \frac{e_{31}w}{t_{\tilde{p}}}\left[\left(t_{\tilde{p}} + \frac{t_{\tilde{s}}}{2}\right)^2 - \frac{t_{\tilde{s}}^2}{4}\right] = e_{31}wn_{pzt}. \tag{3.28}$$

Electrical terms $v(t)$ is the voltage and $n_{pzt}$ is the distance from the neutral axis of the substrate to the neutral axis of the piezoelectric layer. $\vartheta$ is the backward electromechanical coupling for the series connected piezoelectric layers [11]. By substituting Eq. (3.27) into Eq. (3.21) we form the coupled beam equation for a series connection as follows.

$$\frac{\partial^2}{\partial x^2}\left[YI(x)\frac{\partial^2 w_{tot}(x,t)}{\partial x^2}\right] + (c_s I)(x)\frac{\partial^5 w_{tot}(x,t)}{\partial x^4 \partial t} + c_a(x)\frac{\partial w_{tot}(x,t)}{\partial t} + m(x)\frac{\partial^2 w_{tot}(x,t)}{\partial t^2} - \vartheta v(t)\left[\frac{\mathrm{d}\delta(x-L_1)}{\mathrm{d}x} - \frac{\mathrm{d}\delta(x-L_2)}{\mathrm{d}x}\right] = F_{ext}. \tag{3.29}$$

### 3.4.3 Undamped Natural Frequencies

In order to obtain the natural frequencies of the system due to transverse vibration, we first consider the free and undamped system

$$\frac{\partial^2}{\partial x^2}\left(YI(x)\frac{\partial^2 w_{tot}(x,t)}{\partial x^2}\right) = -m(x)\frac{\partial^2 w_{tot}(x,t)}{\partial t^2} \tag{3.30}$$

Assuming a solution that is separable in time and space domains, the response of the system can be described by a series of eigenfunctions (mode shapes) in the form

$$w_{tot}(x,t) = \sum_{r=1}^{\infty} \phi_r(x)\eta_r(t). \tag{3.31}$$

$\phi_r(x)$ is the $r$th mass normalized eigenfunction for an undamped free vibration, and $\eta_r(t)$ is the $r$th modal mechanical coordinate expression. By substituting Eq. (3.31) into Eq. (3.30), the eigenvalue equation is

$$\frac{\partial^2}{\partial x^2}\left(YI(x)\frac{\mathrm{d}^2\phi_r(x)}{\mathrm{d}x^2}\right)\Big/(m(x)\phi_r(x)) = -\ddot{\eta}_r(t)/\eta_r(t) = \omega_r^2 \tag{3.32}$$

where $\omega_r^2$ is the constant of separation while $\omega_r$ represents the $r$th modal frequency of the system. In this thesis, the beam has multiple uniform sections and the spatial ODE can be segmented into uniform piecewise sections [46]. In using this approach additional continuity conditions must be applied at adjoining sections. Consider the spatial part of Eq. (3.32) we obtain the following expression,

$$(YI)^{(n)}\frac{\mathrm{d}^4\phi_r^{(n)}(x)}{\mathrm{d}x^4} = \omega_r^2 m^{(n)}\phi_r^{(n)}(x) \tag{3.33}$$

where subscript $r$ represents the $r$th natural frequency and superscript $(n)$ represents the $n$th section of the beam. Eq. (3.33) can also be written in form,

$$\frac{\mathrm{d}^4\phi_r^{(n)}(x)}{\mathrm{d}x^4} = \beta_r^{(n)4}\phi_r^{(n)}(x) \tag{3.34}$$

where,

$$\beta_r^{(n)4} = \omega_r^2\frac{m^{(n)}}{(YI)^{(n)}} \tag{3.35}$$

and the frequencies of the system (short-circuit conditions) can be found using

$$\omega_r = \sqrt{\beta_r^{(n)4} \frac{(YI)^{(n)}}{m^{(n)}}} \tag{3.36}$$

As we can see from Eq. (3.35), $\beta$ values for each section of the beam are a function of the natural frequency of the system.

### 3.4.4 Boundary & Continuity Conditions

For the proposed cantilever harvester described in Figure 3.6 which has three segmented uniform sections, requires both boundary conditions and continuity equations to describe the system. The following boundary conditions describe the system.

At $x = 0$,

$$\phi_r^{(1)}(0) = 0 \tag{3.37a}$$

$$\left.\frac{\mathrm{d}\phi_r^{(1)}(x)}{\mathrm{d}x}\right|_{x=0} = 0 \tag{3.37b}$$

At $x = L_{eff}$

$$(YI)^{(3)} \frac{\mathrm{d}^2\phi_r^{(3)}(L)}{\mathrm{d}x^2} = \omega_r^2 I_t \frac{\mathrm{d}^2\phi_r^{(3)}(L)}{\mathrm{d}x^2} \tag{3.38a}$$

$$(YI)^{(3)} \frac{\mathrm{d}^3\phi_r^{(3)}(L)}{\mathrm{d}x^3} = -\omega_r^2 M_t \phi_r^{(3)}(L) \tag{3.38b}$$

$M_t$ is the mass of tip and the mass moment of inertia of the tip mass is

$$I_t = M_t \left[ \frac{L_{mag}^2}{6} + \left( \frac{t_{mag} + t_{\tilde{s}}}{2} \right)^2 \right] \tag{3.39}$$

where $L_{mag}$ and $t_{mag}$ are the length and thickness of the magnet. The bending stiffness for sections one and three are simply

$$(YI)^{(1)} = (YI)^{(3)} = Y_{\tilde{s}} \frac{w t_{\tilde{s}}^3}{12} \tag{3.40}$$

where $Y_{\tilde{s}}$ is Young's modulus of the substrate. For section two shown in Figure 3.7, which

is a composite beam, the bending stiffness is

$$(YI)^{(2)} = \frac{2w}{3}\left\{Y_{\tilde{s}}\frac{t_{\tilde{s}}^3}{8} + \tilde{c}_{11}^E\left[\left(t_{\tilde{p}} + \frac{t_{\tilde{s}}}{2}\right)^3 - \frac{t_{\tilde{s}}^3}{8}\right]\right\}. \tag{3.41}$$

Continuity conditions must also be satisfied such that displacement, slope, bending moment and shear force at adjacent sections of the beam are equal to satisfy continuity conditions [46]. The design in this thesis has a total of two discontinuous locations which require the following conditions.

At $x = L_1$

$$\phi_r^{(1)}(L_1) = \phi_r^{(2)}(L_1) \tag{3.42a}$$

$$\frac{\mathrm{d}\phi_r^{(1)}(L_1)}{\mathrm{d}x} = \frac{\mathrm{d}\phi_r^{(2)}(L_1)}{\mathrm{d}x} \tag{3.42b}$$

$$(YI)^{(1)}\frac{\mathrm{d}^2\phi_r^{(1)}(L_1)}{\mathrm{d}x^2} = (YI)^{(2)}\frac{\mathrm{d}^2\phi_r^{(2)}(L_1)}{\mathrm{d}x^2} \tag{3.42c}$$

$$(YI)^{(1)}\frac{\mathrm{d}^3\phi_r^{(1)}(L_1)}{\mathrm{d}x^3} = (YI)^{(2)}\frac{\mathrm{d}^3\phi_r^{(2)}(L_1)}{\mathrm{d}x^3} \tag{3.42d}$$

At $x = L_2$

$$\phi_r^{(2)}(L_2) = \phi_r^{(3)}(L_2) \tag{3.43a}$$

$$\frac{\mathrm{d}\phi_r^{(2)}(L_2)}{\mathrm{d}x} = \frac{\mathrm{d}\phi_r^{(3)}(L_2)}{\mathrm{d}x} \tag{3.43b}$$

$$(YI)^{(2)}\frac{\mathrm{d}^2\phi_r^{(2)}(L_2)}{\mathrm{d}x^2} = (YI)^{(3)}\frac{\mathrm{d}^2\phi_r^{(3)}(L_2)}{\mathrm{d}x^2} \tag{3.43c}$$

$$(YI)^{(2)}\frac{\mathrm{d}^3\phi_r^{(2)}(L_2)}{\mathrm{d}x^3} = (YI)^{(3)}\frac{\mathrm{d}^3\phi_r^{(3)}(L_2)}{\mathrm{d}x^3} \tag{3.43d}$$

### 3.4.5 Mode shapes for each section of the beam

Using the method of separation of variables [71] and adopting a piecewise approach [46] using Eq. (3.31) the following solution arises

$$\phi_r^{(n)}(x) = A_r^{(n)}\cos(\beta_r^{(n)}x) + B_r^{(n)}\cosh(\beta_r^{(n)}x) + C_r^{(n)}\sin(\beta_r^{(n)}x) + D_r^{(n)}\sinh(\beta_r^{(n)}x). \tag{3.44}$$

$A_r^{(n)}$, $B_r^{(n)}$, $C_r^{(n)}$, and $D_r^{(n)}$ are integration constants and are determined using boundary and continuity conditions for each mode of each section of the beam. For this work, three sections have been used as shown in Figure 3.7. The piecewise eigenfunctions are

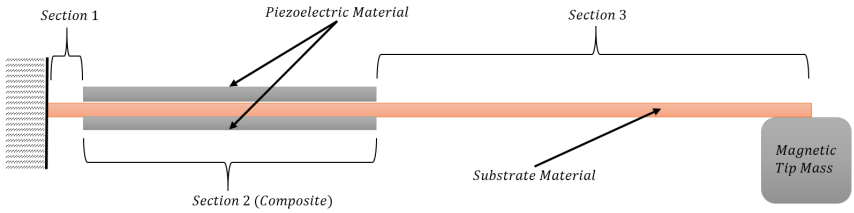


Figure 3.7: Uniform beam sections of energy harvester

$$\phi_r(x) = \begin{cases} A_r^{(1)}\cos(\beta_r^{(1)}x) + B_r^{(1)}\cosh(\beta_r^{(1)}x) + C_r^{(1)}\sin(\beta_r^{(1)}x) + D_r^{(1)}\sinh(\beta_r^{(1)}x) & \text{if } 0 \le x \le L_1 \\ A_r^{(2)}\cos(\beta_r^{(2)}x) + B_r^{(2)}\cosh(\beta_r^{(2)}x) + C_r^{(2)}\sin(\beta_r^{(2)}x) + D_r^{(2)}\sinh(\beta_r^{(2)}x) & \text{if } L_2 \le x \le L_2 \\ A_r^{(3)}\cos(\beta_r^{(3)}x) + B_r^{(3)}\cosh(\beta_r^{(3)}x) + C_r^{(3)}\sin(\beta_r^{(3)}x) + D_r^{(3)}\sinh(\beta_r^{(3)}x) & \text{if } L_2 \le x \le L_{eff} \end{cases} \tag{3.45}$$

Since the natural frequency $\omega_r$ is independent of each section of the beam, the various $\beta_r^{(n)}$ constants can be interrelated in terms of each individual $\beta_r$ value using the explicit expression described in Eq. (3.35) as $\beta_r^{(n)} = \beta_r \alpha_r^{(n)}$. Where $\alpha_r^{(n)}$ is described as

$$\alpha_r^{(n)} = \left(\frac{m^{(n)}(YI)^{(1)}}{m^{(1)}(YI)^{(n)}}\right)^{1/4} \tag{3.46}$$

such that $\alpha_r^{(1)} = 1$ and thus $\beta_r = \beta_r^{(1)}$

### 3.4.6 Characteristic Equation and Parameter Definition

By substituting general solutions Eqs. (3.45) into Eqs. (3.37), (3.38), (3.42) and (3.43) which make up the boundary and continuity conditions we form a characteristic equation matrix as

$$\boldsymbol{PQ} = 0 \tag{3.47}$$

where $\boldsymbol{P}$ is the characteristics matrix and $\boldsymbol{Q}$ is a vector of mode shape coefficients,

$$\boldsymbol{Q} = [A_r^{(1)}, B_r^{(1)}, C_r^{(1)}, D_r^{(1)}, A_r^{(2)}, B_r^{(2)}, C_r^{(2)}, D_r^{(2)}, A_r^{(3)}, B_r^{(3)}, C_r^{(3)}, D_r^{(3)}]^T. \tag{3.48}$$

In this thesis, the desired fundamental frequency of the harvester is known, $\omega_1 = 60$ Hz. Using a modified Eq. (3.35), the exact $\beta_1$ value can be determined as,

$$\beta_1 = \left(\omega_1^2 \frac{m^{(2)}}{(YI)^{(2)}}\right)^{1/4} \tag{3.49}$$

**Note:** *Any matching mass per unit length and bending stiffness values can be used since $\beta_r$ is independent of the beam section used for calculation as described by Eq.* (3.46).

Thereafter, by setting the determinant of the $\boldsymbol{P}$ matrix to zero $\det(\boldsymbol{P}) = 0$ we can evaluate for various system parameters. To determine the ideal length of the harvester to resonate at 60 Hz we can numerically evaluate using a reasonably small increment size for the desired effective length $L_{eff}$ as

$$\det(\boldsymbol{P}(L_{eff})) = 0 \tag{3.50}$$

since $\beta_1$ and $\omega_1$ are both known values. Then by substituting the newly found value for $L_{eff}$ into a similar variation of Eq. (3.50) we can determine the remaining $\beta_r$ solutions and corresponding $\omega_r$ values for the system as

$$\det(\boldsymbol{P}(\beta_r)) = 0. \tag{3.51}$$

In determining the $\beta$ values and setting the determinant of $\boldsymbol{P}$ to zero, mode shape coefficients $\boldsymbol{Q}$ are linearly dependent. The following orthogonality conditions are required to obtain unique solutions for these coefficients

$$\begin{aligned}\int_0^{L_1} \phi_r^{(1)}(x) m^{(1)} \phi_s^{(1)}(x)\mathrm{d}x + \int_{L_1}^{L_2} \phi_r^{(2)}(x) m^{(2)} \phi_s(x)\mathrm{d}x + \int_{L_2}^{L_{eff}} \phi_r^{(3)}(x) m^{(3)} \phi_s^{(3)}(x)\mathrm{d}x + \\ \phi_r^{(3)}(L_{eff}) M_t \phi_s^{(3)}(L_{eff}) + \left[\frac{\mathrm{d}\phi_r^{(3)}(x)}{\mathrm{d}x} I_t \frac{\mathrm{d}\phi_s^{(3)}(x)}{\mathrm{d}x}\right]_{x=L_{eff}} = \delta_{rs}\end{aligned} \tag{3.52}$$

where $\delta_{rs}$ is the Kronecker delta.

$$(YI)^{(1)} \int_0^{L_1} \frac{\mathrm{d}^2\phi_r^{(1)}}{\mathrm{d}x^2}\frac{\mathrm{d}^2\phi_s^{(1)}}{\mathrm{d}x^2}\mathrm{d}x + (YI)^{(2)} \int_{L_1}^{L_2} \frac{\mathrm{d}^2\phi_r^{(2)}}{\mathrm{d}x^2}\frac{\mathrm{d}^2\phi_s^{(2)}}{\mathrm{d}x^2}\mathrm{d}x + (YI)^{(3)} \int_{L_2}^{L_{eff}} \frac{\mathrm{d}^2\phi_r^{(3)}}{\mathrm{d}x^2}\frac{\mathrm{d}^2\phi_s^{(3)}}{\mathrm{d}x^2}\mathrm{d}x = \omega_r^2 \delta_{rs} \tag{3.53}$$

With the eigenfunctions completely defined, by substituting Eq. (3.31) into the discontinuous (non-constant coefficient) coupled beam PDE, Eq. (3.29), and applying orthogonality condition Eq. (3.52), the following mechanical equation of motion is defined in modal coordinates as

$$\frac{\mathrm{d}^2\eta_r(t)}{\mathrm{d}t^2} + 2\zeta_r\omega_r\frac{\mathrm{d}\eta_r(t)}{\mathrm{d}t} + \omega_r^2\eta_r(t) - \chi_r v(t) = f_r(t) \tag{3.54}$$

where $\zeta_r$ is the modal damping ratio and is dependent on the damping coefficients $c_s I$ and $c_a$. The modal damping ratio can easily be identified directly through experimental techniques (half power points) which simplifies the analysis by avoiding the necessity to identify physical damping constants. The electromechanical coupling term $\chi_r$ is defined as [11]

$$\chi_r = \vartheta\left[\frac{\mathrm{d}\phi_r(x)}{\mathrm{d}x}\bigg|_{x=L_2} - \frac{\mathrm{d}\phi_r(x)}{\mathrm{d}x}\bigg|_{x=L_1}\right] \tag{3.55}$$

## 3.5 Coupled Electrical Circuit Equation

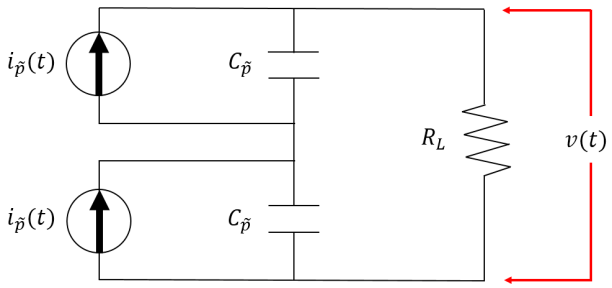


Figure 3.8: Electrical circuit representation of series connected bimorph harvester

Considering Eq. (3.16) described in section 3.3.2 we saw that for a thin cantilever beam subjected to pure bending, the electric displacement vector is reduced to the following scalar expression,

$$D_3 = e_{31}S_1^{\tilde{p}} + \varepsilon_{33}^S E_3, \tag{3.56}$$

where axial strain $S_1$ is the only source of mechanical strain. Observation of the electrical circuit in Figure 3.8 we see that the electric displacement from each piezoelectric layer can be modelled as a current source in parallel with the piezoelectric capacitance [11]. Since a series connection has been chosen, we see the load resistance $R_L$ is across both piezoelectric layers in series where voltage measurement would be made. Analyzing the circuit we can

obtain an expression for the current output from the integral form of Gauss's law [11] as

$$\frac{\mathrm{d}}{\mathrm{d}t}\left(\int_A \boldsymbol{D}\cdot\boldsymbol{n}\mathrm{d}A\right) = \frac{v(t)}{R_L} \tag{3.57}$$

where $\boldsymbol{D}$ is the electric displacement vector from the piezoelectric layers, $\boldsymbol{n}$ is the unit outward normal while integration is done over the electrode area A. This expression is however simplified given the electrodes perpendicularity to the 3-axis(z-axis). Using the expression for the average bending strain Eq. (3.25) and the uniform electric field potential Eq. (3.26), Eq. (3.56) can be combined with Eq. (3.57)to obtain

$$\frac{\varepsilon_{33}^S w(L_2-L_1)}{2t_{\tilde{p}}}\frac{\mathrm{d}v(t)}{\mathrm{d}t} + \frac{v(t)}{R_L} + e_{31}n_{\tilde{p}}w\int_{L_1}^{L_2}\frac{\partial^3 w_{tot}(x,t)}{\partial x^2\partial t}dx = 0 \tag{3.58}$$

where $w$, $t_{\tilde{p}}$, and $(L_2-L_1)$ are the width, thickness, and length of the piezoelectric layers. $n_{\tilde{p}} = (t_{\tilde{p}} + t_{\tilde{s}}/2)$ is the distance from the beam's neutral axis to the neutral axis of the piezoelectric layers [11]. By substituting the modal expansion from Eq. (3.31) into (3.58) we obtain,

$$\frac{\varepsilon_{33}^S w(L_2-L_1)}{2t_{\tilde{p}}}\frac{\mathrm{d}v(t)}{\mathrm{d}t} + \frac{v(t)}{R_L} + \sum_{r=1}^{\infty}\kappa_r\frac{\mathrm{d}\eta_r(t)}{\mathrm{d}t} = 0 \tag{3.59}$$

where $\kappa_r$ is the modal electromechanical coupling [11] term defined as

$$\kappa_r = e_{31}n_p w\int_{L_1}^{L_2}\frac{\mathrm{d}^2\phi_r(x)}{\mathrm{d}x^2}\mathrm{d}x = 0. \tag{3.60}$$

Applying Kirchhoff's circuit laws to the series circuit shown in Figure 3.8 we obtain

$$\frac{C_{\tilde{p}}}{2}\frac{\mathrm{d}v(t)}{\mathrm{d}t} + \frac{v(t)}{R_L} - i_{\tilde{p}}(t) = 0 \tag{3.61}$$

which can be directly related to Eq. (3.59) where $C_{\tilde{p}}/2$ is equal to the first part of the first term in Eq. (3.59) which is the internal capacitance of the piezoelectric material [11]. The internal capacitance is

$$C_{\tilde{p}}^{eff} = \frac{C_{\tilde{p}}}{2} = \frac{\varepsilon_{33}^S w(L_2-L_1)}{2t_{\tilde{p}}} \tag{3.62}$$

where $C_{\tilde{p}}^{eff}$ is the effective capacitance for a series bimorph. The third term in Eq. (3.59) is equal to the current source term

$$i_{\tilde{p}}(t) = -\sum_{r=1}^{\infty} \kappa_r \frac{\eta_r(t)}{dt} \tag{3.63}$$

Substitution of Eq. (3.62),(3.63) into Eq. (3.61) we obtain the final expression for the coupled electrical circuit as [11]

$$C_{\tilde{p}}^{eff} \frac{dv(t)}{dt} + \frac{v(t)}{R_L} - \sum_{r=1}^{\infty} \kappa_r \frac{\eta_r(t)}{dt} = 0. \tag{3.64}$$

## 3.6 Forcing Functions

Beam dynamics, electromechanical coupling, and electrical connections remain unchanged when comparing the base excited EMF model to a tip excited displacement model. The forcing function however takes on a different form as the input location has shifted from the base to the tip of the harvester and the harmonic force has completely changed. The two forcing function for both particular cases are developed here.

### 3.6.1 Base Excitation - Vibration

In the case where the harvester is subjected to base harmonic displacement, we must consider the fact that at the fixed end, the base displacement is not zero due to the harmonic motion at the base and therefore the total beam displacement at the fixed end is not zero. The beams total displacement will be a combination of the relative to the base displacement and the base displacement. By substituting the following relationship into the fixed end boundary condition we may determine the beams relative and total displacement.

$$w_{tot}(x,t) = w_{base}(x,t) + w_{rel}(x,t) \tag{3.65}$$

where $w_{base}(x,t)$ is the displacement of the base and $w_{tot}(x,t)$ and $w_{rel}(x,t)$ is the total and relative beam displacement with respect to the base. By setting the external force to

zero $F_{ext} = 0$ and substituting these relationships into the PDE Eq. (3.29) we obtain

$$\frac{\partial^2}{\partial x^2}\left[YI(x)\frac{\partial^2 w_{tot}(x,t)}{\partial x^2}\right] + c_s I(x)\frac{\partial^5 w_{tot}(x,t)}{\partial x^4 \partial t} + c_a(x)\frac{\partial w_{tot}(x,t)}{\partial t} + m(x)\frac{\partial^2 w_{tot}(x,t)}{\partial t^2} \\ -\vartheta v(t)\left[\frac{\mathrm{d}\delta(x-L_1)}{\mathrm{d}x} - \frac{\mathrm{d}\delta(x-L_2)}{\mathrm{d}x}\right] = -\left[m(x) + M_t\delta(x-L_{eff})\right]\frac{\partial^2 w_{base}(x,t)}{\partial t^2}. \tag{3.66}$$

where the right side of the equation will be considered the force acting on the system as

$$F(x,t) = -\left[m(x) + M_t\delta(x-L_{eff})\right]\frac{\partial^2 w_{base}(x,t)}{\partial t^2} \tag{3.67}$$

By substituting Eq. (3.31) into the coupled beam PDE, Eq. (3.66), and applying orthogonality conditions Eq. (3.52)(3.53), the mechanical forcing function in the form of translational base displacement (vibrations) can be expressed as

$$f_r(t) = -m^{(1)}\frac{\mathrm{d}^2 w_{base}(t)}{\mathrm{d}t^2}\int_0^{L_1}\phi_r^{(1)}(x)\mathrm{d}x - m^{(2)}\frac{\mathrm{d}^2 w_{base}(t)}{\mathrm{d}t^2}\int_{L_1}^{L_2}\phi_r^{(2)}(x)\mathrm{d}x \\ -m^{(3)}\frac{\mathrm{d}^2 w_{base}(t)}{\mathrm{d}t^2}\int_{L_2}^{L_{eff}}\phi_r^{(3)}(x)\mathrm{d}x - M_t\phi_r^{(3)}(L)\frac{\mathrm{d}^2 w_{base}(t)}{\mathrm{d}t^2}. \tag{3.68}$$

Considering a harmonic base displacement such that $w_{base}(t) = W_0 e^{j\omega t}$ where $W_0$ is the base displacement amplitude, $\omega$ is the excitation frequency, and j is an imaginary number. The forcing function can be expressed similarly such that $f_r(t) = F_r e^{j\omega t}$ where

$$F_r = \omega^2 W_0\left[m^{(1)}\int_0^{L_1}\phi_r^{(1)}(x)\mathrm{d}x + m^{(2)}\int_{L_1}^{L_2}\phi_r^{(2)}(x)\mathrm{d}x + m^{(3)}\int_{L_2}^{L_{eff}}\phi_r^{(3)}(x)\mathrm{d}x + M_t\phi_r^{(3)}(L_{eff})\right]. \tag{3.69}$$

### 3.6.2 Tip Excitation - Electromagnetic Force

In the case where the beam is subjected to electromagnetic tip force excitation, unlike the base excitation the base will be fixed and require no such boundary condition manipulation

to determine the total beam displacement. The PDE in Eq. (3.29) takes the form

$$\frac{\partial^2}{\partial x^2}\left[YI(x)\frac{\partial^2 w_{tot}(x,t)}{\partial x^2}\right] + c_s I(x)\frac{\partial^5 w_{tot}(x,t)}{\partial x^4 \partial t} + c_a(x)\frac{\partial w_{tot}(x,t)}{\partial t} + m(x)\frac{\partial^2 w_{tot}(x,t)}{\partial t^2} - \vartheta v(t)\left[\frac{\mathrm{d}\delta(x-L_1)}{\mathrm{d}x} - \frac{\mathrm{d}\delta(x-L_2)}{\mathrm{d}x}\right] = -\frac{\partial}{\partial t}\left[F(t)\delta(x-L_{eff})\right], \tag{3.70}$$

where $F(t)$ is the applied magnetic force at the tip of the beam. By substitution of Eq. (3.31) into the above equation we realize

$$\frac{d^2\eta_r(t)}{dt^2} + 2\zeta_r\omega_r\frac{d\eta_r(t)}{dt} + \omega_r^2\eta_r(t) - \chi_r v(t) = f_r(t). \tag{3.71}$$

Since current in the conducting wire is harmonic (AC current) and the force on the beam is proportional to the current in the wire as described by Eq. (3.13), the forcing function takes the form $f_r(t) = F_r e^{j\omega t}$ where

$$f_r = F_z \int \phi_r^{(3)}\delta(x - L_{eff})dx \tag{3.72}$$

is the amplitude of the force which becomes

$$F_r = F_z\phi_r^{(3)}(L_{eff}), \tag{3.73}$$

where $F_z$ in the $z$-direction. Based on the theoretical force analysis results shown in Figure 3.5 of section 3.2, orientation a) was selected as the optimal design for fabrication and thus force expression Eq.(3.13) will be used to determine the total force input at the tip of the beam. If we first consider the expression developed for magnet force acting in the $z$-direction as

$$F_a = F_z = \frac{I_0 B_r}{2\pi}\iiint \frac{(z^2-y^2)}{(y^2+z^2)^2}dV\hat{k} \tag{3.74}$$

or more simply

$$F_a = \frac{I_0 B_r}{2\pi}C_v \tag{3.75}$$

where $I_0$ is the current amplitude from Eq. (3.5) and $C_v$ is the volume integral constant. By substitution of Eq. (3.75) into (3.73) we obtain

$$F_r = \frac{I_0 B_r}{2\pi}C_v\phi_r^{(3)}(L_{eff}). \tag{3.76}$$

## 3.7 Closed-Form Steady State Responses & Frequency Response Functions

With the modal mechanical and electrical responses across a resistive load defined in Eq. (3.71) and (3.64) the steady-state responses can now be found. Considering both base and tip forcing functions are in the form $f_r(t) = F_r e^{j\omega t}$, the voltage response $v(t)$ and modal response $\eta_r(t)$ can also be transformed in a similar manner to the frequency domain as,

$$\begin{aligned} v(t) &= V e^{j\omega t} \\ \eta_r(t) &= H_r e^{j\omega t} \end{aligned} \tag{3.77}$$

### 3.7.1 Steady State Response

By substituting Eq. (3.77) into Eq. (3.71) and (3.64) to obtain [11]

$$\left(\omega_r^2 - \omega^2 + j2\zeta_r\omega_r\omega\right) H_r - \tilde{\chi}_r V = F_r \tag{3.78}$$

$$\left(\frac{1}{R_l} + j\omega C_{\tilde{p}}^{eff}\right) V + j\omega \sum_{r=1}^{\infty} \kappa_r H_r = 0 \tag{3.79}$$

The complex voltage response $v(t)$ can be obtained by substitution of Eq. (3.78) into Eq. (3.79) yields the steady-state voltage response of the bimorph [11]

$$v(t) = \frac{\sum_{r=1}^{\infty} \frac{-j\omega\tilde{\theta}_r F_r}{\omega_r^2 - \omega^2 + j2\zeta_r\omega_r\omega}}{\frac{1}{R_l} + j\omega C_{\tilde{p}}^{eff} + \sum_{r=1}^{\infty} \frac{j\omega\tilde{\theta}_r^2}{\omega_r^2 - \omega^2 + j2\zeta_r\omega_r\omega}} e^{j\omega t}. \tag{3.80}$$

since a series connection is chosen,

$$\hat{\theta_r} = \tilde{\chi_r} = \kappa_r. \tag{3.81}$$

Output power can then be calculated using Ohm's Law $p(t) = v(t)^2/R_L$ to produce steady-state power as

$$p(t) = \frac{1}{R_L}\left(\frac{\sum_{r=1}^{\infty}\frac{-j\omega\tilde{\theta}_r F_r}{\omega_r^2-\omega^2+j2\zeta_r\omega_r\omega}}{\frac{1}{R_l}+j\omega C_{\tilde{p}}^{eff}+\sum_{r=1}^{\infty}\frac{j\omega\tilde{\theta}_r^2}{\omega_r^2-\omega^2+j2\zeta_r\omega_r\omega}}e^{j\omega t}\right)^2. \tag{3.82}$$

Following a similar procedure, Eq. (3.79) can be substituted into Eq. (3.78) to obtain the steady-state modal mechanical response [11] as,

$$\eta_r(t) = \left(F_r - \tilde{\theta}_r\frac{\sum_{r=1}^{\infty}\frac{j\omega\tilde{\theta}_r F_r}{\omega_r^2-\omega^2+j2\zeta_r\omega_r\omega}}{\frac{1}{R_L}+j\omega C_{\tilde{p}}^{eff}+\sum_{r=1}^{\infty}\frac{j\omega\tilde{\theta}_r^2}{\omega_r^2-\omega^2+j2\zeta_r\omega_r\omega}}\right)\frac{e^{j\omega t}}{\omega_r^2-\omega^2+j2\zeta_r\omega_r\omega}. \tag{3.83}$$

To obtain the transverse displacement at point $x$ along the beam, Eq. (3.83) can be substituted into the mode summation equation Eq. (3.31) [11] to obtain

$$w_{rel}(x,t) = \sum_{r=1}^{\infty}\left[\left(F_r - \tilde{\theta}_r\frac{\sum_{r=1}^{\infty}\frac{j\omega\tilde{\theta}_r F_r}{\omega_r^2-\omega^2+j2\zeta_r\omega_r\omega}}{\frac{1}{R_L}+j\omega C_{\tilde{p}}^{eff}+\sum_{r=1}^{\infty}\frac{j\omega\tilde{\theta}_r^2}{\omega_r^2-\omega^2+j2\zeta_r\omega_r\omega}}\right)\frac{\phi_r^{(n)}(x)e^{j\omega t}}{\omega_r^2-\omega^2+j2\zeta_r\omega_r\omega}\right]. \tag{3.84}$$

where measurement distance $x$ along the beam must correspond with the $n$th section mode shape function $\phi_r^{(n)}(x)$.

### 3.7.2 Frequency Response Functions

To obtain frequency response functions (FRFs), we normalized expressions with respect to their particular inputs, translation base acceleration (for vibrations) or current through conductor (for EMF). To simplify this, we can re-define the forcing function $f_r(t) = F_r e^{j\omega t}$ appropriately for each input method.

**Base Excitation - Vibrations**

Redefining the forcing functions $f_r(t) = F_r e^{j\omega t}$ so that

$$F_r = -\sigma_r \omega^2 W_0 \tag{3.85}$$

where

$$\sigma_r = -\left[ m^{(1)} \int_0^{L_1} \phi_r^{(1)}(x)\mathrm{d}x + m^{(2)} \int_{L_1}^{L_2} \phi_r^{(2)}(x)\mathrm{d}x + m^{(3)} \int_{L_2}^{L_{eff}} \phi_r^{(3)}(x)\mathrm{d}x + M_t \phi_r^{(3)}(L_{eff}) \right] \tag{3.86}$$

allows the steady state voltage, power and transverse mechanical responses from Eq. (3.80)(3.82) and (3.84) to be re-expressed [11] as

$$v(t) = \alpha(\omega)\left(-\omega^2 W_0 e^{j\omega t}\right), \tag{3.87a}$$

$$p(t) = \psi(\omega)\left(-\omega^2 W_0 e^{j\omega t}\right)^2, \tag{3.87b}$$

$$w_{rel}(t) = \gamma(\omega, x)\left(-\omega^2 W_0 e^{j\omega t}\right). \tag{3.87c}$$

**Tip Excitation - EMF**

For the case of EMF tip excitation the forcing functions $f_r(t) = F_r e^{j\omega t}$ is redefined so that

$$F_r = -\sigma_r I_0 \tag{3.88}$$

where

$$\sigma_r = \frac{B_r}{2\pi} C_v \phi_r^{(3)}(L_{eff}). \tag{3.89}$$

The steady state voltage, power and transverse mechanical responses are then

$$\begin{aligned} v(t) &= \alpha(\omega)\left(-I_0 e^{j\omega t}\right), \\ p(t) &= \psi(\omega)\left(-I_0 e^{j\omega t}\right) \\ w_{rel}(t) &= \gamma(\omega, x)\left(-I_0 e^{j\omega t}\right), . \end{aligned}$$

Using the appropriate set of expressions for the corresponding forcing input (base vibration or EMF tip), the following normalized FRF expressions are formed.

**Voltage FRF**

$$\alpha(\omega) = \frac{\sum_{r=1}^{\infty} \frac{-j\omega\tilde{\theta}_r\sigma_r}{\omega_r^2-\omega^2+j2\zeta_r\omega_r\omega}}{\frac{1}{R_L} + j\omega C_{\tilde{p}}^{eff} + \sum_{r=1}^{\infty} \frac{j\omega\tilde{\theta}_r^2}{\omega_r^2-\omega^2+j2\zeta_r\omega_r\omega}}. \tag{3.91}$$

**Power FRF**

$$\psi(\omega) = \frac{1}{R_L}\left(\frac{\sum_{r=1}^{\infty} \frac{-j\omega\tilde{\theta}_r\sigma_r}{\omega_r^2-\omega^2+j2\zeta_r\omega_r\omega}}{\frac{1}{R_L} + j\omega C_{\tilde{p}}^{eff} + \sum_{r=1}^{\infty} \frac{j\omega\tilde{\theta}_r^2}{\omega_r^2-\omega^2+j2\zeta_r\omega_r\omega}}\right)^2. \tag{3.92}$$

**Transverse displacement FRF**

$$\gamma(\omega, x) = \sum_{r=1}^{\infty}\left[\left(\sigma_r - \tilde{\theta}_r\frac{\sum_{r=1}^{\infty} \frac{j\omega\tilde{\theta}_r\sigma_r}{\omega_r^2-\omega^2+j2\zeta_r\omega_r\omega}}{\frac{1}{R_L} + j\omega C_{\tilde{p}}^{eff} + \sum_{r=1}^{\infty} \frac{j\omega\tilde{\theta}_r^2}{\omega_r^2-\omega^2+j2\zeta_r\omega_r\omega}}\right)\frac{\phi_r^{(n)}(x)e^{j\omega t}}{\omega_r^2-\omega^2+j2\zeta_r\omega_r\omega}\right]. \tag{3.93}$$

# Chapter 4

# Experimental Results & Model Validation

## 4.1 Experimental Methodology

As alluded to in the modelling section 3.4.1 of this thesis, the approach to experimentally validate this harvester design is two fold with a final section to test the harvester on a 120 VAC 60 Hz wall signal. Once the harvester has been fabricated, it will be experimentally validated with a base excitation experimental setup using an electrodynamic shaker. The base excitation experimental results are compared to the developed analytical model to provide insight into model accuracy. Base excitation experimental tests will also provide a means of determining maximum power resistance of the harvester as well as conduct any frequency tuning required. Once the harvester is properly tuned to the designed frequency of 60 Hz (within 1 Hz), damping ratios as well as maximum power resistance values are determined using experimental techniques. Once the harvester is completely characterized for base excitation conditions, it is relocated and tested under an EMF tip excitation in the form of a constant current amplitude sine sweep signal. A similar experimental procedure is used for the tip excitation and experimental results are compared over a range of frequencies to the developed analytic model. Finally, the tuned harvester is tested on a real wall signal at various currents using a space heater for a load and compared to the model at the discrete design frequency of 60 Hz.

## 4.2 Harvester Fabrication

### 4.2.1 Harvester Assembly

The complete harvester assembly including clamping mechanism shown in Figure 4.1 has a length, width and height of approximately 60 mm x 50 mm x 25 mm respectively. The clamping mechanism may be attached to either the electrodynamic shaker or the conducting wire testing platform without disrupting the boundary condition or tuned resonant frequency. The electrical leads soldered to each layer of piezoelectric material on the top and bottom of the bimorph cantilever are connected to a resistive load circuit on the breadboard via a short connector cable. The circuit is then connected to a data acquisition center (DAC) for measurement. Figure 4.1 shows the harvester and resistive circuit used for experimental testing. In this thesis, a single prototype harvester is designed, modelled and fabricated, both a 60 Hz resonant frequency. The harvester has been designed with an arbitrary piezoelectric material length of approximately 10 mm which allows the effective lengths to be less than 30 mm which was outlined as a design constraint. The harvester will be identified as EH10 (10 mm PZT). A full table of design and material parameters is provided in section 4.2.4.

### 4.2.2 Beam Fabrication

Substrate material is a high strength 510 Bronze with a thickness of 0.254 mm was provided from the manufacturer in rectangular sheets (approx. 15 cm x 30 cm). The sheets were then cut into 15 cm lengths using a pedal shearing machine found in most machine shops by carefully measuring and scribing 3 mm uniform widths. The variance in width from end to end was found to be negligible. The beams were then cut to 65 mm lengths, which allowed for approximately 25 mm of clamp coverage and 10 mm of overhang on the back side of the clamp. The rear overhang provided a grabbing location which was used during frequency tuning. Lastly, two lines were lightly scribed along the width of the beam 10 mm apart at locations $L_1$ and $L_2$ where the PZT will be epoxied.

Piezoelectric material PZT-5A was provided from the manufacturer in square sheets (approx. 72 mm) with a thickness of 0.127 mm which would require careful cutting. PZT may be cut a number of ways effectively depending on the thickness including water jet, laser, and razor blade. One of the most common techniques is using laser cutting technology since cutting accuracy with lasers tends to be high however setting laser parameters can be time consuming if not previously known. Since the thickness of the PZT material chosen for

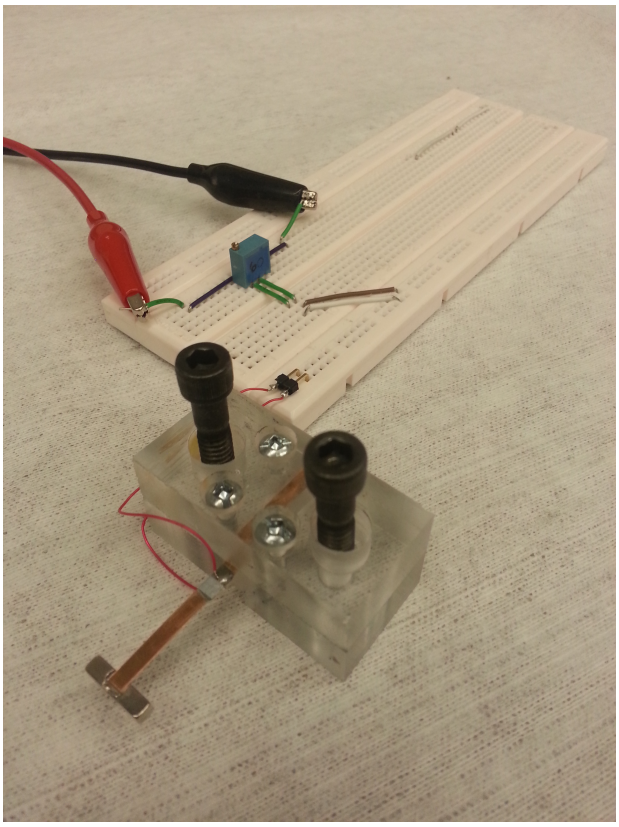

(a) EMF Harvester and Circuit.

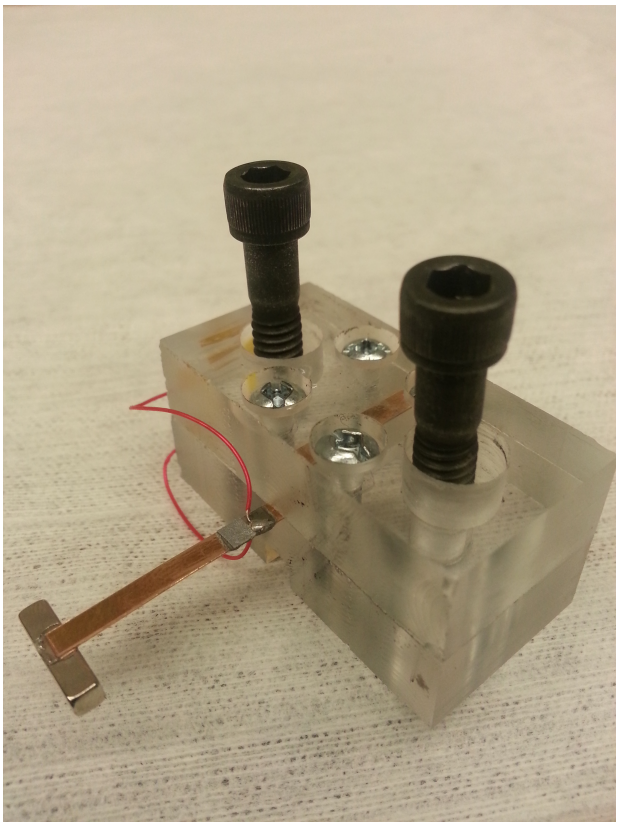

(b) EMF Harvester Assembly

Figure 4.1: EMF Energy Harvester Assembly

prototype fabrication is extremely thin, manufacturer recommendations suggested simple razor blaze scoring to be a reasonably accurate method of cutting. The square PZT sheets were carefully taped to a cutting surface using masking tape and then the previously cut bronze substrate material lengths were used as a rule to score PZT material to the matching width. The PZT lengths were then cut as accurately as possible with a rule to the designed length of 10 mm. Since this process is so delicate, many prototypes had to be made before completing a working prototype fit for testing.

Conductive two part epoxy was then mixed and applied to the area of the beam (substrate) that had been previously scribed. PZT material sections were then carefully located and taped into position with masking tape to prevent shifting during curing. Special care

was taken to mark the PZT sections with their poling direction prior to the epoxy stage since the harvester design is a series configuration. Once cured, the masking tape and all excess epoxy was removed and tested for continuity to ensure substantial leakage was not present across individual PZT sections.

The next step was to epoxy the neodymium magnetic tip mass to the prefabricated beam assembly. First the magnet was weighed using a high precision (0.001±) GemPro-250 scale to determine actual magnet weight. Then the prefabricated beam was measured to determine the beams weight. The magnet was then carefully centered and epoxied to the tip of the beam using general purpose high strength super-glue and weighed a third time to determine any additional mass of the epoxy at the tip of the beam.

The final step in the harvester assembly was to solder two small conducting wire leads to the base of the PZT material (both sides) using manufacturer provided solder flux and lead solder. The leads were soldered to the PZT at the base near the clamping location and taped to the clamping mechanism to reduce any impact the leads may have on the dynamics of the harvester.

### 4.2.3 Interchangeable Clamping Mechanism

The clamping mechanism was constructed from transparent plexiglass material which was sufficiently hard to provide the fixed boundary condition required for testing. This material provided the rigid boundary condition required while eliminating the possibility of electrical leakage since the material is non-conductive. The two piece clamp mechanism was machined to size (2"x 1"x 0.5") with a total of six holes drill into each clamping piece. Four holes for beam clamping and boundary adjustments (tuning) and two holes that would fasten to both the shaker (vibration base excitation) and the conducting wire platform (EMF tip excitation). The bottom clamp piece also has slot cut parallel to where the beams length is located to provide a locating channel for the conducting wire to travel through during EMF wire experimentation.

### 4.2.4 Harvester Parameter Identification

Based on information gathered from Chapter 3 the following tables outline the geometry and material parameters used for analytical modelling. Width and thickness parameters for both the substrate and piezoelectric material were chosen arbitrarily to be as thin as possible to meet the frequency design parameter of 60 Hz.

Table 4.1: EMF Harvester Material Properties

| ***PZT-5A, [74]*** | | | |
|---|---|---|---|
| **Material Parameter Name** | **Name** | **Units** | **Value Used** |
| Relative Dielectric Constant | $\varepsilon_{33}^{S}$ | $nF/m$ | *13.3* |
| | $\varepsilon_{33}^{T}$ | $\varepsilon^{T}/\varepsilon_{0}$ | *1700* |
| Piezoelectric coefficients | $d_{31}$ | $pm/V$ | *-171* |
| | $e_{31}$ | $C/m^2$ | *-5.5* |
| Elastic Modulus | $c_{11}^{E}$ | $N/m^2$ | *61* |
| Elastic Compliance | $s_{11}^{E}$ | $m^2/N$ | *16.4* |
| Density | $\rho_{\tilde{p}}$ | $Kg/m^3$ | *7750* |
| ***Ultra-Strength Bronze (Alloy 510), [73]*** | | | |
| **Material Parameter Name** | **Name** | **Units** | **Value Used** |
| Elastic Modulus | $Y_{\tilde{s}}$ | $N/m^2$ | 110 x $10^9$ |
| Density | $\rho_{\tilde{s}}$ | $Kg/m^3$ | 8800 |
| ***Neodymium Magnet (NdFeb, N42), [65]*** | | | |
| **Material Parameter Name** | **Name** | **Units** | **Value Used** |
| Residual Magnetic Flux Density | $Br$ | Tesla | 1.32 |

Table 4.2: Harvester Geometric Parameters

| **Geometric Parameter Name** | **Name** | **Units** | **EH10** |
|---|---|---|---|
| Substrate Length | $L_{eff}$ | mm | 27.36 |
| PZT Length | $L_{\tilde{p}}$ | mm | 10.75 |
| PZT Gap Length | $L_1$ | mm | 1 |
| PZT End Length | $L_2$ | mm | 11.75 |
| Width | $w$ | mm | 2.86 |
| PZT Thickness | $t_{\tilde{p}}$ | mm | 0.127 |
| Substrate Thickness | $t_{\tilde{s}}$ | mm | 0.254 |
| Magnet Length | $L_m$ | mm | 3.175 |
| Magnet Thickness | $t_m$ | mm | 3.175 |
| Magnet Width | $w_m$ | mm | 12.65 |

## 4.3 Base Vibration Validation

### 4.3.1 Experimental Setup and Equipment

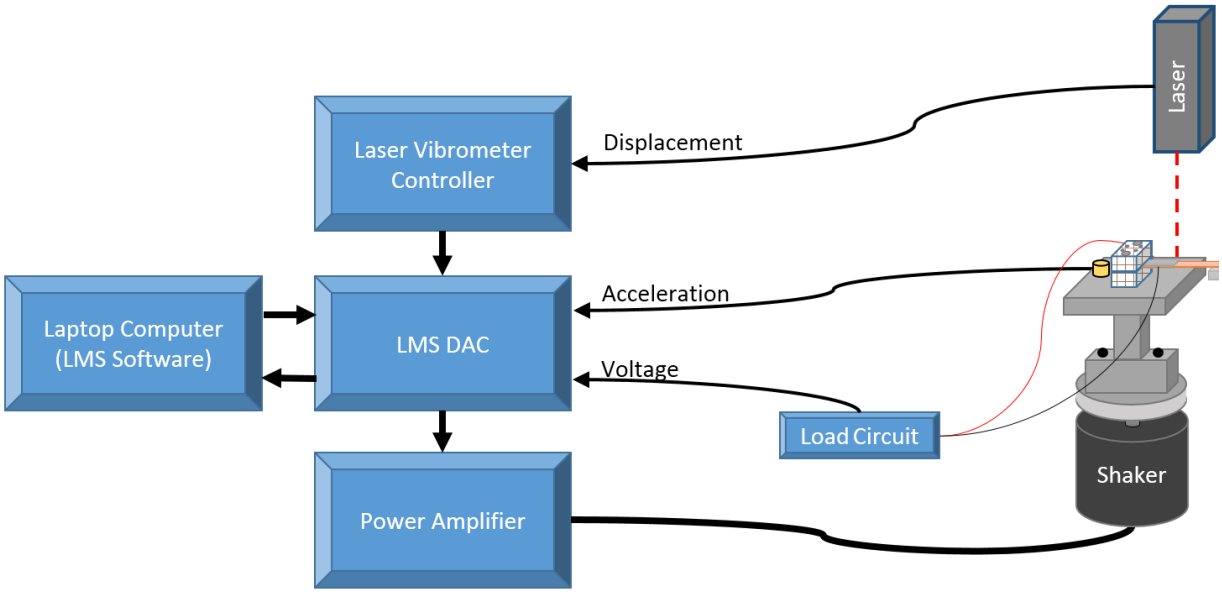


Figure 4.2: Base Vibration Experimental Set-up Diagram.

To validate the fabricated harvester under base excitation an electrodynamic shaker is used to excite the harvester and provide harmonic vibrations. It is a Modal Shop 2075 Dual Purpose shaker that can provide up 334 N of force [75]. The shaker is mounted to the floor using a standard trunnion mounting base that is angled in the vertical position. The armature of the shaker has a 25.4 mm stroke that can be driving at frequencies up to 6500 Hz.

The shaker driven by a Modal Shop Model 2050E09 power amplifier [75] which is controlled by an LMS SCADAS Mobile Data Acquisition System [76]. The system has 8 input ports that can be configured for measurement or control feedback and 2 output ports that can be configured to provide various signals (sine, chirp, burst chirp etc.). The shaker uses an accelerometer mounted on the shaker to provide controlled feedback (reference channel) over a range of frequencies. The accelerometer used is made by PCB Piezotronics [77], model 352A24, which has a sensitivity of 100 mV/g that can operate at frequencies up to 10,000 Hz.

Another component required for measuring displacement of the harvester beam is a laser vibrometer and accompanied controller. The sensor head is a Polytec OFV 505 with a OFV 5000 controlling unit made by Polytec [78]. The vibrometer uses the Doppler principle to measure the displacement of a moving object by directing a laser beam of light at the object and measuring the frequency shift of the returning light. Using the laser vibrometer, displacement can be measured to produce an FRF measurement (displacement/base acceleration). The composites section of the beam was selected as a good measuring location since the displacement is minimal closest to the fixed end of the beam. This allowed for a single measurement to be made from the laser vibrometer without changing settings to increase ranges. The measurement location from the fixed end was 10.25mm where a small piece of reflective tape was used to reflect the laser.

The harvester output voltage signal is measured by connecting BNC crocodile clamps to the circuit shown in Figure 4.1a which is used to produce a second FRF directly (Output Voltage/base acceleration). Power output of the harvester can then be calculated using Eq. (3.92) and the voltage data obtained and the known load resistance $R_L$ to generate a final power FRF (power/base acceleration).

A laptop running the necessary LMS Test Lab software was connected to the LMS hardware system via Ethernet cable to measure and record experimental results in real time as well as control signal output parameters to the shaker. This experimental test set up required the Sine Control LMS software to configure a frequency sine sweep from 10 Hz to 120 Hz over a constant 0.2g acceleration to produce FRFs. A range was chosen for the acceleration input parameter to increase measurement sensitivity. Within the test settings various test parameters can be set including sweep rate and frequency resolution. For this test a sweep rate of 0.1 Hz/s was chosen with a frequency resolution of 0.1 Hz. A breadboard with the resistive circuit required was mounted near the shaker to determine the optimal resistance value for the harvester using a potentiometer. The experimental set-up has been depicted in Figure 4.2 which identifies major components and signal directions.

Based on the fact that the electrodynamic shaker uses electromagnetic forces to create harmonic motion at the shaker armature, considerations must be made to segregate the magnetic fields of the harvester and the shaker. A lab tested aluminum stand off was mounted on the shakers main platform to provide enough offset distance such that the fields produced by the shaker do not interact with the harvester tip mass. The complete set up is depicted in Figure 4.3.

Lastly, a complete analytical model was developed using MATLAB R2012b to preform all mathematical modelling and calculations required for direct data comparison. Acceleration, voltage, displacement and frequency data extracted from the LMS system was

unmodified and processed with MATLAB code to compare experimental and model data sets of interest.

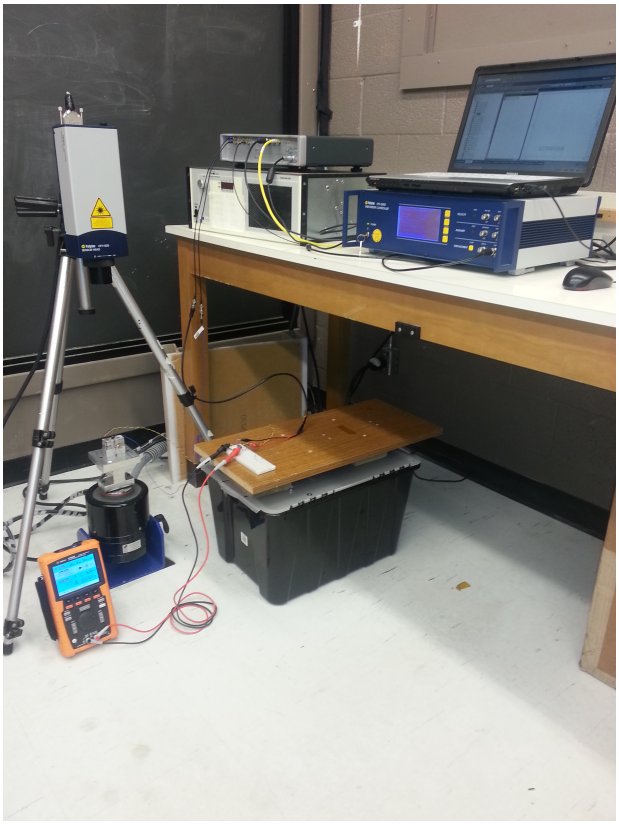

(a) Base Vibration Experimental Set-up.

(b) Harvester and Resistive Load Circuit.

Figure 4.3: Base Vibration Experimental Set-up

### 4.3.2 Resonance Tuning

The harvester was fabricated to the geometric dimensions outlined in Table 4.2. Based on these design parameters, Eq.(3.50) was used to determine the effective length $L_{eff}$ for the bimorph harvester to produce a resonant frequency of 60 Hz . $L_1$ (tuning gap length), $L_{eff}$ and the resonant frequency of the design harvester are compared to the experimental results in Table 4.3 to determine the accuracy of the model under short circuit conditions

($R_L \approx 0$) or practically, $R_L = 428.6$ ohms. The harvester was manually tuned to within 1 Hz of the designed frequency.

Table 4.3: EH10 - Model accuracy and tuning adjustments

| | **EH10** | | |
|---|---|---|---|
| **Adjusted Parameters** | **Designed** | **Before Tuning** | **After Tuning** |
| **Effective Length (mm),** $L_{eff}$ | *27.36* | 27.21 | 27.71 |
| **Gap Length (mm),** $L_1$ | *1* | 1 | 1.5 |
| **Frequency (Hz),** $\omega_1$ | *60* | 62.1 | 59.1 |

The primary goal of this thesis was to develop a model which would accurately predict the fundamental frequency of a discontinuous piezoelectric bimorph cantilever beam. The model demonstrates a satisfactory agreement for this application within 2 Hz of the designed frequency prior to minor tuning adjustments. The small frequency error is attributed to the fact that the model does not account for the stiffness or mass caused by the epoxy used to mount the piezoelectric layers to the substrate. However based on the approach taken here the comparative results demonstrate a high degree of accuracy that is sufficient for the required application.

### 4.3.3 Maximum Power Resistance Characterization

The first step in validating this harvester is to determine the maximum power resistance using the Maximum Power Transfer Theorem. The natural frequency of the system was modelled under short circuit conditions ($R_L \approx 0$). When the systems electromechanical parameters are altered by changing the load resistance, the natural frequency is also altered. The short circuit frequency will always be lower than than the optimal load frequency or open circuit frequency, so it is only natural that the model underestimate the fundamental frequency of the system once the maximum power resistance load is selected. Although analytical models do exist to predict the optimal load resistance for a bimorph harvester [11, 79], mechanical damping is a contributing parameter in these models and must still be determined experimentally. Furthermore, the accuracy of these models has not been proven to a degree of certain accuracy. These issues make it difficult to model the damped harvester frequency at an optimal resistance value. Considering the fact that the harvester was constructed manually and epoxied together using a conductive epoxy which creates additional stiffness and resistance that is unaccounted for in the model, the use of one of

these models would have been ineffective. Since the approach in this thesis was to fabricate the design, a modelling approach to determine the maximum power transfer resistance was ignored. A simplistic approach was used here to match the internal resistance of the harvester with the resistance of the external load. Through circuit analysis of the series circuit represented in Figure 4.4 power at the load can be found

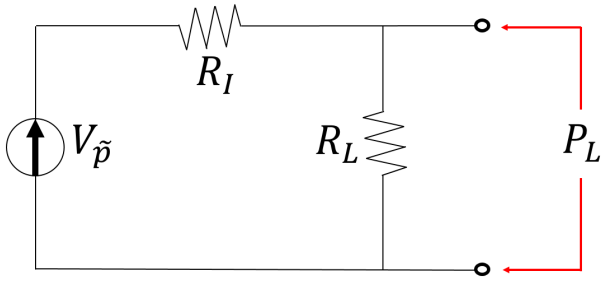


Figure 4.4: Maximum power electrical circuit representation

$$I = \frac{V_{\tilde{p}}}{R_L} = \frac{V_{\tilde{p}}}{R_I + R_L} \tag{4.1a}$$

$$P_L = I^2 R_L = \frac{V_{\tilde{p}}^2}{R_I^2 + 2R_I R_L + R_L^2} R_L \tag{4.1b}$$

$$P_L = \frac{V_{\tilde{p}}^2}{\frac{R_I^2}{R_L} + 2R_I + R_L} \tag{4.1c}$$

$P_L$ and $R_L$ represents power at the load and resistance of the load respectively and $R_I$ is the internal resistance of the harvester. To maximize the power at the load $P_L$ the denominator of Eq.(4.1) must be as small as possible. Taking the derivative of the denominator and equating it to zero gives

$$\frac{\mathrm{d}}{\mathrm{d}R_L}\left(\frac{R_I^2}{R_L} + 2R_I + R_L\right) = 0 \tag{4.2a}$$

$$\frac{-R_I^2}{R_L} + 0 + 1 = 0 \tag{4.2b}$$

$$R_I = R_L \tag{4.2c}$$

A simple experimental method commonly used for determining the maximum power resistance for piezoelectric harvesting units is to increase the load resistance incrementally

using a potentiometer across the harvester leads while sweeping through frequencies at the constant acceleration input level (chirp signal). While doing this, voltage is measured across the load to calculate the corresponding output power. The results have also been plotted in Figure 4.5.

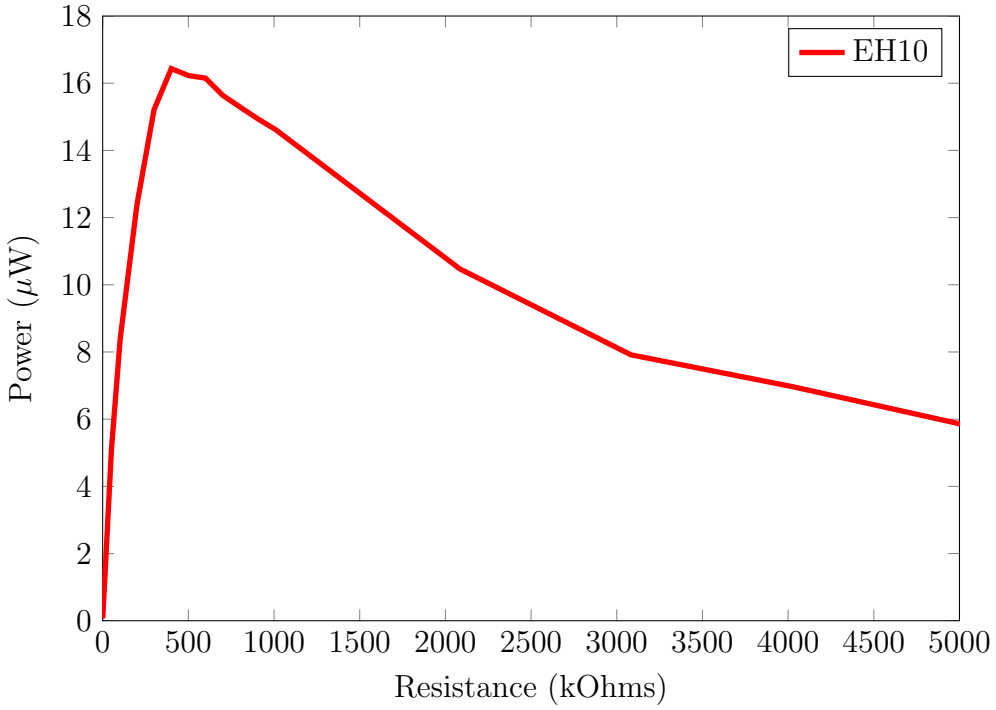


Figure 4.5: Maximum power resistance

Table 4.4: Max Power Resistance at Constant Acceleration (0.1g)

| **Harvester** | **Max Power Resistance (kOhms)** | **Power Output ($\mu$W)** | $\omega_1$ **(Hz)** |
|---|---|---|---|
| **EH10** | 548 | 16.435 | 59.5 |

### 4.3.4 Damping Characterization

The strain-rate $C_s$ and viscous air $C_a$ damping coefficients considered in the PDE of Eq.(3.21) have not been identified. Modal damping $\zeta_r$ is considered here instead since

the individual identification of these coefficients is not necessary for this thesis however the reader can refer to [11] to identify these coefficients explicitly. Since maximum power is the major goal in energy harvesting, determining the optimal resistive load is most important. In this thesis the optimal resistive load was determined experimentally which resulted in an undamped model frequencies slightly above 60 Hz. A note of comparison to be considered in this thesis is the peak values found in the FRF data. Since resonance is phenomenon that produces infinite amplitude which is only reduced by inherent damping in the system, it is difficult to obtain matching values at the peak unless physical damping is perfectly accounted for. Typically in energy harvesting applications the areas just outside the resonance location are more of interest when comparing experimental results to an analytical model since most harvesting applications have an input frequency which drifts. Characterization of the modal mechanical damping ratio is an important step for accurate electromechanical modelling of the harvester. Two approaches were considered and compared in this thesis, an experimental method commonly known as 'Half-power bandwidth method' (HPB) and a closed-form expression (CFE) developed by [11] which has been used to accurately predict modal damping for an arbitrary load resistance using non-dimensional parameters.

### Half-power Bandwidth Method

The Half-power bandwidth method which is a common technique to experimentally determine modal damping ratios $\zeta_r$. Since the harvester is assumed to be a linear electromechanical system, the modal damping ratios can be obtained from, and applied to, FRF data from the transverse displacement FRF amplitudes. A short-circuit resistance value was used for modal damping ratio extraction since piezolectric coupling contributes to the mechanical damping ratio [11]. Using the sample FRF data shown in Figure 4.6, points of interest have been identified to characterize the modal damping ratios as

$$|H(\omega_a)| = |H(\omega_b)| = \frac{|H(\omega_d)|}{\sqrt{2}}, \tag{4.3a}$$

$$\omega_b - \omega_a = 2\zeta\omega_d, \tag{4.3b}$$

$$\zeta_r = \frac{\omega_b - \omega_a}{2\omega_d}. \tag{4.3c}$$

$\omega_d$ is the experimentally damped natural frequency of interest, $\omega_a$ and $\omega_b$ the corresponding frequency values found at a 3dB drop with $|H(\omega_a)|$ and $|H(\omega_b)|$ amplitudes. Since the load resistance affects the mechanical behavior of the system, the modal damping ratios are

found using short circuit conditions ($R_L \approx 0$) which in reality $R_L$ was measured as 428.6 ohms.

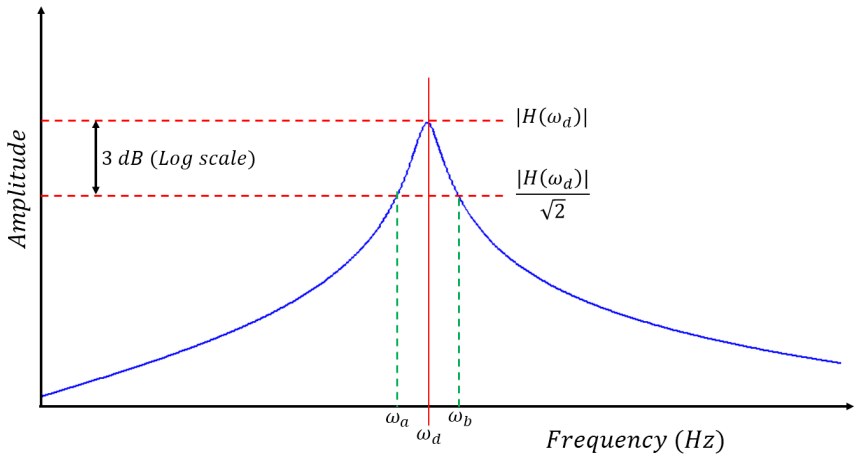


Figure 4.6: Half Power FRF Bandwidth Damping Characterization

### Closed-form Damping Expression

The closed-form expression developed by [11] to identify mechanical damping for an arbitrary load resistance is outlined here. The resistance used for this thesis will be the experimentally determined maximum power resistance. Although modal damping ratios can theoretically be obtained from either the voltage FRF or the displacement FRF (assuming linear electromechanical coupling), the voltage FRF extraction has be chosen here for simplicity. The following dimensionless variables are used to simplify the magnitude of the voltage FRF.

$$\nu_r = R_L C_{\tilde{p}}^{eff} \omega_r, \tag{4.4a}$$

$$\gamma_r = \frac{\tilde{\theta}_r^2}{C_{\tilde{p}}^{eff} \omega_r}, \tag{4.4b}$$

$$\tilde{\omega} = \frac{\omega}{\omega_r} \tag{4.4c}$$

where $\nu_r$ is the dimensionless resistance, $\gamma_r$ is the dimensionless electromechanical coupling factor and $\tilde{\omega}$ is the dimensionless excitation frequency. For an arbitrary resistance $\nu_r$ at

resonance $\tilde{\omega} = 1$, Eq. (3.91) in single-mode form can be expressed as

$$|\alpha(1)| = \frac{\gamma_r \nu_r |\sigma_r / \tilde{\theta}_r|}{\left[ (2\nu_r \zeta_r)^2 + (2\zeta_r + \nu_r \gamma_r)^2 \right]^{1/2}} \tag{4.5}$$

where $|\alpha(1)|$ is a known experimental measurement data used for modal damping identification. Eq. (4.5) will yield a quadratic relation

$$A\zeta_r^2 + B\zeta_r + C = 0 \tag{4.6}$$

such that

$$A = 4(1 + \nu_r^2), \tag{4.7a}$$

$$B = 4\gamma_r \nu_r, \tag{4.7b}$$

$$C = \nu_r^2 \gamma_r^2 - \left( \frac{\gamma_r \nu_r \sigma_r}{|\alpha(1)| \, \tilde{\theta}_r} \right)^2, \tag{4.7c}$$

to yield a positive root which expresses the modal mechanical damping ratio as

$$\zeta_r = \frac{(B^2 - 4AC)^{1/2} - B}{2A}. \tag{4.8}$$

Using these methods, the following table comprises the modal damping ratios calculated from the Voltage FRF experimental data for the prototype harvester which demonstrates substantially higher damping ratios are calculated from the closed-form expression.

Table 4.5: Modal Damping Ratios - Base Vibration

| **Harvester Prototype** | **Half Power Method** | **Closed-form Expression** |
|---|---|---|
| **EH10** | 0.00521 | 0.00857 |

### 4.3.5 Base Vibration Frequency Response Functions

The following FRF data plots shown in Figure 4.7 compare the experimental results with model data. Both HPB and CFE damping methods previously discussed were used to demonstrate each methods effectiveness in modeling the peak values of the FRF data sets.

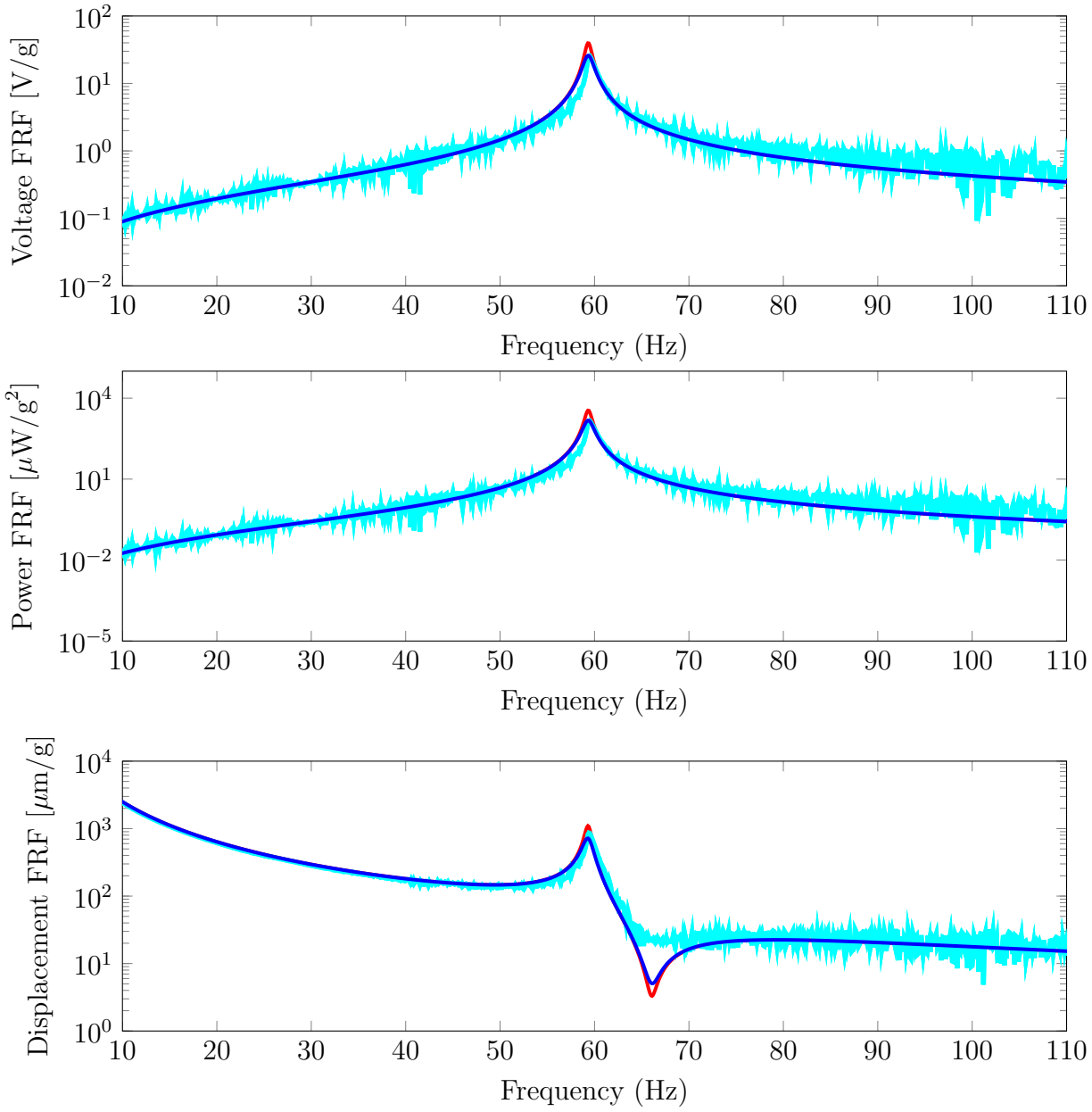


Figure 4.7: Vibration FRFs for 10mm Energy Harvester (EH10). Experiment (**Cyan**) Vs. Model - Half Power Damping (**Red**) and Model - Closed-form Damping (**Blue**)

The peak values and frequencies are compared in Tables 4.6 to provide a better understanding of model accuracy using the different damping methods.

Table 4.6: Damping Effects on Model Accuracy of EH10 - Base Vibration

| | **EH10 - Peak Values at Resonance** | | | |
|---|---|---|---|---|
| **Data Set** | **Frequency (Hz)** | **Voltage FRF (V/g)** | **Power FRF ($\mu W/g^2$)** | **Displacement FRF ($\mu/m$)** |
| **Experimental** | 59.5 | 25.62 | 1197 | 864.9 |
| **Model - Half Power Damping Method** | 59.3 | 39.58 | 3497 | 1098 |
| **Model - Closed-form Damping Method** | 59.3 | 25.85 | 1219 | 718.6 |

When examining the experimental results, it is evident that the model has overestimated the voltage response across all frequencies examined. Considering the fact that the effect of the epoxy was not accounted for in this model, the model and experimental results are quite agreeable. Fabrication techniques with respect to cutting and epoxying the beams may have also diminished the electromechanical coupling of the harvester which resulted in model overestimation. Over all the half-power bandwidth method greatly overestimated the damping values for the voltage FRF which are of most interest but more accurately predicted the mechanical response of the system. The closed-form expression on the other hand was most accurate in predicting both the mechanical and electrical FRF responses however the CFE model underestimated the displacement FRF experimental results. The percentage error between the voltage FRF and the displacement FRF are quite different. Linear piezoelectric piezoelectric modelling assumptions suggest the error in the voltage FRF and displacement FRF to be the same. The differences suggest there is some electromechanical non-linearity present in the system that are unaccounted for which could have been caused during beam fabrication. Lastly, an important note regarding the increased displacement FRF amplitudes at the lower frequencies is that the data extracted from the LMS system is the total displacement amplitude. Larger amplitudes are created at lower frequencies during base excitation experimentation to maintain the constant force throughout the sweep.

## 4.4 Wire Validation - Controlled Signal

### 4.4.1 Experimental Setup and Equipment

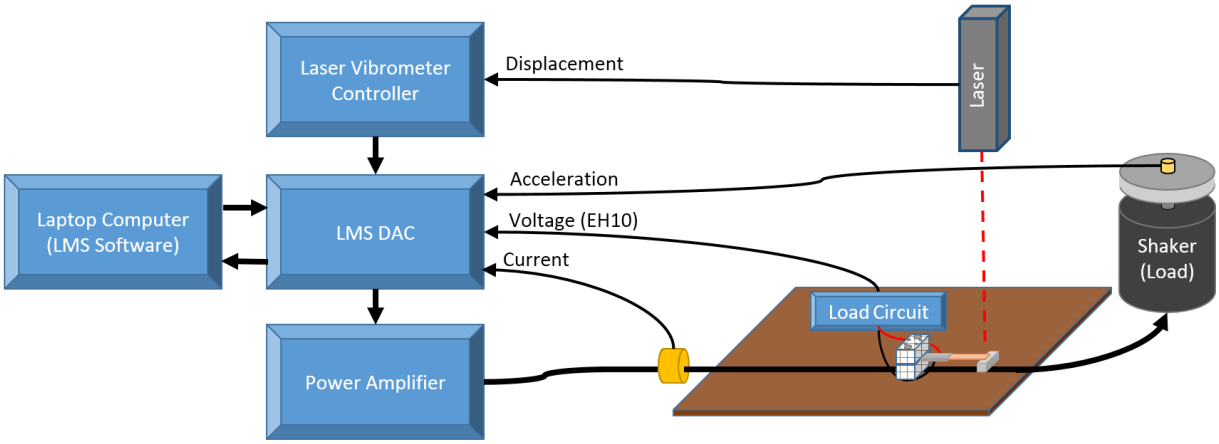


Figure 4.8: Controlled Wire current Experimental Set-up Diagram.

To validate the harvester behavior under tip excitation due to EMF from a current carrying conductor, a controlled test set up was constructed and depicted in Figure 4.11 which identifies major components and signal directions. A custom cable was constructed to connect the amplifier (same as shaker test) to the electrodynamic shaker (used as a load) while segregating a single 10 AWG copper conductor with an outer diameter (including jacket) of 4.12 mm for harvester mounting. The segregated conductor was then mounted along a 1" thick piece of wood with strong kapton tape. The harvester was then fastened to the mounting board (pre-drilled holes in the board), over top of the conducting wire (located in clamp channel) with the same hardware used to fasten the harvester to the shaker test set-up. The clamping mechanism of the harvester was not altered in any way from the shaker tests. The distance from the magnet to the conducting wire was then manually measured for each harvester to be used in force modelling equation Eq.(3.74). A distance of 6 mm was used for EH10 as the offset distance from the center of the wire to the bottom of the magnet. Once completely mounted on the mounting board, the laser vibrometer (same as shaker test) was positioned over top of the harvester to measure beam displacement in the same manner as the shaker test as shown in Figure 4.9.

The shaker used in the base validation test was used in the wire testing as a convenient load that could be controlled the same way it was in the base validation test with the same

accuracy. However, instead of using an accelerometer to provide feedback to the LMS controller, a Fluke i400s AC current clamp was then clamped around the conducting wire to provide the necessary reference feedback (reference channel). This way the required FRF data could be measured in a similar fashion as done with the accelerometer for the base validation tests. The current clamp has two range options, 40 Amp and 400 Amp with corresponding sensitivities of 10 mV/A and 1 mv/A. For the work done in this thesis, the 40 Amp range at 1 mv/A output sensitivity was all that is required.

The harvester output voltage (Output Voltage/Wire-Current), power (Output Power/ Wire-Current) and displacement (Displacement/Wire-Current) FRFs are all measured and calculated in the same manner as the base validation test. The FRF data produced however is normalized to the current running though the wire and not the acceleration in the shaker. A bread board is mounted near the harvester with the maximum power resistance circuit found from base validation testing.

A laptop running the necessary LMS Test Lab software was connected to the LMS hardware system to measure and record experimental results in real time as well as control signal output parameters. This experimental test set up required the Sine Control LMS software to configure a frequency sine sweep from 20 Hz to 120 Hz at a constant current of 1.5 Amps to produce FRFs. Within the test settings various test parameters can be set including sweep rate and frequency resolution. For this test a sweep rate of 0.1 Hz/s was chosen with a frequency resolution of 0.1 Hz. The experimental set-up is shown in Figure 4.9.

Finally, MATLAB was used once again to model the electromechanical behavior of the harvester when subjected to the magnetic forces caused by the current carrying wire. Voltage, displacement and wire current data were all extracted from the LMS data acquisition system and processed using MATLAB without alteration.

### 4.4.2 Damping Characterization

The damping effect of the EMF on the magnet is unknown and characterization of any magnetic damping present in the system is outside the scope of this thesis. Modal damping ratio characterization is however done once again to determine damping ratios in a similar manner in Table 4.7. It is also worth while to compare the experimental damping present in the base vibration experiment set-up to the damping present in the wire current experimental set-up which is done in Table 4.8. The damping ratio found using HPB damping slightly decreased as the harvester was moved from the base vibration set-up to the EMF wire test set-up. The damping found using the CFE however remained relatively constant.

Table 4.7: Modal Damping Ratios - EMF Tip Excitation

| **Harvester Prototype** | **Half Power Method** | **Closed-form Expression** |
|---|---|---|
| **EH10** | 0.00366 | 0.00881 |

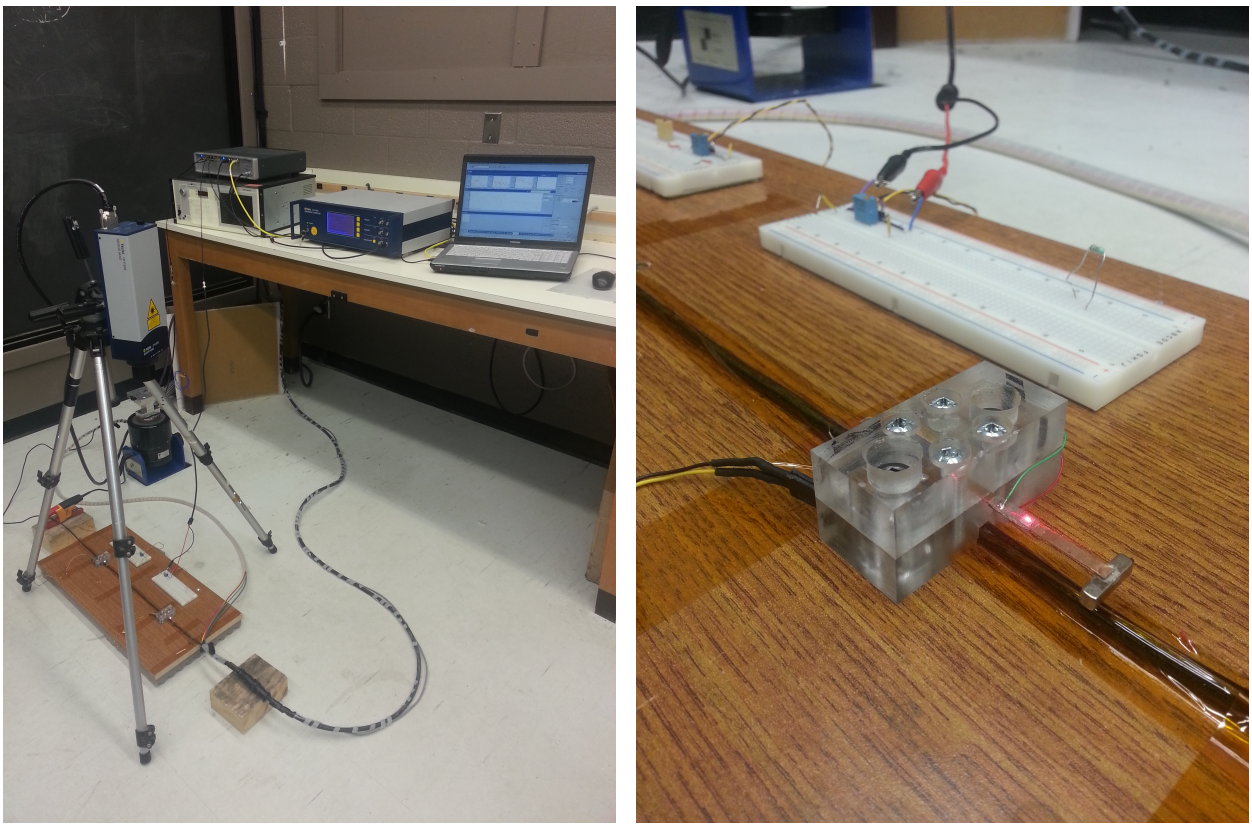

(a) Wire Validation Experimental Set-up. (b) Harvester and Resistive Load Circuit.

Figure 4.9: Controlled Wire current Experimental Set-up

Table 4.8: Comparison of damping values found from both experimental set-ups.

| | **Half Power Bandwidth Method** | | **Closed-form Expression** | |
|---|---|---|---|---|
| **Harvester Prototype** | **Base Vibration $\zeta_1$** | **EMF Tip Excitation $\zeta_1$** | **Base Vibration $\zeta_1$** | **EMF Tip Excitation $\zeta_1$** |
| **EH10** | 0.00521 | 0.00366 | 0.00857 | 0.00881 |

### 4.4.3 Wire Current Frequency Response Functions

The following FRF data plots shown in Figure 4.10 compare the experimental results with model data. Both HPB and CFE damping methods previously discussed were used to demonstrate each methods effectiveness in modelling the peak values of the FRF data sets.

The peak values and frequencies are compared in Table 4.9 to determine the most accurate damping method. With respect to frequency matching, the experimental results showed a natural frequency of 60.1 Hz which is 0.6 Hz higher than the base excitation test. In the case of the EMF tip excitation from a current carrying wire, the Half-power bandwidth method overestimated the experimental results again while the CFE damping method underestimated the estimated all experimental results. The CFE showed marginally more accurate results for the voltage and power FRF however the HPB method was more accurate in predicting the displacement results. This is interesting considering the closed-form expression was most accurate for all the base vibration results. This may suggest non-linearity of the electromechanical response since the HPB damping ratio was extracted from the displacement FRF. This demonstrates the necessity for accurate modal damping determination under various test set-ups and the effect of non-linearity caused by fabrication. Another interesting change from the base vibration set up to the EMF tip excitation is the presence of what appears to be a small torsional mode effects between 30 - 40 Hz of displacement FRF results. This is most likely due to uneven forces (uncentered mounting) applied to the magnetic tip such that the conductor is not properly aligned beneath the center of the magnet. Lastly, the experimental results demonstrate an upward frequency shift of 0.6 Hz. This could simply be caused by an imperfect clamping mechanism.

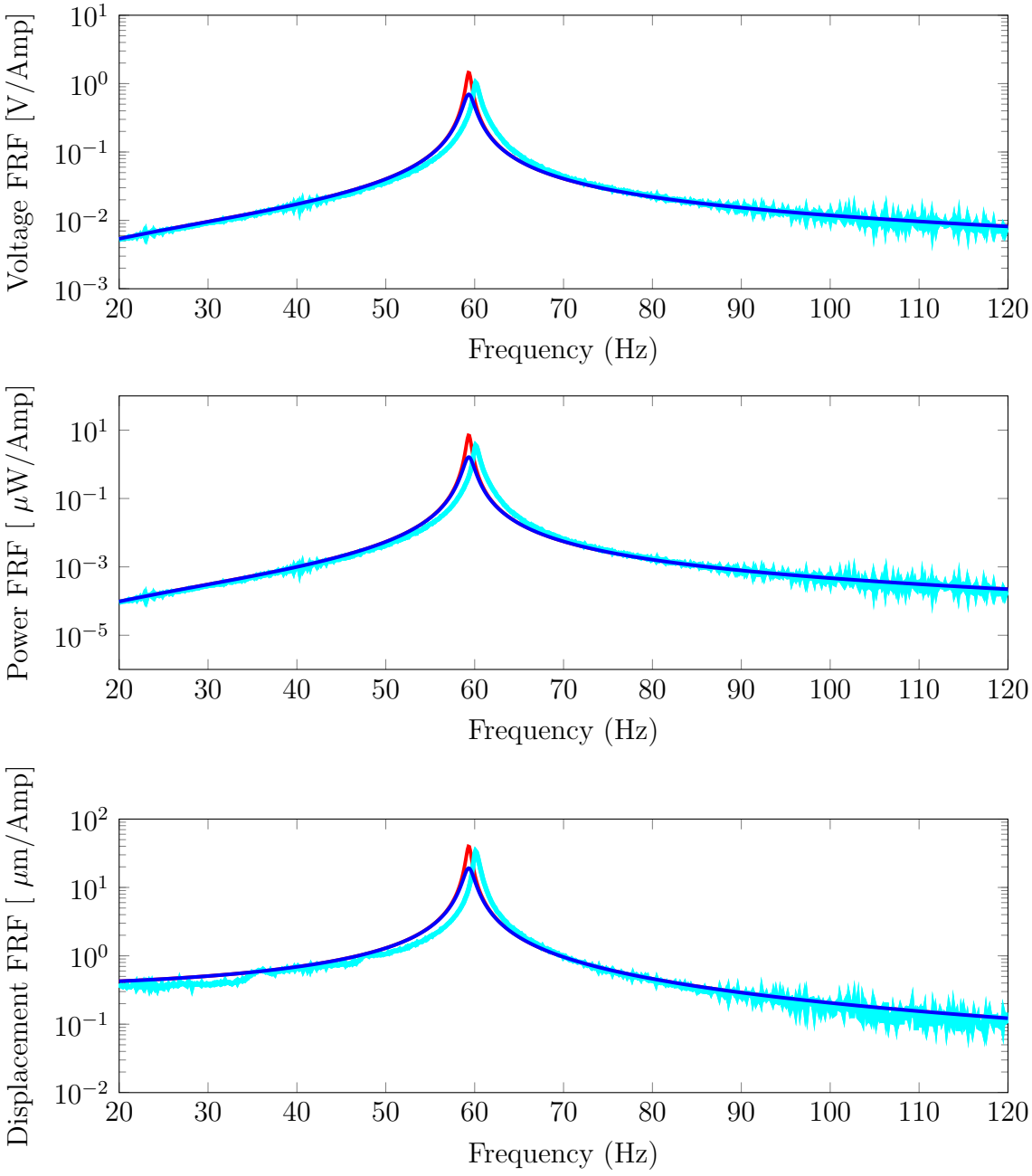


Figure 4.10: Wire Current EMF FRFs for 10mm Energy Harvester (EH10). Experiment (**Cyan**) Vs. Model - Half Power Damping (**Red**) and Model - Closed-form Damping (**Blue**)

Table 4.9: Damping Effects on Model Accuracy of EH10 - Wire Current EMF

| Data Set | EH10 - Peak Values at Resonance | | | |
|---|---|---|---|---|
| | **Frequency (Hz)** | **Voltage FRF** $(V/A)$ | **Power FRF** $(\mu W/A)$ | **Displacement FRF** $(\mu m/A)$ |
| **Experimental** | 60.1 | 1.033 | 3.577 | 33.78 |
| **Model - Half Power Damping Method** | 59.3 | 1.448 | 7.014 | 39.8 |
| **Model - Closed-form Damping Method** | 59.3 | 0.6952 | 1.616 | 19.11 |

## 4.5 Wall Current Validation

### 4.5.1 Experimental Setup and Equipment

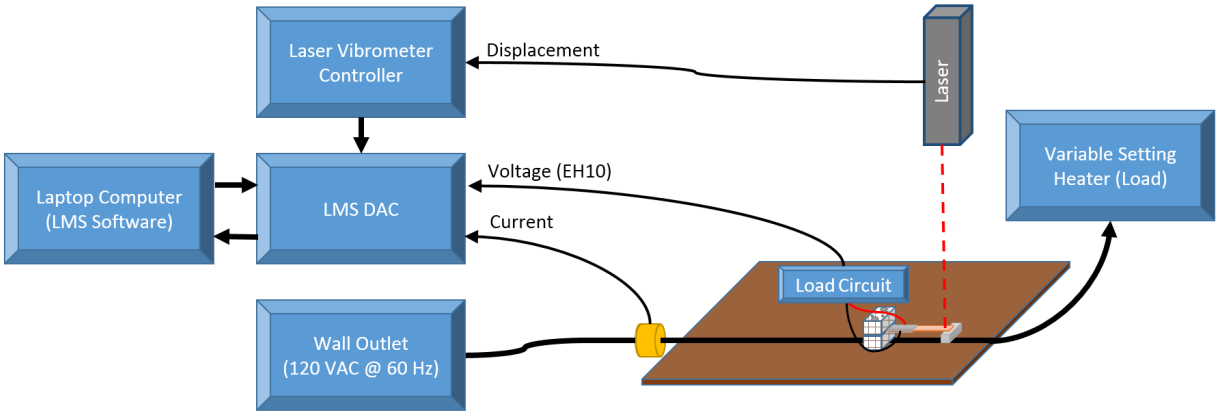


Figure 4.11: Wall current Experimental Set-up Diagram.

The last stage of validations is to test the harvester on a load that is not controlled by complex control hardware such as LMS. For this stage of the testing, the conducting wire and entire test set up remains unaltered, however the conducting wire is supplied from the laboratory wall outlet rather then the amplifier. The wall outlet signal is a common North American signal operating at 120VAC with a primary harmonic at 60 Hz which would be extremely similar to the signal found in the power transmission lines for this

harvester application. The load in this test set up is a 2000 Watt space heater with three load settings (approx. 0.28A, 8.4A, and 16.5A).

The experimental set-up has been depicted in Figure 4.11 which identifies major components and signal directions. Since the supply voltage single is coming from a standard 120 VAC wall outlet with a primary frequency of 60 Hz, it is subject to noise created by loads which back-feed into the buildings immediate power network. This creates a large variance in the current signal which is obviously much greater than the signal generated by the LMS control software. The variance in the current signal however is present mostly within frequencies away from the primary harmonic of 60 Hz. The variance at 60 Hz is extremely minimal which provides a reliable current amplitude. This can be seen by taking measurements of the wall signal over a range of frequencies using a current clamp. Despite taking multiple averages, the variance in the line current outside of 60 Hz is unpredictable. This can been seen in Figure 4.12 and 4.13 where 15 measurements with 25 averages each were taken consecutively and plotted on top of one another for an arbitrary load (heater).

Based on the variance found in the line signal outside the primary driving frequency and the amplitude in comparison to the driving frequency, it would only be valuable to analyze the harvester response at 60 Hz. The main goal is to measure and predict the harvester performance at 60 Hz where a reliable current measurement can be found. For these reasons, the analytical model will be evaluated at a discrete frequency of 60 Hz rather than over a range as done in the previous sections and compared to experimental results.

The measurement system consists of the same hardware used in the wire validation section including the current clamp, laser vibrometer and voltage leads, however in this case there is no control feedback to control the current to the load. The LMS software package used was Spectral Control which allowed for real time monitoring of the current clamp and harvester outputs. The resolution used was 0.125 Hz over a bandwidth range of 128 Hz which has a data capture speed of 8 seconds. A total of 25 averages were taken measuring the input current amplitude at 60 Hz as well as the harvester displacement and voltage output responses for model comparison at 3 separate load values (approx. 0.28A, 8.4A, and 16.5A). The experimental set up is shown in Figure 4.14.

### 4.5.2 Wall Current Harvesting Results

As shown in Figure 4.15, the experimental voltage and power output from EH10 agree with the model trend which should be linear which was also determined in [62]. The Half-power bandwidth (HPB) and Closed-form expression (CFE) damping values have been identified and compared in Figure 4.15 and 4.16 against experimental data for three current inputs

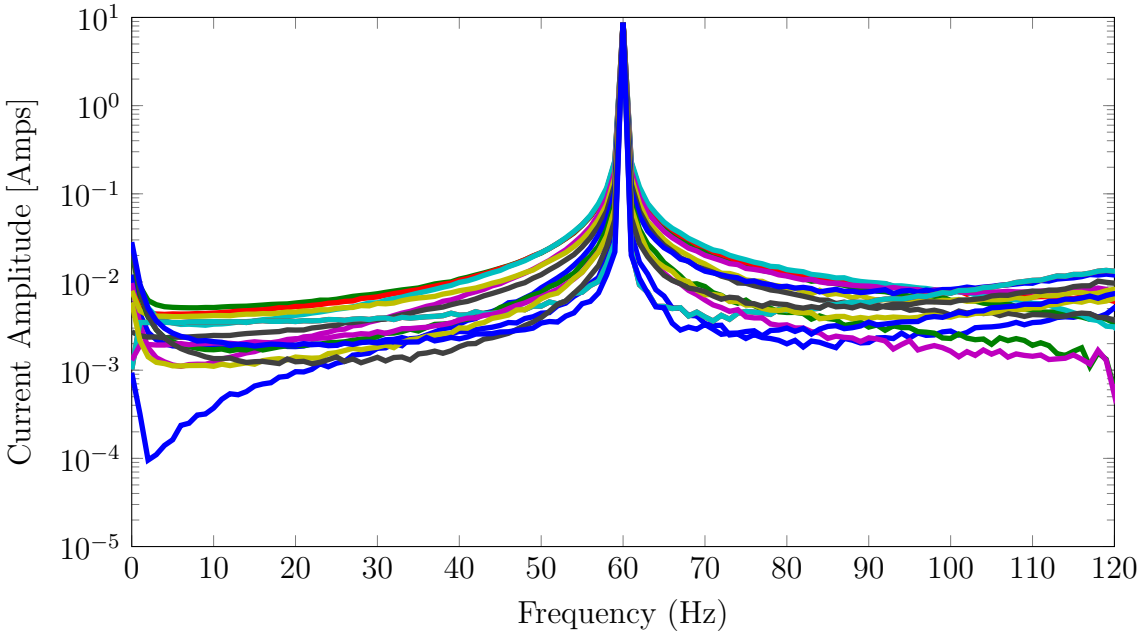


Figure 4.12: 15 measurements of the wall current signal from 0 - 120 Hz

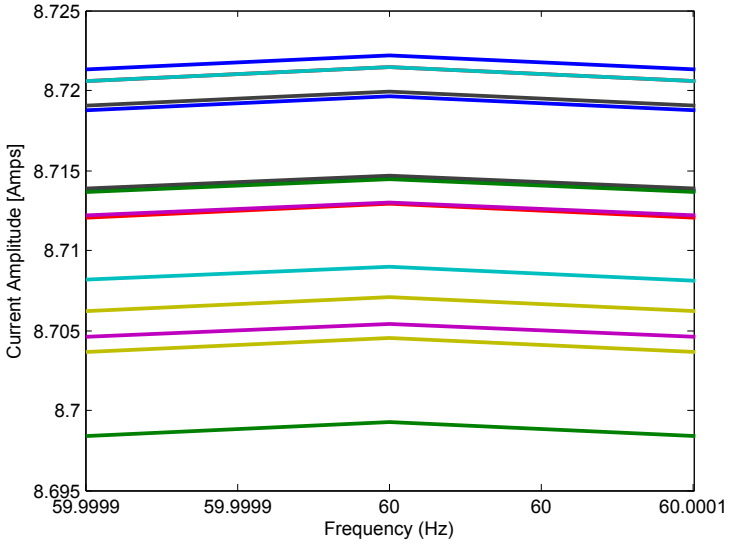


Figure 4.13: 15 measurements of the wire current signal at 60 Hz

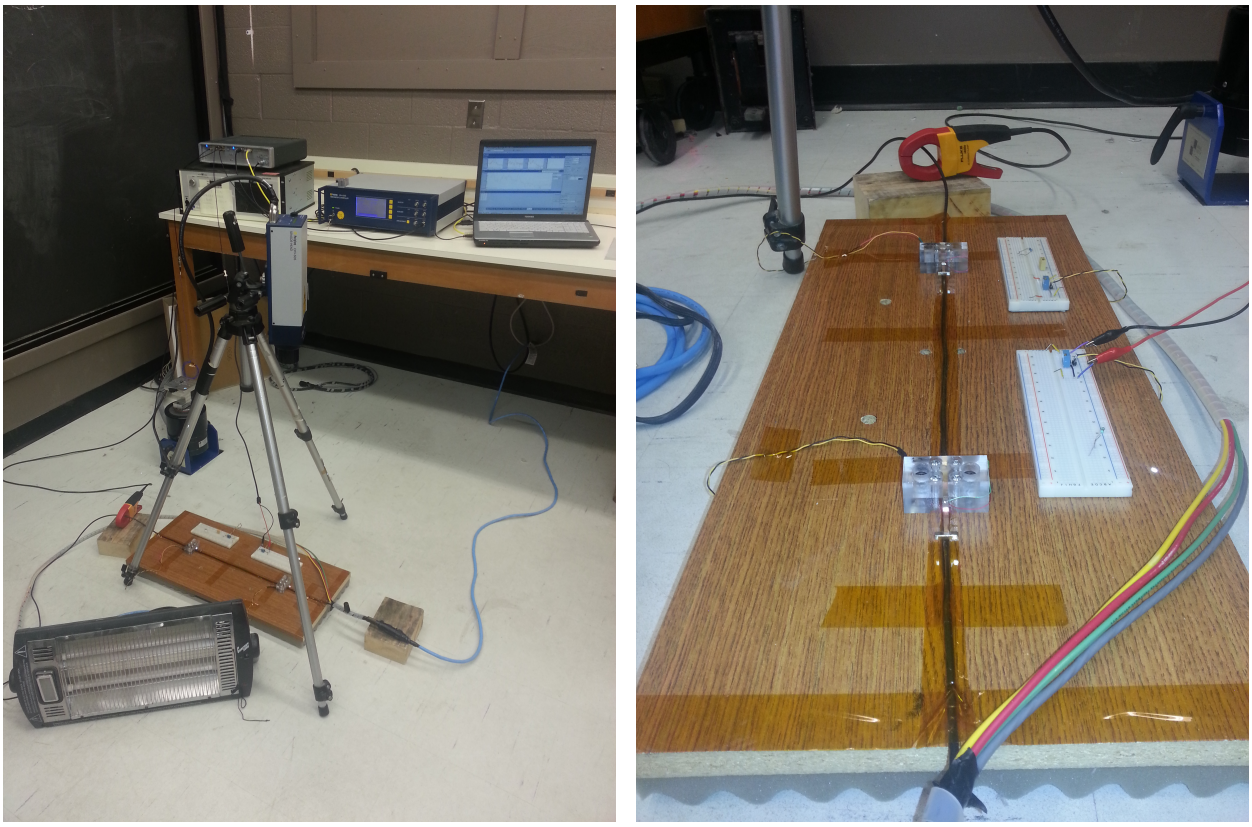

(a) Wall Current Experimental Set-up. (b) Harvester and Resistive Load Circuits.

Figure 4.14: Wall Current Experimental Set-up

produced by changing the heating load settings. The model results that correspond to EH10 show good agreement and linear trends for all compared results.

Since the model and design chosen was to be versatile with respect to power output but yet specific for a designed frequency of 60 Hz, comparing performance of EH10 to other harvesters is difficult. Furthermore, comparison becomes even more ambiguous considering the fact that power output is directly affected based on how close the harvester is mounted to a conducting wire. Since a distance of approximately 6mm was used as the mounting distance, comparison to other harvesters found in literature with different mounting distances would be inconclusive. Piezoelectric material lengths were also chosen arbitrarily to validate the accuracy of the analytical model and as such do not provide a maximum

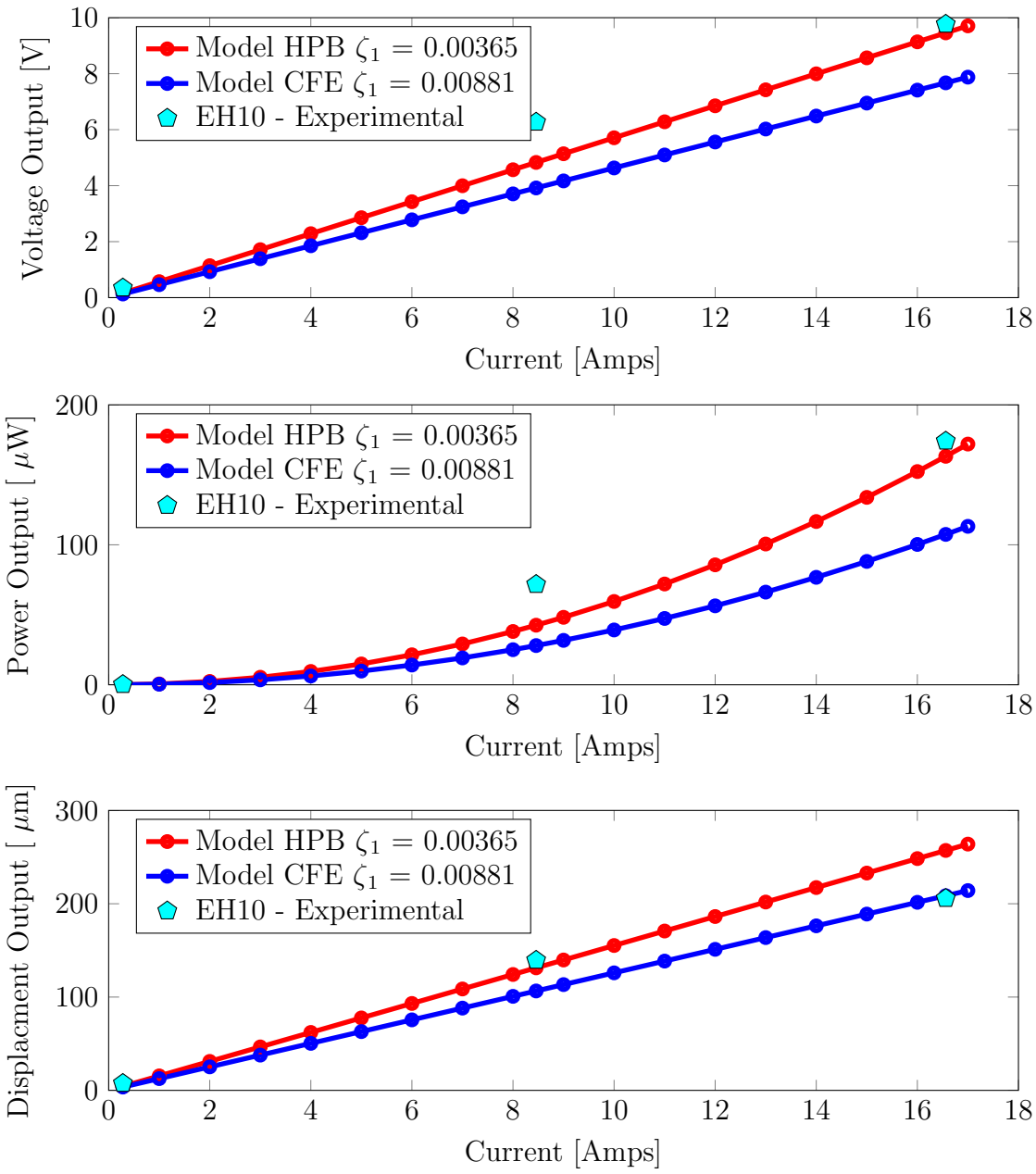


Figure 4.15: EH10 - Voltage power and displacement outputs Vs. Wall current signal (using heater as load)

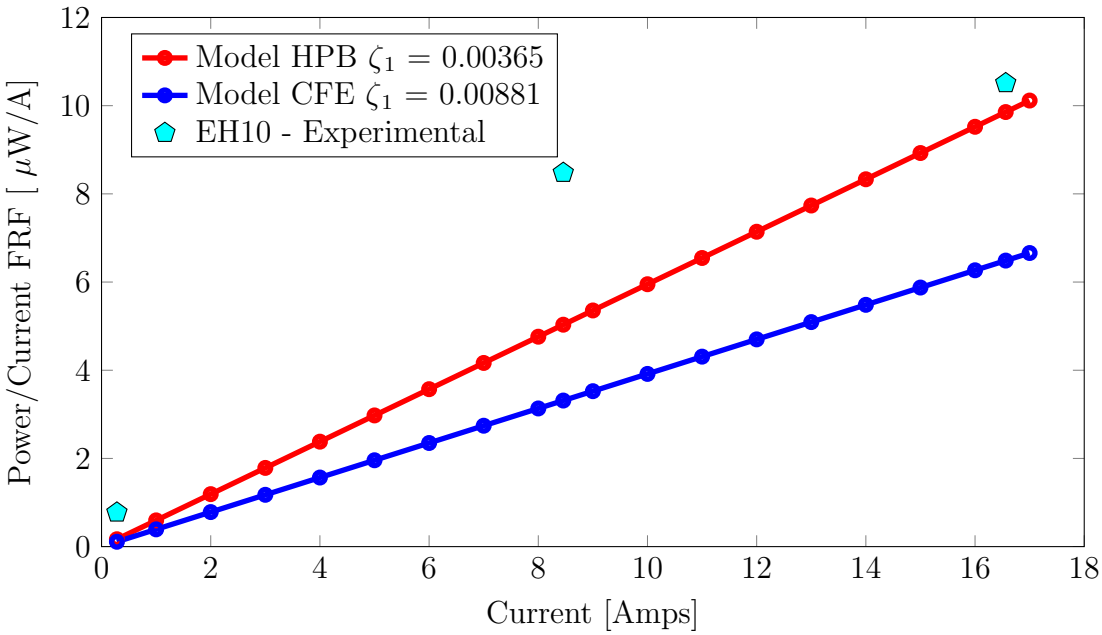


Figure 4.16: EH10 - Power per unit at various currents (using heater as load)

theoretical output for this application. Power density however can still be calucalted for the tested harvester. The calculated over-hang volume excluding the clamping mechanism used to test harvester EH10 is $154 \times 10^{-12} cm^3$. Another metric that could be used to quantify the harvester performance is to determine the power recovered from the grid by the harvester. This can be done with a simple calculation where *Power Recovery=(Power from harvester)/(Power from the wire)* to determine the power recovery ratio. Considering metrics such as power density and power recovery as means of quantifying the harvester prototype, Table 4.10 outlines the harvester performance.

Table 4.10: Experimental Power density and Power Recovery

| | **EH10** | | |
|---|---|---|---|
| **Wall Current, Amplitude (Amps)** | **Power,** $(\mu W)$ | **Power Density,** $\frac{\mu W}{cm^3}$ | **Power Recovery,** (%) |
| **0.28** | 0.22 | 0.0014 | $0.65 \times 10^{-6}$ |
| **8.42** | 71.71 | 0.4635 | $7.09 \times 10^{-6}$ |
| **16.56** | 174.12 | 1.1253 | $8.76 \times 10^{-6}$ |

On a final note of observation based on the results found from the prototype harvester assembled and tested in this thesis, we saw an appreciable power output from EH10 at 174.12 $\mu W$ for a 16.56 amp current. However if the piezoelectric material were increased or decreased we could expect an increased and decrease in power output respectively. An increase in piezoelectric material offers increased capacitance and electromechanical coupling. However, increased piezoelectric material along the beam also results in increased stiffness to the whole system as the beam section with piezoelectric material increases. One of the goals of this thesis was to offer some intuition as to how much piezoelectric material would be required to support various electronic loads. If we make a few assumptions such as constant HPB damping (experimentally found damping ratio) $\zeta_1 = 0.00366$, current amplitude (input force) of 15 amps and a 60 Hz design frequency for the application. The amount of PZT along the beam $L_2$ and the effective length of the beam $L_{eff}$ can simultaneously be increased to the design limit of $L_{eff} \approx 30$ mm while maintaining a 60 Hz resonant frequency to obtain a number of different combinations of beam sizes. Plotting the theoretical power output for these beam sizes gives some future design intuition as to how the power will increase as function of the amount of PZT on the beam for a specific driving frequency. Figure 4.17 demonstrates this concept using the analytical model developed in the thesis. Notice there exist two x-axis labels and values (Effective length and Length of PZT) which correspond to one another to produce theoretical power output (left y-axis) and power per unit current (right y-axis) for each combination of lengths. This simulation was produced by considering 15 amps of current traveling through the conducting wire at a frequency of 60 Hz however similar results are expected for higher currents if the harvester is scaled appropriately.

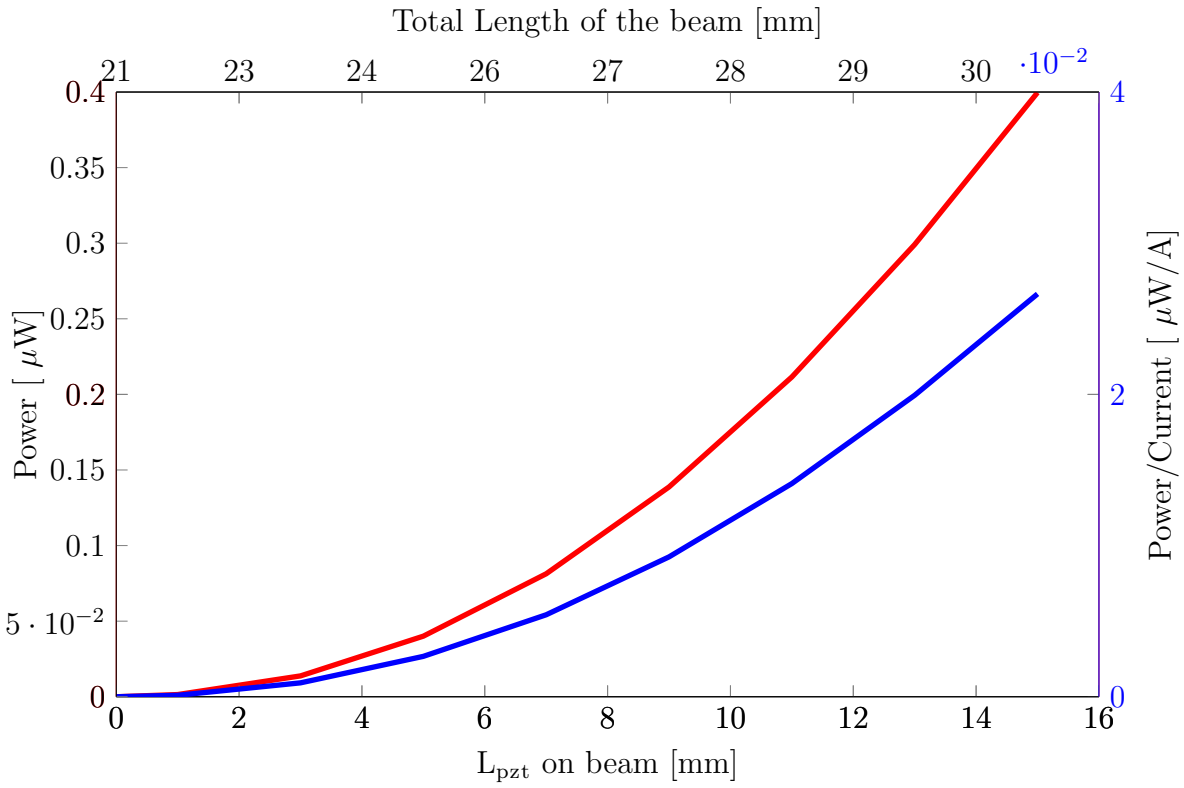


Figure 4.17: Harvesting Power output Vs. Amount of PZT along beam]

# Chapter 5

# Conclusions and Future Work

## 5.1 Summary Conclusions

In this thesis, developing a working model and functioning prototype of a power transmission line energy harvesting unit was the ultimate goal. The harvester was meant to be miniature in size and optimized for a harvesting frequency of 60 Hz. Model accuracy is a key design feature considering the certainty of the input frequency. Successful electromechanical modelling of the harvesting system was also essential.

Piezoelectric PZT-5A material was chosen as the optimal transduction mechanism and material for a bimorph cantilever beam configuration with a high strength bronze substrate. A series electrical connection was selected to increase voltage output of the harvester and a magnetic tip mass was used to lower the harvester frequency and size while creating force interaction between the harvester and conducting wire. The magnetic tip mas was analytically analyzed and simulation results determined orientation a) as the optimal magnetic configuration for the harvester design.

The harvester was modelled as a distributed parameter system with discontinuous beam sections which allow the amount of piezoelectric material to be minimized. The discontinuous model required additional continuity conditions as well as piecewise construction of the mode shapes. The overall model was successful in predicting natural frequency for the prototype fabricated EH10 within approximately 2 Hz of the designed frequency under short circuit conditions prior to tuning adjustments. The analytical model also was successful in predicting harvester frequencies at the experimentally determined maximum power resistance which was essential for maximum harvesting capability.

Two damping methods were selected including a closed-form solution which used voltage FRF data and non-dimensional parameters to determine modal damping ratios for an arbitrary load resistance. And also a more simplistic conventional approach commonly known as half-power bandwidth method which used the displacement FRF data under short-circuit conditions. In both cases, non-linear behavior was observed between voltage FRF and displacement FRF data sets for all experimental tests conducted.

Three validation experimental tests were preformed to test model validity. Base excitation was used to validate natural frequency and provide a simple method of determining maximum power resistance as well as all for quick minor tuning adjustments. The harvester electromechanical behavior seemed to agree with the model quite well however non-linearity was evident when comparing model error between voltage and displacement FRF data sets. Furthermore, the model seemed to overestimate the experimental voltage and power outputs over a range of frequencies slightly.

The harvester was then mounted on a conducting wire to observed the harvesting behavior when subjected to an EMF input at the tip of the beam due to the flux generated by a current carrying conductor. Modal damping values were re-established to find a small increase in damping possibly attributed to electromagnetic interaction affects. The reported harvester showed good agreement with the analytical model and maintained a similar model overestimation trend.

Lastly the harvester was tested on a real wall signal where a 2000W heater was used as a load operating at 120V producing three arbitrary current inputs to the harvester. The harvester performance followed a similar trend as found in the wire testing suggesting minimal additional interference despite the irregularity of the the wall signal away from 60 Hz.

## 5.2 Future Work

Considerations that should be made when moving forward with this work would be to develop more controlled fabrication techniques to reduce variability in piezoelectric coupling. The model overestimation should be explored further to determine if fabrication techniques play a strong role in piezoelectric coupling reduction. Damping characterization should also be a focus for future work, although that was not the focus of this thesis, the two methods tested provided varying degrees of accuracy between experimental tests and simulated model. Decreased damping found during the wire validation tests suggests electromagnetic damping of some kind may be present. At higher amperage this damping

may be even more predominant and such should be characterized further to improve model accuracy at the peaks.

These prototype designs should also be tested under higher current settings. Although the model shows good agreement for the current levels tested, higher current levels would provide a much more realistic validation of the model. Furthermore, limitations of the prototypes could be assessed at high amperages such as fatigue and over strain causing cracking and possibly saturation limits for this scale of harvester. Furthermore, given the environment this device may find itself in, temperature and weather testing of a more complete design is also essential for future work and a successful design.

Exploring scalability of the model and design is also a possibility for future work. Although the design was meant to be a miniature prototype for a proof of concept, research shows a large draw towards further miniaturization to the MEMS scale. Optimization of piezoelectric bimorphs using magnetic flux interaction methods for power transmission line harvesting seems like a logical next step.

# References


[1] J. Chen, X. Cao, P. Cheng, Y. Xiao, and Y. Sun. Distributed collaborative control for industrial automation with wireless sensor and actuator networks. *IEEE Transactions on Industrial Electronics*, 57(12):4219–4230, 2010. cited By (since 1996)48.

[2] G. Park, T. Rosing, M.D. Todd, C.R. Farrar, and W. Hodgkiss. Energy harvesting for structural health monitoring sensor networks. *Journal of Infrastructure Systems*, 14(1):64–79, 2008. cited By (since 1996)82.

[3] J. Ko, C. Lu, M.B. Srivastava, J.A. Stankovic, A. Terzis, and M. Welsh. Wireless sensor networks for healthcare. *Proceedings of the IEEE*, 98(11):1947–1960, 2010. cited By (since 1996)78.

[4] W.H. Liao, D.H. Wang, and S.L. Huang. Wireless monitoring of cable tension of cable-stayed bridges using pvdf piezoelectric films. *Journal of Intelligent Material Systems and Structures*, 12(5):331–339, 2001. cited By (since 1996)30.

[5] T.E. Starner. Powerful change part 1: Batteries and possible alternatives for the mobile market. *IEEE Pervasive Computing*, 2(4):86–88, 2003. cited By (since 1996)17.

[6] Robert Hahn and Herbert Reichl. Batteries and power supplies for wearable and ubiquitous computing. pages 168–169, 1999. cited By (since 1996)7.

[7] S. Roundy, P.K. Wright, and J. Rabaey. A study of low level vibrations as a power source for wireless sensor nodes. *Computer Communications*, 26(11):1131–1144, 2003. cited By (since 1996)953.

[8] X. Jiang, J. Polastre, and D. Culler. Perpetual environmentally powered sensor networks. volume 2005, pages 463–468, 2005. cited By (since 1996)185.

[9] U.S.-Canada Power System Outage Task Force. Final report on the august 14, 2003 blackout in the united states and canada: Causes and recommendations. 2012.

[10] S. Chalasani and J.M. Conrad. A survey of energy harvesting sources for embedded systems. pages 442–447, 2008. cited By (since 1996)48.

[11] Danial J. Inman Alper Erturk. *Piezoelectric Energy Harvesting*. Wiley, Chichester, West Sussex, U.K. Hoboken, N.J, 2011.

[12] S.P. Beeby, M.J. Tudor, and N.M. White. Energy harvesting vibration sources for microsystems applications. *Measurement Science and Technology*, 17(12):R175–R195, 2006. cited By (since 1996)819.

[13] S. Priya. Advances in energy harvesting using low profile piezoelectric transducers. *Journal of Electroceramics*, 19(1):165–182, 2007. cited By (since 1996)207.

[14] H.A. Sodano, D.J. Inman, and G. Park. A review of power harvesting from vibration using piezoelectric materials. *Shock and Vibration Digest*, 36(3):197–205, 2004. cited By (since 1996)506.

[15] C.B. Williams and R.B. Yates. Analysis of a micro-electric generator for microsystems. *Sensors and Actuators, A: Physical*, 52(1-3):8–11, 1996. cited By (since 1996)438.

[16] L. Moro and D. Benasciutti. Harvested power and sensitivity analysis of vibrating shoe-mounted piezoelectric cantilevers. *Smart Materials and Structures*, 19(11), 2010. cited By (since 1996)7.

[17] L. Mateu and F. Moll. Optimum piezoelectric bending beam structures for energy harvesting using shoe inserts. *Journal of Intelligent Material Systems and Structures*, 16(10):835–845, 2005. cited By (since 1996)89.

[18] J. Granstrom, J. Feenstra, H.A. Sodano, and K. Farinholt. Energy harvesting from a backpack instrumented with piezoelectric shoulder straps. *Smart Materials and Structures*, 16(5):1810–1820, 2007. cited By (since 1996)81.

[19] S.P. Beeby, R.N. Torah, M.J. Tudor, P. Glynne-Jones, T. O'Donnell, C.R. Saha, and S. Roy. A micro electromagnetic generator for vibration energy harvesting. *Journal of Micromechanics and Microengineering*, 17(7):1257–1265, 2007. cited By (since 1996)271.

[20] Yan Chen, Tim E Pollock, and Armaghan Salehian. Analysis of compliance effects on power generation of a nonlinear electromagnetic energy harvesting unit; theory and experiment. *Smart Materials and Structures*, 22(9):094027, 2013.

[21] Y. Chen and A. Salehian. Modeling, analysis and experimental validation of an electromagnetic energy harvesting unit. volume 2, pages 793–802, 2012. cited By (since 1996)0.

[22] P. Glynne-Jones, M.J. Tudor, S.P. Beeby, and N.M. White. An electromagnetic, vibration-powered generator for intelligent sensor systems. *Sensors and Actuators, A: Physical*, 110(1-3):344–349, 2004. cited By (since 1996)295.

[23] B. Yang, C. Lee, W. Xiang, J. Xie, J. Han He, R.K. Kotlanka, S.P. Low, and H. Feng. Electromagnetic energy harvesting from vibrations of multiple frequencies. *Journal of Micromechanics and Microengineering*, 19(3), 2009. cited By (since 1996)67.

[24] C.R. Saha, T. O'Donnell, N. Wang, and P. McCloskey. Electromagnetic generator for harvesting energy from human motion. *Sensors and Actuators, A: Physical*, 147(1):248–253, 2008.

[25] S. Roundy, P.K. Wright, and K.S.J. Pister. Micro-electrostatic vibration-to-electricity converters. pages 487–496, 2002. cited By (since 1996)6.

[26] R. O'Donnell. Energy harvesting from human and machine motion for wireless electronic devices. *Proceedings of the IEEE*, 96(9):1455–1456, 2008.

[27] Y. Naruse, N. Matsubara, K. Mabuchi, M. Izumi, and S. Suzuki. Electrostatic micro power generation from low-frequency vibration such as human motion. *Journal of Micromechanics and Microengineering*, 19(9), 2009. cited By (since 1996)71.

[28] X. Wu, A. Khaligh, and Y. Xu. Modeling, design and optimization of hybrid electromagnetic and piezoelectric mems energy scavengers. pages 177–180, 2008. cited By (since 1996)0.

[29] V.R. Challa, M.G. Prasad, and F.T. Fisher. A coupled piezoelectric-electromagnetic energy harvesting technique for achieving increased power output through damping matching. *Smart Materials and Structures*, 18(9), 2009. cited By (since 1996)28.

[30] B. Yang, C. Lee, W.L. Kee, and S.P. Lim. Hybrid energy harvester based on piezoelectric and electromagnetic mechanisms. *Journal of Micro/ Nanolithography, MEMS, and MOEMS*, 9(2), 2010. cited By (since 1996)12.

[31] Torsten Reuschel and Armaghan Salehian. Analysis and modelling towards hybrid piezoelectromagnetic vibrating energy harvesting devices. *AIP Conference Proceedings*, 1368(1):81–84, 2011.

[32] M. Wischke, M. Masur, F. Goldschmidtboeing, and P. Woias. Electromagnetic vibration harvester with piezoelectrically tunable resonance frequency. *Journal of Micromechanics and Microengineering*, 20(3), 2010.

[33] C. Eichhorn, R. Tchagsim, N. Wilhelm, and P. Woias. A smart and self-sufficient frequency tunable vibration energy harvester. *Journal of Micromechanics and Microengineering*, 21(10), 2011.

[34] E.S. Leland and P.K. Wright. Resonance tuning of piezoelectric vibration energy scavenging generators using compressive axial preload. *Smart Materials and Structures*, 15(5):1413–1420, 2006.

[35] C. Eichhorn, F. Goldschmidtboeing, and P. Woias. Bidirectional frequency tuning of a piezoelectric energy converter based on a cantilever beam. *Journal of Micromechanics and Microengineering*, 19(9), 2009. cited By (since 1996)35.

[36] D. Zhu, S. Roberts, M.J. Tudor, and S.P. Beeby. Design and experimental characterization of a tunable vibration-based electromagnetic micro-generator. *Sensors and Actuators, A: Physical*, 158(2):284–293, 2010. cited By (since 1996)52.

[37] Y. Tadesse, Shujun Zhang, and S. Priya. Multimodal energy harvesting system: Piezoelectric and electromagnetic. *Journal of Intelligent Material Systems and Structures*, 20(5):625–632, 2009. cited By (since 1996)48.

[38] I. Sari, T. Balkan, and H. Kulah. An electromagnetic micro power generator for wideband environmental vibrations. *Sensors and Actuators, A: Physical*, 145-146(1-2):405–413, 2008. cited By (since 1996)117.

[39] H. Liu, C. Lee, T. Kobayashi, C.J. Tay, and C. Quan. Investigation of a mems piezoelectric energy harvester system with a frequency-widened-bandwidth mechanism introduced by mechanical stoppers. *Smart Materials and Structures*, 21(3), 2012. cited By (since 1996)17.

[40] A. Erturk and D.J. Inman. Broadband piezoelectric power generation on high-energy orbits of the bistable duffing oscillator with electromechanical coupling. *Journal of Sound and Vibration*, 330(10):2339–2353, 2011. cited By (since 1996)54.

[41] S. Roundy and P.K. Wright. A piezoelectric vibration based generator for wireless electronics. *Smart Materials and Structures*, 13(5):1131–1142, 2004. cited By (since 1996)480.

[42] Shadrach Joseph Roundy. *EEnergy Scavenging for Wireless Sensor Nodes with a Focus on Vibration to Electricity Conversion*. PhD thesis, THE University of California, Berkeley, 2003.

[43] N.E. DuToit, B.L. Wardle, and S.-G. Kim. Design considerations for mems-scale piezoelectric mechanical vibration energy harvesters. volume 71, pages 121–160, 2005. cited By (since 1996)228.

[44] A. Erturk and D.J. Inman. A distributed parameter electromechanical model for cantilevered piezoelectric energy harvesters. *Journal of Vibration and Acoustics, Transactions of the ASME*, 130(4), 2008. cited By (since 1996)189.

[45] A Erturk and D J Inman. An experimentally validated bimorph cantilever model for piezoelectric energy harvesting from base excitations. *Smart Materials and Structures*, 18(2):025009, 2009.

[46] S. Bashash, A. Salehi-Khojin, and N. Jalili. Forced vibration analysis of flexible euler-bernoulli beams with geometrical discontinuities. pages 4029–4034, 2008. cited By (since 1996)4.

[47] X. Zhao, T. Keutel, M. Baldauf, and O. Kanoun. Energy harvesting for overhead power line monitoring. 2012. cited By (since 1996)0.

[48] K. Chang, S. Kang, K. Park, S. Shin, H.-S. Kim, and H. Kim. Electric field energy harvesting powered wireless sensors for smart grid. *Journal of Electrical Engineering and Technology*, 7(1):75–80, 2012. cited By (since 1996)7.

[49] Larry Fish. Power donut systems for overhead electric power line monitoring, 2012.

[50] Z. Wu, Y. Wen, and P. Li. A power supply of self-powered online monitoring systems for power cords. *IEEE Transactions on Energy Conversion*, 28(4):921–928, 2013. cited By (since 1996)0.

[51] R.H. Bhuiyan, R.A. Dougal, and M. Ali. A miniature energy harvesting device for wireless sensors in electric power system. *IEEE Sensors Journal*, 10(7):1249–1258, 2010. cited By (since 1996)17.

[52] V. Gupta, A. Kandhalu, and R. Rajkumar. Energy harvesting from electromagnetic energy radiating from ac power lines. 2010. cited By (since 1996)0.

[53] E.S. Leland, P.K. Wright, and R.M. White. A mems ac current sensor for residential and commercial electricity end-use monitoring. *Journal of Micromechanics and Microengineering*, 19(9), 2009. cited By (since 1996)28.

[54] Q. Xu, M. Seidel, I. Paprotny, R.M. White, and P.K. Wright. Integrated centralized electric current monitoring system using wirelessly enabled non-intrusive ac current sensors. pages 1998–2001, 2011. cited By (since 1996)3.

[55] Q.R. Xu, I. Paprotny, M. Seidel, R.M. White, and P.K. Wright. Stick-on piezoelectromagnetic ac current monitoring of circuit breaker panels. *IEEE Sensors Journal*, 13(3):1055–1064, 2013. cited By (since 1996)1.

[56] W. He, P. Li, Y. Wen, and C. Lu. A self-powered high sensitive sensor for ac electric current. pages 1863–1865, 2011. cited By (since 1996)0.

[57] Eli S Leland, Richard M White, and Paul K Wright. Energy scavenging power sources for household electrical monitoring. *PowerMEMS (Dec. 2006)*, 2006.

[58] I. Paprotny, E. Leland, C. Sherman, R.M. White, and P.K. Wright. Self-powered mems sensor module for measuring electrical quantities in residential, commercial, distribution and transmission power systems. pages 4159–4164, 2010. cited By (since 1996)4.

[59] I. Paprotny, Q. Xu, W.W. Chan, R.M. White, and P.K. Wright. Electromechanical energy scavenging from current-carrying conductors. *IEEE Sensors Journal*, 13(1):190–201, 2013. cited By (since 1996)3.

[60] W. He, P. Li, Y. Wen, J. Zhang, A. Yang, C. Lu, J. Yang, J. Wen, J. Qiu, Y. Zhu, and M. Yu. Piezoelectric energy harvester scavenging ac magnetic field energy from electric power lines. *Sensors and Actuators, A: Physical*, 193:59–68, 2013. cited By (since 1996)1.

[61] W. He, P. Li, Y. Wen, J. Zhang, C. Lu, and A. Yang. Energy harvesting from electric power lines employing the halbach arrays. *Review of Scientific Instruments*, 84(10), 2013. cited By (since 1996)0.

[62] S.B. Lao, S.S. Chauhan, T.E. Pollock, T. Schrder, I. Cho, and A Salehian. Design, fabrication and temperature sensitivity testing of a miniature piezoelectric-based sensor for current measurements. 2013.

[63] Magnet Sales & Manufacturing Inc. Properties of alnico magnets, 2014.

[64] Nathan Ida. *Electromagnetics and calculation of fields*. Springer, Heidelberg, 2013.

[65] K&J Magnetics Inc. Neodymium magnet physical properties, 2014.

[66] Magnet Sales & Manufacturing Inc. Properties for ferrite magnets, 2012.

[67] Magnet Sales & Manufacturing Inc. Properties of samarium cobalt magnets, 2014.

[68] H. S. Tzou. *Piezoelectric shells : distributed sensing and control of continua*. Kluwer Academic, Dordrecht Boston, 1993.

[69] Donald Leo. *Engineering analysis of smart material systems*. John Wiley & Sons, Hoboken, N.J, 2007.

[70] Alper Erturk. *Electromechanical Modeling of Piezoelectric Energy Harvesters*. PhD thesis, Virginia Polytechnic Institute and State University, 2009.

[71] D. J. Inman. *Engineering vibration*. Pearson Prentice Hall, Upper Saddle River, N.J, 2008.

[72] ASM Aerospace Specification Metals Inc. 6000 series aluminum alloy, 2014.

[73] McMaster-Carr. Physical and mechanical properties of copper, brass, and bronze alloys, 2014.

[74] Piezo Systems Inc. Typical matrix for psi-5a4e, 2014. Document with material parameters was provided by Piezo System, Inc.

[75] Inc The Modal Shop. 75 lbf dual purpose shaker, 2014.

[76] LMS. Lms scadas mobile, 2014.

[77] PCB Piezotronics. Model: 352a24 product specifications, 2014.

[78] Polytec Advanced Measurements by Light. Ofv-50x vibrometer sensor head and controller, 2014.

[79] M.A. Ahmad, A.M. Elshurafa, K.N. Salama, and H.N. Alshareef. Determination of maximum power transfer conditions of bimorph piezoelectric energy harvesters. *Journal of Applied Physics*, 111(10), 2012. cited By (since 1996)2.